Lawrence Berkeley Laboratory
UNIVERSITY OF CALIFORNIA

CHEMICAL BIODYNAMICS DIVISION

AN X-RAY ABSORPTION SPECTROSCOPY STUDY OF MANGANESE CONTAINING COMPOUNDS AND PHOTOSYNTHETIC SPINACH CHLOROPLASTS

Jon Allan Kirby
(Ph.D. thesis)

May 1981

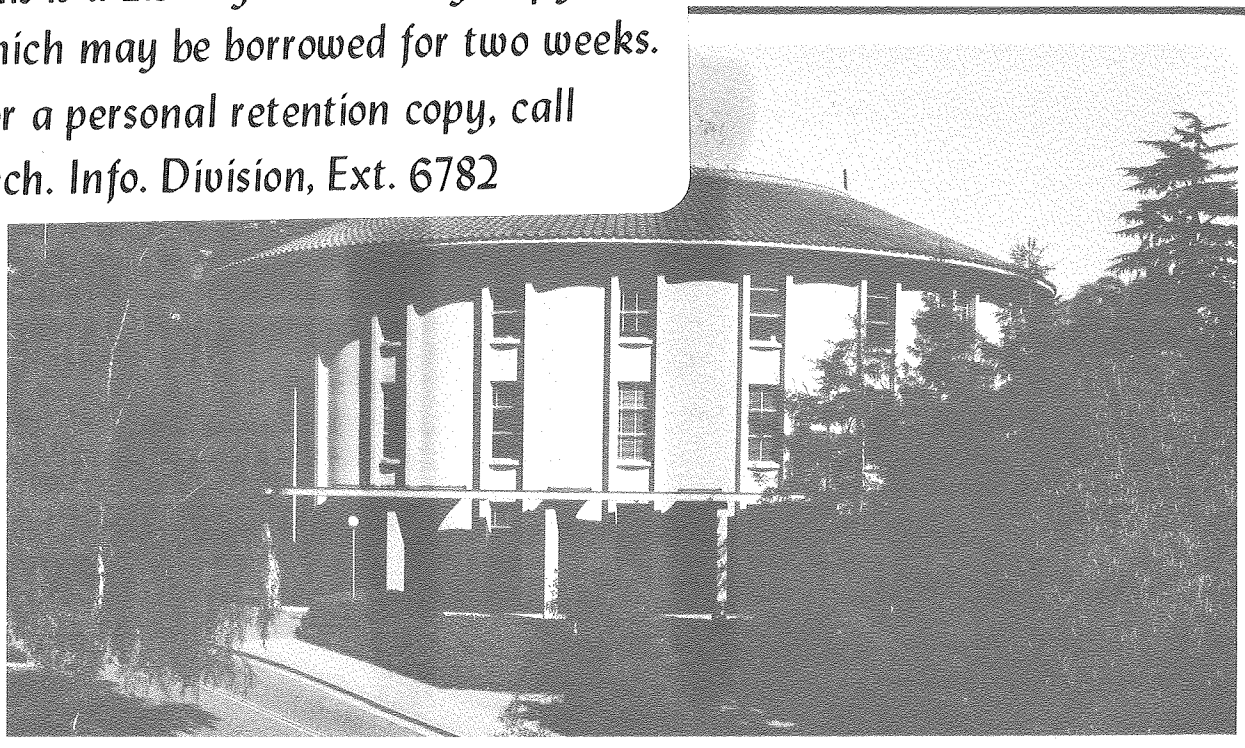

Prepared for the U.S. Department of Energy under Contract W-7405-ENG-48

DISCLAIMER

LBL-12705

AN X-RAY ABSORPTION SPECTROSCOPY STUDY OF MANGANESE CONTAINING COMPOUNDS AND PHOTOSYNTHETIC SPINACH CHLOROPLASTS

Jon Allan Kirby

Ph.D. Thesis

May 1981

Lawrence Berkeley Laboratory
University of California
Berkeley, CA 94720

This work was supported in part by the United States Department of Energy under Contract No. W-7405-ENG-48. Synchrotron Radiation facilities were provided by the Stanford Synchrotron Radiation Laboratory, which is supported by NSF grant DMR-07692-A02.

CONTENTS

CONTENTS (Continued)

ACKNOWLEDGEMENTS

The support and encouragement of Drs. Melvin P. Klein and Albert C. Thompson of LBL, without whom this work could not have been accomplished, is gratefully acknowledged.

I wish to acknowledge my co-conspirator in crime, Dr. Alan S. Robertson, without whom data analysis would not have been possible and the arsenic data would have been non existant.

I wish to thank Prof. Kenneth Sauer, Dr. Robert Blankenship, Ms. A. McGuire and Dr. Tom Wydrzynski for their extensive help with preparing and characterizing the chloroplast samples and interpreting the chloroplast XAS results.

I wish to acknowledge my fellow graduate students who have assisted at various points in this work: David Goodin, Tim Walker, Dr. Joseph Smith, Ninon Kafka, Dr. Steven Cooper and Al Ramponi. I wish to thank Dr. Joseph Jaklevic of LBL for his assistance at various times.

Lastly, I wish to thank my wife, Andrea, for putting up with me over the years and my son, Jack, whose birth provided the impetus to finish.

This work was supported in part by the United States Department of Energy under Contract No. W-7405-ENG-48. Synchrotron radiation facilities were provided by the Stanford Synchrotron Radiation Laboratory, which is supported by NSF grant DMR-07692-A02.

An X-ray Absorption Spectroscopy Study of Manganese Containing Compounds and Photosynthetic Spinach Chloroplasts

Jon Allan Kirby

B.S. (Ottawa University) 1970

M.A. (University of California) 1972

Abstract

The manganese sites in chloroplasts, long thought to be involved in photosynthetic oxygen evolution have been examined and partially characterized by X-ray Absorption Spectroscopy (XAS) using synchrotron radiation.

The local environment about the manganese atoms is estimated from an analysis of the extended X-ray Absorption Fine Structure (EXAFS). Comparisons with and simulations of the manganese EXAFS for several reference compounds leads to a model in which the chloroplast manganese atoms are contained in a binuclear complex similar to di-u-oxo-tetrakis-(2,2'-bipyridine) dimanganese. It is suggested that the partner metal is another manganese. The bridging ligands are most probably oxygen. The remaining manganese ligands are carbon, oxygen, or nitrogen.

A roughly linear correlation between the X-ray K edge onset energy and the "coordination charge" of a large number of manganese coordination complexes and compounds has been developed. Entry of the chloroplast manganese edge energy onto this correlation diagram establishes that the active pool of manganese is in an oxidation state greater than +2. If the manganese is in a dimeric form the oxidation states are

most probably (II,III).

Underlying these results is an extensive data analysis methodology. The method developed involves the use of many different background removal techniques, Fourier transforms and ultimately curve fitting to the modulations in the x-ray absorption cross sections.

A large number of model compounds were used to evaluate the analysis method. These analyses are used to show that the two major curve fitting models available are essentially equivalent. Due to its greater versatility, the theoretical model of Teo and Lee is preferred (J. Am. Chem. Soc. (1979), 101, 2815). The results are also used to determine the informational limitations of XAS within the limits of the present understanding of X-ray absorption phenomena by inner shell electrons for atoms with atomic number greater than that of argon.

Madison S. Kelley

Chapter I

INTRODUCTION

The single source of all energy utilized in the Earth's biosphere is the absorption of radiant energy from the sun by the process known as Photosynthesis. It is known that the photosynthetic process takes the energy of the incident optical radiation and converts a substantial percentage of this energy into the compounds adenosine triphosphate (ATP) and reduced nicotinamide adenine dinucleotide phosphate (NADPH). ATP and NADPH are then used in the biosynthesis of the vast varieties of bio-organic molecules such as sugars and proteins. The harnessing of the radient energy is accomplished by the degradation of excited electronic states. The initial excitation is created by the absorption of an incident photon. The subsequent gradual degradation, accomplished by electron transfer from molecule to molecule, is used to drive the chemical reactions which create ATP and NADPH.

This movement of excited electrons means that the process of photosynthesis must have some source of electrons to replace the transported ones. In the higher green plants and the blue-green algae, the transported electrons are replaced by stripping electrons from water molecules and creating the biologically necessary oxygen molecule, O_2. The overall chemical reaction is expressed in the equation

$$2H_2O \rightarrow O_2 + 4H^+ + 4e^-$$

Unlike the rest of the photosynthetic process, very little is known about the mechanism of this reaction. However, it has been known for many years that manganese is an essential trace element for this reaction. The exact role of the manganese in oxygen evolution is not

known, but it is known that the manganese is not a passive participant (1).

The largest single reason for the lack of knowledge concerning the manganese is the inability of the normal types of spectroscopy, such as optical or Electron Paramagnetic Resonance (EPR), to observe the weak transitions produced by manganese in most chemical environments. Thus, some new type of element specific spectroscopy was needed to probe this system.

One of the most element-specific phenomena is the absorption of incident X-rays by the inner shell 1s or K electrons of an atom. Thus, the recently rediscovered field of X-ray Absorption Spectroscopy (XAS) potentially allows the examination of specific elements. XAS is composed of two separate techniques which yield different information. One technique is X-ray Absorption Edge Spectroscopy (XAES). XAES examines the energy region near the onset for a given K-shell X-ray absorption. In this region the absorption is due to transitions into unoccupied bound states in a nonconductor or into the conduction bands in a conductor. It has been known for many years that XAES results are chemically sensitive, but it has been a problem to obtain good correlations with known chemical states (3). The second technique utilizes the phenomena known as Kronig structure or X-ray Absorption Fine Structure (EXAFS). EXAFS is the modulations that appear in the photoelectron absorption cross section as the energy of the photoelectron changes. The modulations are due to the presence of atomic neighbors to the absorbing atom. Thus, it should be possible to extract local structural information from the EXAFS. Therefore, if certain problems

could be solved it should be possible to obtain a considerable amount of information about the manganese associated with photosynthetic oxygen evolution from XAS.

The result of the EXAFS studies is the prediction that the manganese, that is known to be essential for oxygen evolution, exists in a dimeric (or multimeric) bridged form with carbon, nitrogen or oxygen bridging ligands. This structure is very similar to the class of compounds represented by di-μ-oxo-tetrakis (2, 2'-bipyridine) dimanganese (III, IV) perchlorate.

The results of the XAES studies strongly suggest that in the "dark adapted" or "resting" state the manganese dimer (multimer) exists in either a (II, III) or (III, III) configuration, although (II, II) or (III, IV) cannot be absolutely excluded.

The majority of the work that is presented in this dissertation has been the resolution of the many problems associated with utilizing XAS with dilute species and evaluating the capabilities of the two XAS subsets, XAES and the EXAFS phenomena. The final part of this dissertation is the application of XAS technique to study the manganese involved in photosynthetic oxygen evolution in its "dark adapted" state, the results of which are described above.

The first problem was to increase the sensitivity of XAS because the low concentration of photosynthetic manganese results in a very small fraction of the total X-ray absorption being due to the element of interest, manganese.

The sensitivity increase was accomplished in 1975 by indirectly measuring the absorption of the incident X-rays by monitoring the X-ray

fluorescence produced as a result of manganese absorption events. The details of this experimental technique are described in Joseph Smith's Ph.D thesis (2) and will not be discussed in this work.

The second problem was to develop reliable data analysis methods for XAS. The general data extraction method that was developed is extensively described in the first part of Chapter III. The development and evaluation of the analysis method used to process EXAFS spectra is described in detail in the last part of Chapter III. The application of the methods described in Chapter III to the photosynthetic manganese problem is presented in Chapter IV. A reasonable correlation between a theoretical electronic charge on the X-ray absorbing atom and the X-ray edge energy obtained from XAES analysis was obtained. The details and its application to the photosynthetic manganese problem is presented in Chapter V.

REFERENCES

Chapter I

1. K. Sauer; Accts. Chem. Res., 13 (1980) 249.

2. J. P. Smith; Ph. D. Thesis, University of California, Berkeley (1978).

3. U. C. Srivastava and H. L. Nigam; Coord. Chem. Rev., 9 (1972-3) 275.

Chapter II

X-RAY ABSORPTION SPECTROSCOPY

THEORY AND EXPERIMENT

The total X-ray absorption cross section $\mu(E)$, where E is the energy of the incident X-ray photon, can be divided into two main parts and can be defined as $\mu(E) = \mu_I(E) + \mu_p(E)$ where $\mu_I(E)$ is the absorption cross section due to the electrons of interest and $\mu_p(E)$ is the "pre-edge" background. $\mu_p(E)$ is the absorption cross section of all the other electrons in the absorbing sample which have lower binding energies than the electrons of interest, as well as a small contribution from Thompson and Compton scattering from all the electrons in the sample. $\mu_I(E)$ has many parts and can be expressed as:

$$\mu_I(E) = \mu_E(E) + \mu_S(E) + \mu_0(E)\ (1 + \chi(E)) \qquad (1)$$

where μ_E contains the sudden cross section increase caused by electronic transitions to previously unoccupied atomic, molecular and crystalline states ("X-ray edge"); μ_0 is the free atom photoelectric effect cross section; μ_S is the smooth monotonically decreasing absorption cross section enhancement observed in the photoelectric effect cross section in the energy region closest to the X-ray edge; and $\chi(E)$ is the observed Extended X-ray Absorption Fine Structure or EXAFS modulation of the free atom photoelectric effect.

$\mu_E(E)$ is the part of $\mu_I(E)$ which is associated with the energy region near the sharp increase in absorption cross section known as the "X-ray Absorption Edge" or "edge region", for short. μ_E is usually non-zero only when the incident photon energy is less than the binding energy of the absorbing electron. μ_E contains all transitions of an inner shell electron to unoccupied localized orbitals (1). For ionic

and molecular compounds, these transitions are transitions into empty atomic and molecular orbitals. For metals and semiconductors, these transitions are promotions into partially filled or empty conduction bands or into excitonic or hole states. Thus, μ_E is usually contained within the photon energy region of 10 eV below the edge to approximately 30 eV above the edge (see for example, Figures 1, 2, 4 and 5).

$\mu_0(E)$ is the absorption cross section representative of the free atom photoelectric effect. If a photon absorbed by a free atom has an energy greater than the binding energy of the absorbing electron, then a electron can be promoted to a free electron state and leave the atom as a photoelectron. For free atoms $\mu_0(E) + \mu_E(E)$ contains the only options for X-ray absorption available and, therefore, constitutes a complete description of $\mu_I(E)$.

For absorbing atoms which exist in an ordered multiatomic, condensed phase, the assumption that a photoelectron's final state is just free electron-like is not valid. When in a condensed phase, a low energy photoelectron (less than 40 eV) is not in a free electron state, but in one of the "conduction band" states of that phase. Only when the photoelectron's energy is greater than approximately 40 eV can the electron's state be described as free electron-like. The presence of these "conduction bands" is exhibited by a significantly enhanced absorption cross section when compared to what would be expected from the free atom cross section, μ_0. This enhancement has a maximum of approximately 5% of μ_0 when the photon's energy is near the threshold for producing photoelectrons and monotonically decreases to zero when the photoelectron's state is essentially free electron-like

(energy of the photoelectron is approximately 40 eV) (3). This additional cross section is represented by $\mu_S(E)$ in equation 1.

Also in a condensed phase, a photoelectron will be partially scattered by the rest of the nearby atoms. These scattered components in a photoelectron's state appear in the absorption cross section as sinusoidal modulations of the free atom absorption cross section, μ_0. The modulations usually never exceed 10% of μ_0 and, thus, are generally represented as a fraction of μ_0. The modulation factor or the Extended X-ray Absorption Fine Structure (EXAFS) is represented in equation 1 as $\chi(E)\ \mu_0(E)$.

All of the terms in equation 1 have now been described in detail above. In practice, a number of simplifying assumptions can be made. $\mu_S(E)$ contains no useful information and so can be neglected and in general can be considered to be part of the experimental background that is removed. When the photoelectron's energy is too low to permit the free electron approximation to be valid, the EXAFS theory presented later in this chapter is not valid. This means that the photon energy region of interest for examining the EXAFS phenomena is at least 70 eV beyond the X-ray edge 30 eV from μ_E and 40 eV for free electron state and extends as high as usable data can be obtained. In the rest of this work, this energy region will be referred to as the "EXAFS region", although EXAFS modulations extend from the "edge region" to infinite photon energy. Also, there is a slight overlap of the non-zero regions of μ_E, μ_S and μ_0. They are nearly impossible to separate, so no attempt is made. Whenever the terms "edge region" or "X-ray edge" are used in the future, it is assumed that the small contributions of μ_S and μ_0 to

μ_I in that energy region will be ignored. Thus, it is assumed that near the X-ray absorption edge, $\mu_I(E) = \mu_E(E)$ and in the EXAFS region $\mu_I(E) = \mu_0(E)\ (1 + \chi(E))$.

I. X-ray Absorption Edge Spectroscopy (XAES) Theory

This section discusses μ_E, the XAES or edge region of the absorption cross section. To date, the understanding of the nature of the XAES data is mostly qualitative. A good review of this understanding as applied to coordination chemistry was presented by Srivastava and Nigam (4). A qualitative classification of the types of edge spectra was presented by Van Nordstrand (5, 6). The edge shape was correlated with the known local environment and symmetry around the absorber being studied.

Correlations of the position and shape of the edge features have been made with the oxidation state of the absorber. The edge width (7), the inflection point of the absorption edge (8), the position of the main absorption maximum (9), and the positions of other peaks (10) have been used for this purpose. The inflection point E_i where

$$\left(\frac{\delta^2 \mu}{\delta E^2}\right)_{E_i} = 0$$

is a valuable piece of information only if inflection points of the same feature are used in all cases. The inflection point of an edge in one compound which does not have a certain transition cannot be compared in a simple way with the inflection point of another compound in which that transition is allowed. Since broadening of the data exists, these

problems do affect the accuracy of the correlations.

Shulman et al. (10) have extended and refined this qualitative understanding. Highly ionic model systems with fluorine ligands were studied. Their approach of using the completely relaxed core approximation and the corresponding atomic states worked well, e.g., consider a transition from the K shell of As^{+5}. The one electron transition is from 1s to n'ℓ' or

$$(As)^{+5}\{1s^2 2s^2 2p^6 3s^2 3p^6 3d^{10}\} \rightarrow (As^*)^{+5}\{1s2s^2 2p^6 3s^2 3p^6 3d^{10}\}n'\ell' \qquad (2)$$

Shulman et al. treat the excited state n'ℓ' as atomic in character and localized on the metal ion. Since the 1s hole is close to the nucleus, the final state of the outer shell of an ion having atomic number Z can be approximated by the atomic states of the element Z + 1 but with a $1s^2$ core. Thus,

$$(As^*)^{+5}\{1s2s^2 2p^6 3s^2 3p^6 3d^{10}\}n'\ell' \equiv (Se)^{+5}\{1s^2 2s^2 2p^6 3s^2 3p^6 3d^{10}\}n'\ell' \qquad (3)$$

The transition is from As^+ to Se^+ (n'ℓ') in this approximation. The spectroscopic tables (11) of the (Z +1) ion (Se^{+5}) can be used. Figures 1 and 2 show the spectra of $Cs^+AsF_6^-$ and AsF_3 and the appropriate ionic states as illustrations of how this works for two highly ionic compounds which were examined during this work.

For their highly ionic compounds, Shulman et al. (10) were able to identify 1s → 3d, 1s → 4s, 1s → 4p transitions in the iron fluorides and predict their intensity in agreement with optical transitions.

For a detailed comparison of these and other spectra, calculations of the molecular orbitals with an ionized absorbing atom must be made. Such calculations are not available. However, it is often possible to use normal molecular orbital calculations to predict the identity of edge transitions, but the energy spacings will be incorrect. Consider the case of the tetrahedrally bonded species MnO_4^-. The molecular orbital energy levels are presented in Table 1 and graphically displayed in Figure 3 (41). Due to the presence of the core hole upon X-ray absorption, producing an iron-like potential, the energy levels of all these states should change. All four of the empty orbitals in Figure 3 and Table 1 have strong p or ℓ=1 state contributions so that all should appear in the XAES spectrum. A set of assignments is presented in Figure 4. These assignments seem quite reasonable. The energy spacing between the 2e and $3a_1$ states in MnO_4^- is 21 eV. With the production of the core hole all the bound states should become more tightly bound and the $3a_1$ state, which is the anti-bonding conjugate of the $1a_1$ state, should become more energetic. Therefore, the energy spacing should increase, in agreement with the observed energy difference of 50 eV. If these assignments are reasonable then equivalent transitions should exist in α-MnO_2 which has a distorted tetrahedral structure. The XAES spectrum of α-MnO_2 is presented in Figure 5. Note the apparent splitting of the 2e, $4t_2$ and $5t_2$ transitions while the $3a_1$ transition seems unaltered. This is due to splitting of the orbital energy levels by the structural disorder. Since the $3a_1$ state is not degenerate it can not result in more than one transition.

An interesting consequence of making the above transition assignments is the prediction that the pre-edge transition, 2e, should not

appear in an octahedral environment since the 2e and $4t_2$ orbitals invert in energy in the octahedral structure (becoming the e_g and t_{2g} orbitals, respectively). The t_2 state has a strong atomic p contribution and is, thus, the state responsible for the edge onset. Therefore, there should be no pre-edge transition observed. To date no pre-edge transition has been observed in any octahedral environment.

Ab initio calculations of various metal spectra which agree well with XAES spectra have been made (12). The ℓ=1 projected density of final states was computed by the linear augmented plane-wave (APW) method. In addition, the Ti emission and absorption spectra of various oxides of Ti have compared favorabley with theoretical calculations (13).

Therefore, fo all compounds a great deal is understood about the nature of the edge region. However, there is still need for the qualitative approach reviewed by Srivastava and Nigam (4). The identity and nature of the absorption site affects the spectrum. When the site is unknown, interpretation of the edge spectrum is often at a qualitative level.

II. Extended X-ray Absorption Fine Structure (EXAFS) Theory

Beyond the edge region, as the energy is increased, there is a gradual decline in the absorption cross section μ_0 of equation 1. Simple theory predicts only this smooth decrease. The promotion of electrons into this continuum region of free electrons is modulated by an oscillatory structure, $\mu_0\chi(k)$ of equation 1, which has been called EXAFS.

The early theories of the EXAFS modulations were reviewed in 1963 by Azaroff. The theories can be divided into two basic types: long range order (LRO); and short range order (SRO). Kronig (15, 16) described the modulations in terms of a change in the density of states due to the diffraction of final state electrons off periodic planes of atoms. This LRO theory was modified by Hayasi (17, 18).

Kronig (19) and Petersen (20, 21) also first introduced the SRO theory as an explanation for the fine structure in the absorption spectra of a diatomic molecule. Kostarev (22) criticized Kronig's original theory because it did not explain features of non-crystalline materials. He developed a short range order theory (22, 23) in which scattering from nearby neighbors caused the EXAFS modulation. In support of an SRO theory, Shiraiwa et al. (24, 25) pointed out that the ejected photoelectron travels only a few lattice spacings before the amplitude of its wave becomes zero. In 1961, Kozlenkov (26) reviewed the SRO theories.

The SRO theoretical approach has proven to be the most accurate description. The greatest advancement of EXAFS theory was presented by Sayers et al. (27, 28). Further refinement of the theory (29) showed excellent agreement with the data. This showed that the interference of the wave backscattered by nearby atoms with the original outgoing electron wave is the basis of the EXAFS modulations. The basic theoretical equation derived is:

$$\chi(k) = \sum_j \frac{N_j}{kR_j^2} |f_j(k,\pi)|\ e^{-2\sigma_j k^2} e^{-R_j/\lambda(k)} \sin\{2kR_j + \alpha_j(k)\} \qquad (4)$$

where the sum is over all shells and types of atoms, N_j is the number of atoms at a distance R_j from the absorber of interest, k is the photoelectron wavevector (defined by $k = 2\pi \sqrt{2m(E-E_0)}/h$, where E is the X-ray photon energy and E_0 is the threshold at which the electron becomes free), $|f_j(k,\pi)|$ is the magnitude of the back scattering off nearby atoms (scatter angle of π), $\alpha_j(k)$ is a sum of the phase shifts due to the scattering process of nearby atoms and the potential well around the absorber of interest, σ_j is the mean square relative displacement of the atom j along the line from absorber to scatterer and $\lambda(k)$ is the mean free path of the electron.

Figure 6 demonstrates a qualitative description of the EXAFS effect. An X-ray photon of energy $E = h\nu$ liberates a photoelectron from the absorber A which can be represented as a free outgoing spherical wave (solid lines on Figure 6). This wave has a probability for backscattering from nearby atoms B. This backscattered wave (dashed lines on Figure 6) can interfere constructively (Figure 6a) or destructively (Figure 6b) with the original outgoing electron wave. As the energy of the photon is increased, the electron's energy is correspondingly increased. Its wavelength decreases and the constructive and destructive interference of Figures 6a and 6b alternate. This changing interference pattern modulates the transition matrix element of the photon absorption process.

Note that the shape of the backscattering envelope $|f_j(k,\pi)|$ depends on the nature of the scattering atoms B. $\alpha_j(k)$ depends on the atomic number type of both the absorber atoms A and B and can be separated into the component parts contributed by atoms A and B. To a

limited extent, these parameters are also dependent on the oxidation state of atoms A and B.

Sayers et al. (17, 18) made a simple calculation using muffin-tin potentials and point scatterers which agreed well with experiment. More sophisticated calculations followed. Kincaid used the Hartree-Fock approximation to calculate EXAFS theoretically (30, 31). His major discrepancy was that his theoretical values for $|f_j(k,\pi)|$ were twice the size of the experimental results.

Ashley and Doniach (32, 33), Hayes and Sen (34, 35), and Lee and Pendry (36) expanded and generalized the theory. Multiple scattering (33) of the electron can occur. Focusing (36) of the electron occurs when the absorber and the first and second coordination sphere ligands of the absorber are colinear. Under most circumstances, multiple scattering is negligible and focusing does not occur so the single scattering theory of Sayers et al. in equation 4 provides an excellent description of the EXAFS spectra (33, 36).

Recently Lee and Beni (37) and Teo and Lee (38) have made ab initio calculations of the absorber and scatterer phase shifts and scatterer amplitude using Herman-Skillman and Clementi-Rossi wave functions. The agreement of these calculations with some experiments has been excellent (37, 38). Therefore, it is not always necessary to have known model compounds to provide these parameters in order to analyze an unknown system. Teo and Lee's calculations are used in the analysis of the data in this work.

III. X-ray Absorption Spectroscopy (XAS) Experiment

X-ray absorption spectroscopy experiments are conceptually simple. The X-rays from a broadband X-ray source are passed through a tunable monochromator. The intensity of the beam in front of the sample (I_0) and behind the sample (I) are measured as the monochromator is swept through the energy range of interest. From the Lambert-Beer law, $I = I_0 e^{-\mu x}$, the absorption coefficient for a give sample thickness x can be calculated, $\mu = 1n(I_0/I)/x$. As before, $\mu = \mu_I + \mu_P$ where μ_I is the photoelectric cross section of the absorption edge of interest and μ_P is the slowly varying absorption due to other edges and scatter.

The excitation of the photoelectron creates an inner shell vacancy which may relax via a radiative transition from a higher occupied state. The probability of this fluorescence is proportional to the original absorption probability. Therefore, fluorescence is a direct measure of the photoelectric cross section μ_I. In practice, for thin or dilute samples, if the fluorescence intensity F is measured, then $\mu = kF/I_0$ where k is a slowly varying number which depends on the fluorescence efficiency, the detector solid angle, sample thickness and total cross-section μ. A version of the fluorescent technique was first used by our research group (39) and is the method by which the chloroplast data were obtained.

The synchrotron radiation source and absorption XAS experimental equipment at the Stanford Synchrotron Radiation Laboratory (SSRL) were used to perform these experiments. The experimental apparatus is described below and elsewhere (30). The fluorescence detector used was a triplet Si(Li) detector built at Lawrence Berkeley Laboratory, similar

to those used in Nuclear Physics research (42).

The intense broadband continuous synchrotron spectrum is created by the acceleration of the electrons in the bending magnets of the SPEAR storage ring at the Stanford Linear Accelerator Center (SLAC). Experiments were not performed using X-rays from discharge tubes because they have significantly less intensity. A 20 minute experiment at SSRL would require 10 days with a standard X-ray tube. The synchrotron radiation beam exits the SPEAR vacuum through a thin beryllium window and travels 15 to 20 meters through a beam pipe to the monochromator.

The monochromator consists of two parallel crystals which diffract the beam via Bragg's law:

$$n\lambda_{hk\ell} = 2\, d_{hk\ell} \sin \theta_B \qquad (5)$$

where $\lambda_{hk\ell}$ is the wavelength of the X-rays diffracted by the ($hk\ell$) plane with interplanar spacing $d_{hk\ell}$ at angle $2\theta_B$, and n is the harmonic order. Since the beam is diffracted once by each crystal, the beam exits the monochromator parallel to the incident beam displaced by the height

$$H = 2D \cos \theta_B \qquad (6)$$

where D is the distance between the crystal faces. By turning the entire monochromator assembly, the X-ray wavelength can be changed and swept across the energy range of interest. A diagram of the XAS

experiment is shown in Figure 7.

The high intensities of typical operating conditions dictate the usage of ion chambers for the measurement of I_0 and I for the absorption experiments. To fully use the high intensity, the continuously monitoring front I_0 ion chamber is necessary to correct the erratic time and spatial dependence of the SPEAR beam. Solid state ion chambers have been built for use at SSRL. Under low intensity conditions, a NaI scintillator can be substituted for the rear ion chamber. However, under normal conditions, the fron chamber I_0 is a 6" long gas flow chamber and the rear chamber is a 12" long gas flow chamber. Typically, the front chamber gas is adjusted so that it absorbs about 10% of the beam and the rear chamber is adjusted so as to absorb most of the beam. If harmonics of the fundamental beam are large, the gas in the rear chamber may have to be adjusted to minimize the effects of these undesirable energies in the beam. The current generated by the passage of the X-ray beam through the ion chamber is amplified by a Keithly electrometer to a voltage which is then converted to a frequency proportional to that voltage. This voltage is then counted by a computer-interfaced scalar for each ion chamber. The fluorescence detection equipment used was a triplet Si solid state detector which creates a pulse whenever a photon is detected. Each of the three detectors had an active area of 1 cm^2 and sufficient energy resolution to separate the incident fluorescent photons from the scattered photons. Post-detection electronics permitted only pulses with the energy of the fluorescent photons to pass on. These valid pulses were counted by three other computer-interfaced scalars. The dark current of each

input was measured with the beam off before the start of the experimental scan. These dark values were subtracted from each data point. For more details, see J. P. Smith's Ph. D. thesis (43).

A PDP-11 computer was used to control the experiment. A complete description of the software package written by me is contained in Reference 40. Computer-controlled stepping motors change the energy and wavelength of the beam by changing the angular orientation of the monochromator according to equation 5 and change the height of the table supporting the detector and sample array according to equation 6. The computer-controlled counters count the signals I_0, I and F for a time preset by the user. Five regions of variable size with different distances between points and variable measurement times can be specified. The data are written onto floppy disks which are later transferred to magnetic tape which can be read by our analysis programs. The software package at SSRL can also perform some on-line data analysis.

Typically several XAS spectra, each requiring 10 to 25 minutes, were obtained for each sample. Several short scans which can be added later are preferable to one long scan due to the time instabilities of the beam. After injection of electrons into the SPEAR storage ring, the beam intensity slowly decays until the beam unexpectedly loses intensity due to technical difficulties or until the SPEAR operators inject more electrons into the ring. Data collection must cease in any case. This occurs quite frequently. If many short scans are obtained, the few bad scans can be discarded.

Two different types of partial loss of intensity can occur.

First, technical difficulties in the operation of SPEAR can cause a partial loss of beam resulting in a level shift in the data because of the non-linearity of the ion chamber detector system. Second, at certain angles the wavelength of another set of crystal diffracting planes (h'k'ℓ') can equal that of the primary beam (hkℓ). This causes a large decrease in the intensity of the hkℓ beam which is not compensated for by the ion chamber detector system. A so-called "glitch" of limited range is created in the data.

Two different kinds of monochromator energy calibration changes can occur. The first is caused by the new operating conditions each time new electrons are injected into the SPEAR ring. New steering conditions produce a different souce point for the synchrotron beam which means that the X-rays impinge on the monochromator at a slightly different angle changing the calibration. A standard compound was run for calibration during each beam fill. The second change is caused by poor design and maintenance of the monochromator system. For several years, with varying degrees of severity on different beam lines, the monochromator calibration has continuously slipped in one direction from scan to scan. Once the data have been obtained, it is difficult or impossible to compensate adequately for the problem. Most of the data in this thesis were not affected by this problem.

Table 1. Molecular Orbitals for MnO_4^-.

	Eigenvalues	Eigenvectors				
		s	σ_s	σ_p		
a_1	128.75	1.37	-0.98	0.25		
	-112.11	-0.03	0.13	1.00		
	-276.54	0.12	0.92	-0.01		
		d	π			
e	- 72.98	-0.72	0.90			
	-136.56	0.74	0.51			
		p	σ_p	d	σ_s	π
t_2	- 18.83	1.08	-0.06	0.24	-0.42	0.27
	- 49.29	-0.14	0.67	0.80	-0.30	-0.58
	-105.65	0.02	-0.69	0.13	-0.07	-0.67
	-126.26	-0.17	-0.35	0.63	-0.17	0.49
	-260.45	0.03	-0.02	-0.16	-0.96	0.03
		π				
t_1	- 96.40	1.00				

From Ballhausen and Gray, Reference 41. Note: the eigenvalues are in units of wavenumber, i.e. 1/cm.

Figure Captions

Chapter II

Figure 1. Normalized K-shell absorbance of AsF_3. (a) is a scale plot; (b) is expanded to an arbitrary scale. For comparison, these Se^{+3} atomic states (11), calibrated such that the $4s^2p$ state is coincident with the "white peak," are plotted. Se^{+3} states approximate the $(As^*)^{+3}$ states, if the relaxed core approximation is assumed.

Figure 2. Normalized K-shell absorbance of AsF_5. (a) is a normalized plot; (b) is expanded to an arbitrary scale. For comparison, these Se^{+5} atomic states (11), calibrated such that the 4p state is coincident with the "white peak," are plotted. Se^{+5} states approximate the $(As^*)^{+5}$ states, if the relaxed core approximation is assumed.

Figure 3. Molecular orbital energy level diagram for MnO_4^-. From C. J. Ballhausen and H. S. Gray, Molecular Orbital Theory, Benjamin/Cummings Publishing Co., Inc., Reading, Mass. (1964).

Figure 4. Normalized K-shell absorbance of $KMnO_4$. The predicted molecular orbital final states are indicated by the labels 2e, $4t_2$, $5t_2$, and $3a_1$ from Figure 3 and Table 1.

Figure captions, Chapter II, continued

Figure 5. Normalized K-shell absorbance of α-MnO_2. The predicted molecular orbital final states are indicated by the labels 2e, $4t_2$, $5t_2$, and $3a_1$ from Figure 3 and Table 1.

Figure 6. A schematic drawing which shows the electron interference patterns which cause the EXAFS modulations. The atom A absorbs the photon while the atom B backscatters the "ejected" photoelectron. For energy E_1, the electron wave interferes constructively while for energy E_2, it interferes destructively which causes an absorption modulation.

Figure 7. Schematic drawing of the XAS measurement apparatus.

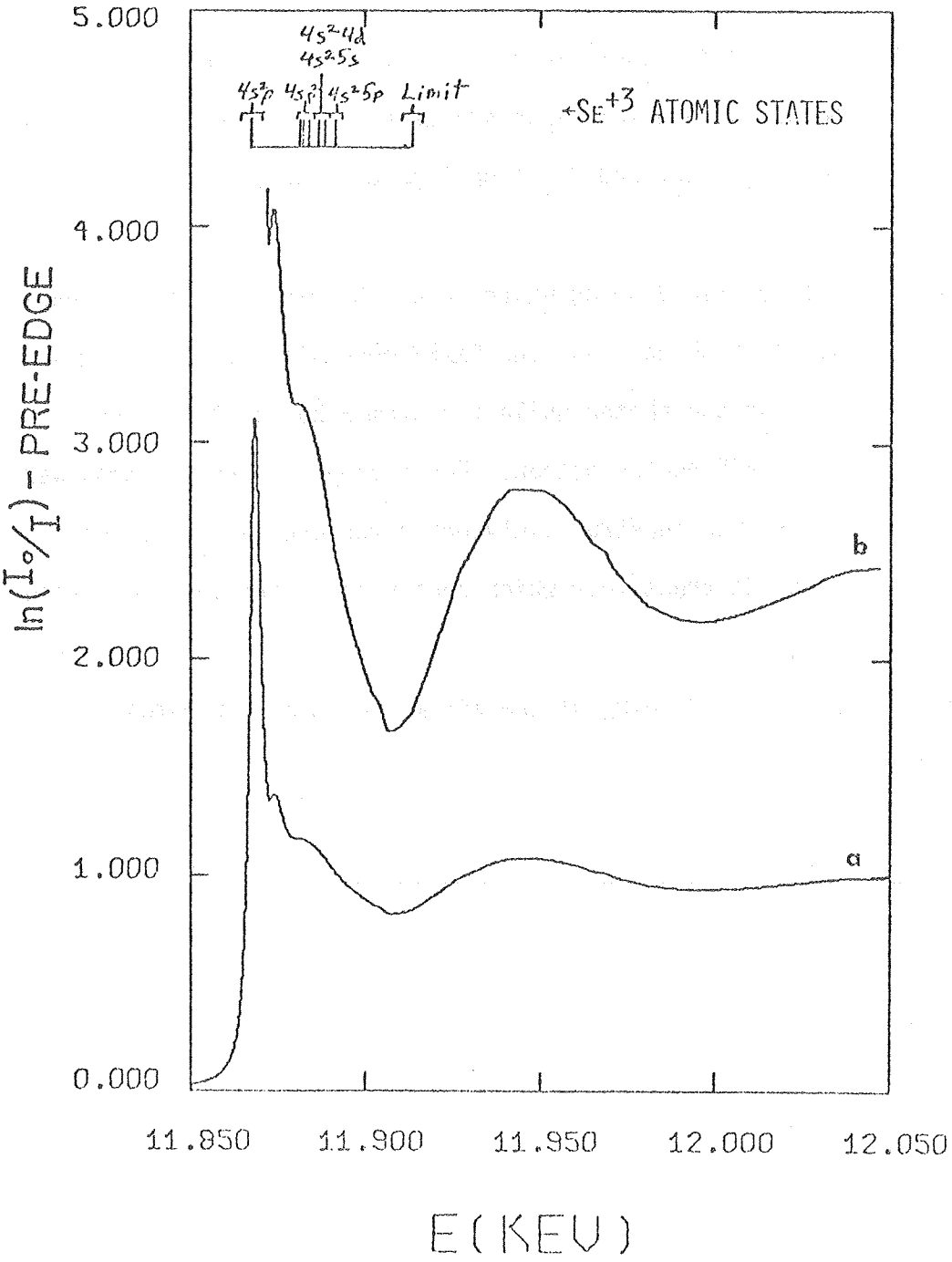

XBL 798-10992

CHAPTER II

Figure 1.

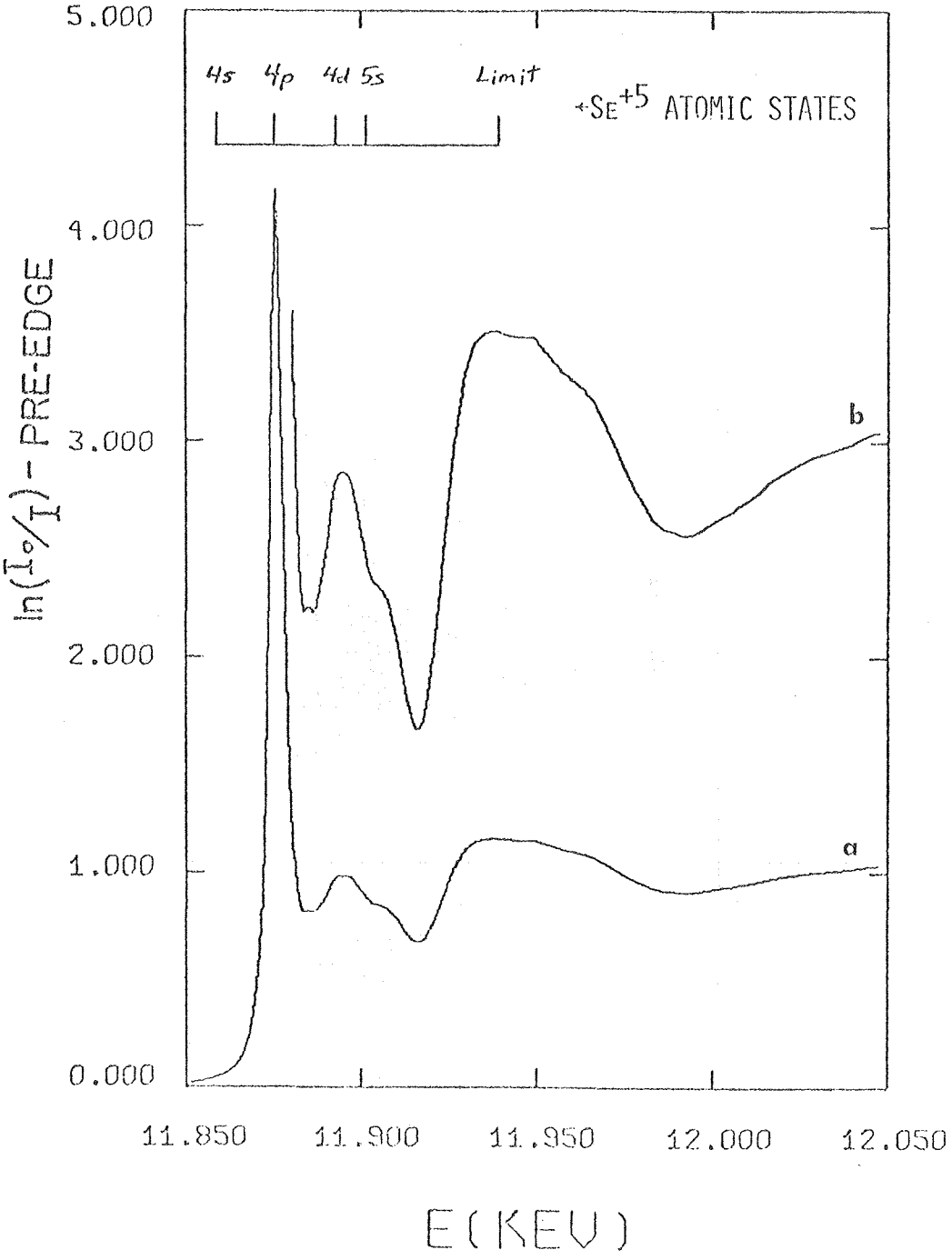

XBL 798-10993

CHAPTER II

Figure 2.

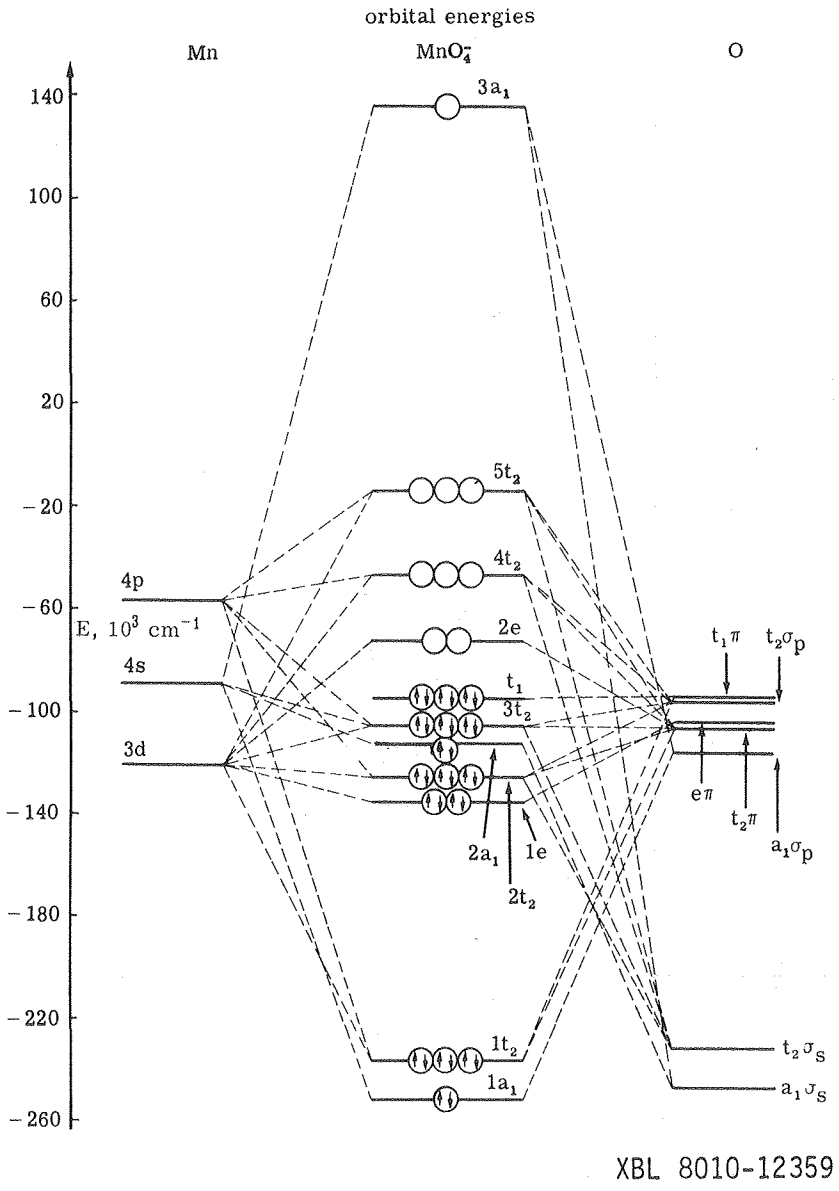

XBL 8010-12359

CHAPTER II

Figure 3

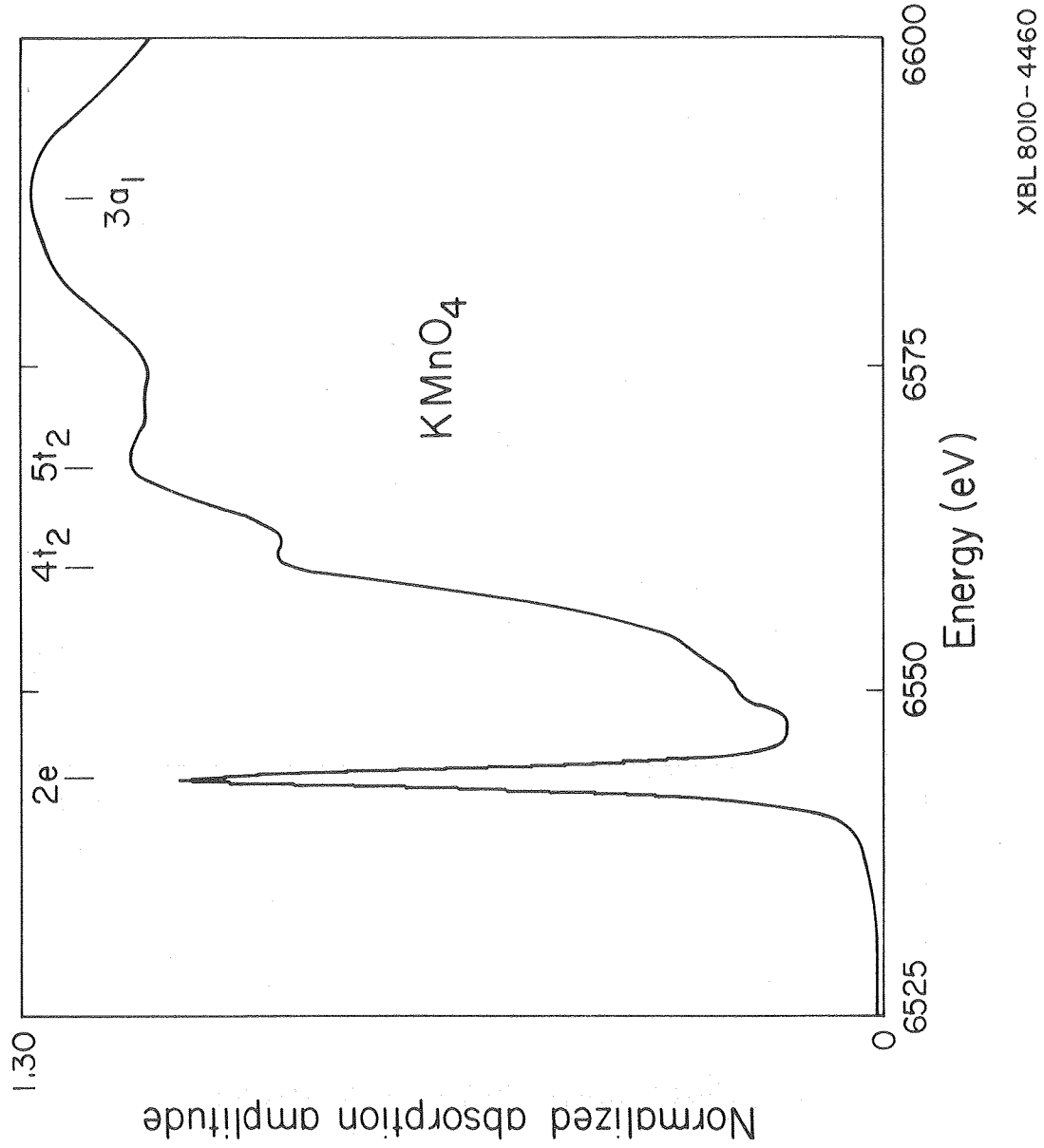

XBL 8010-4460

CHAPTER II

Figure 4.

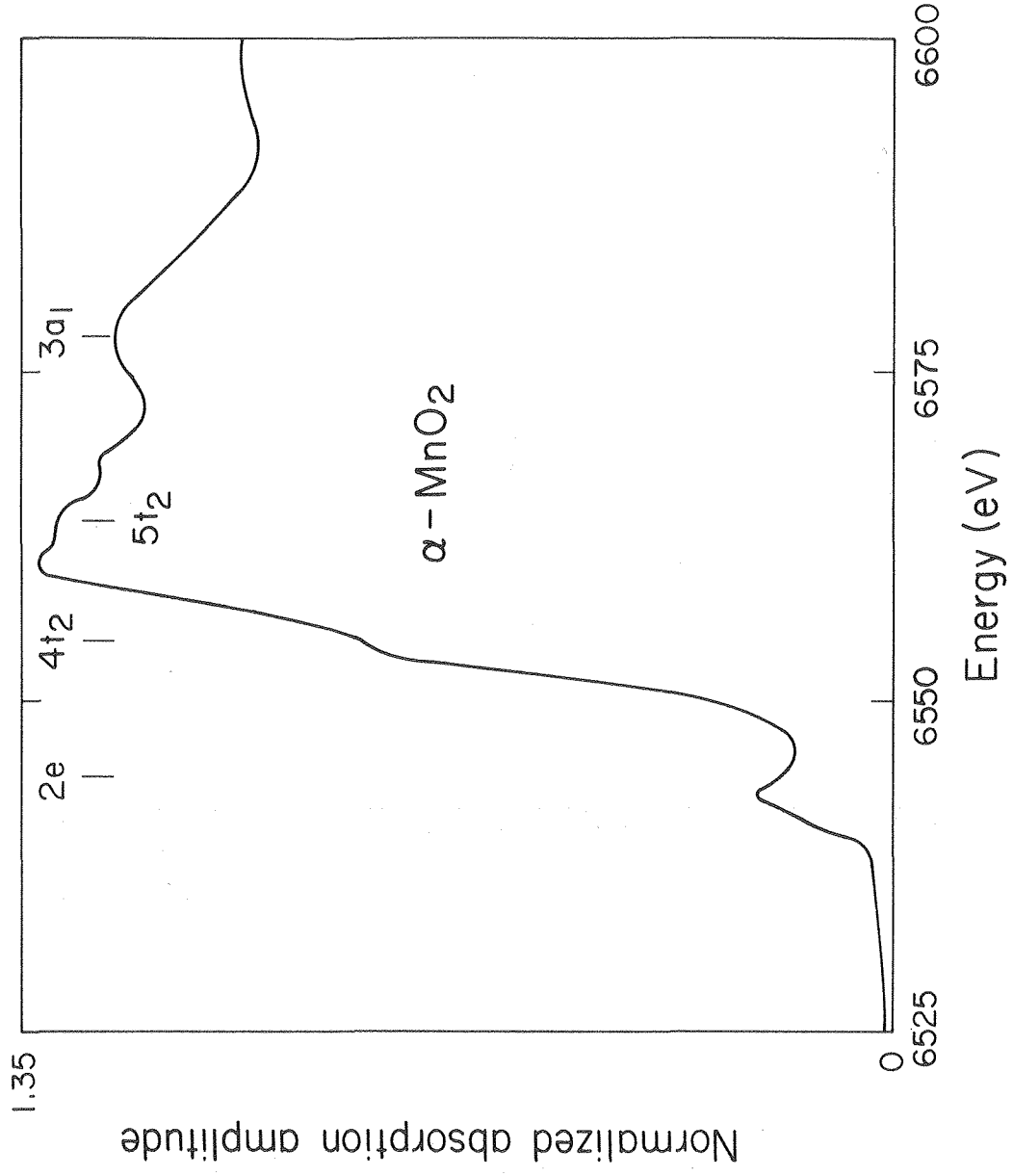

XBL 8010-4462

CHAPTER II

Figure 5.

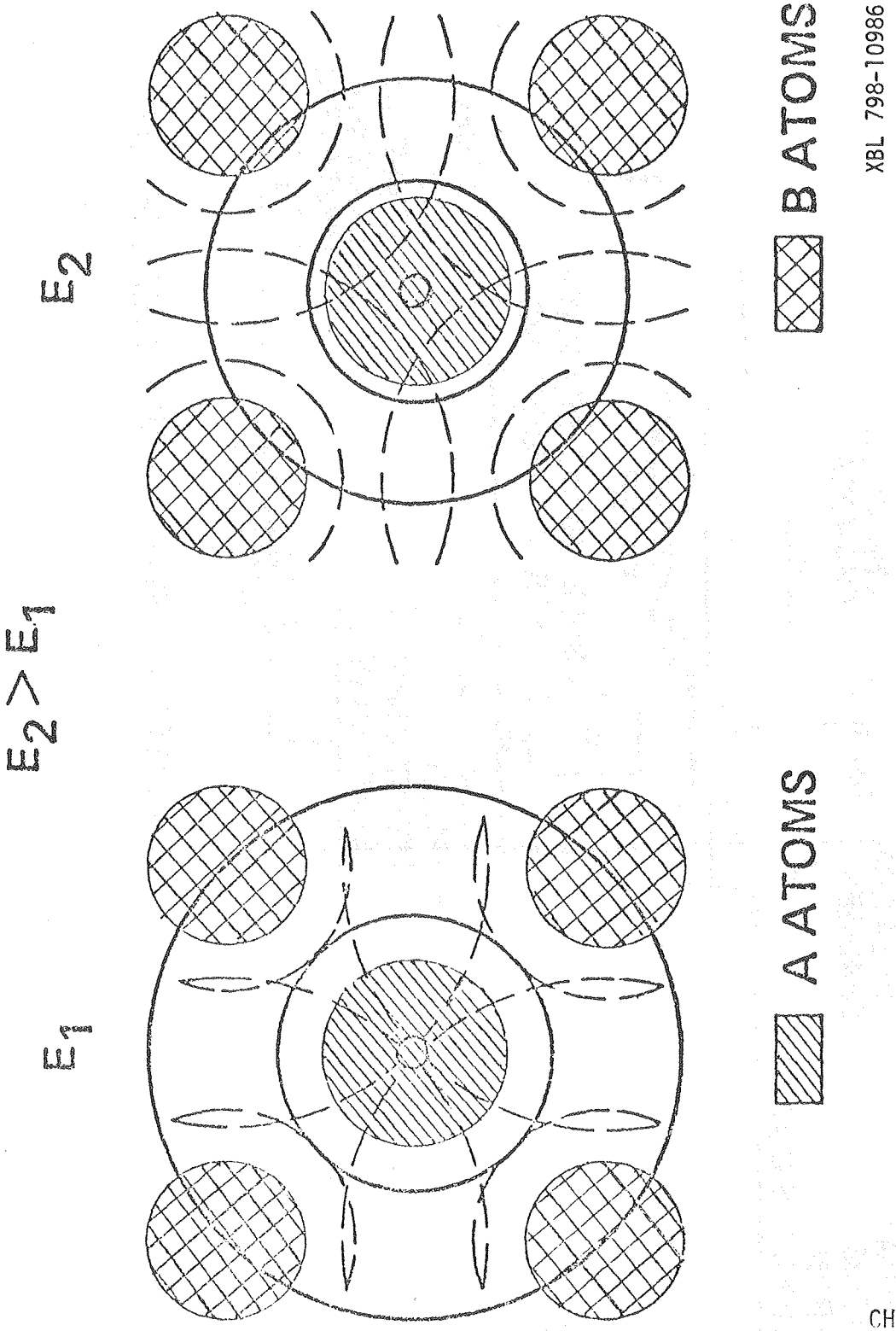

CHAPTER II

Figure 6.

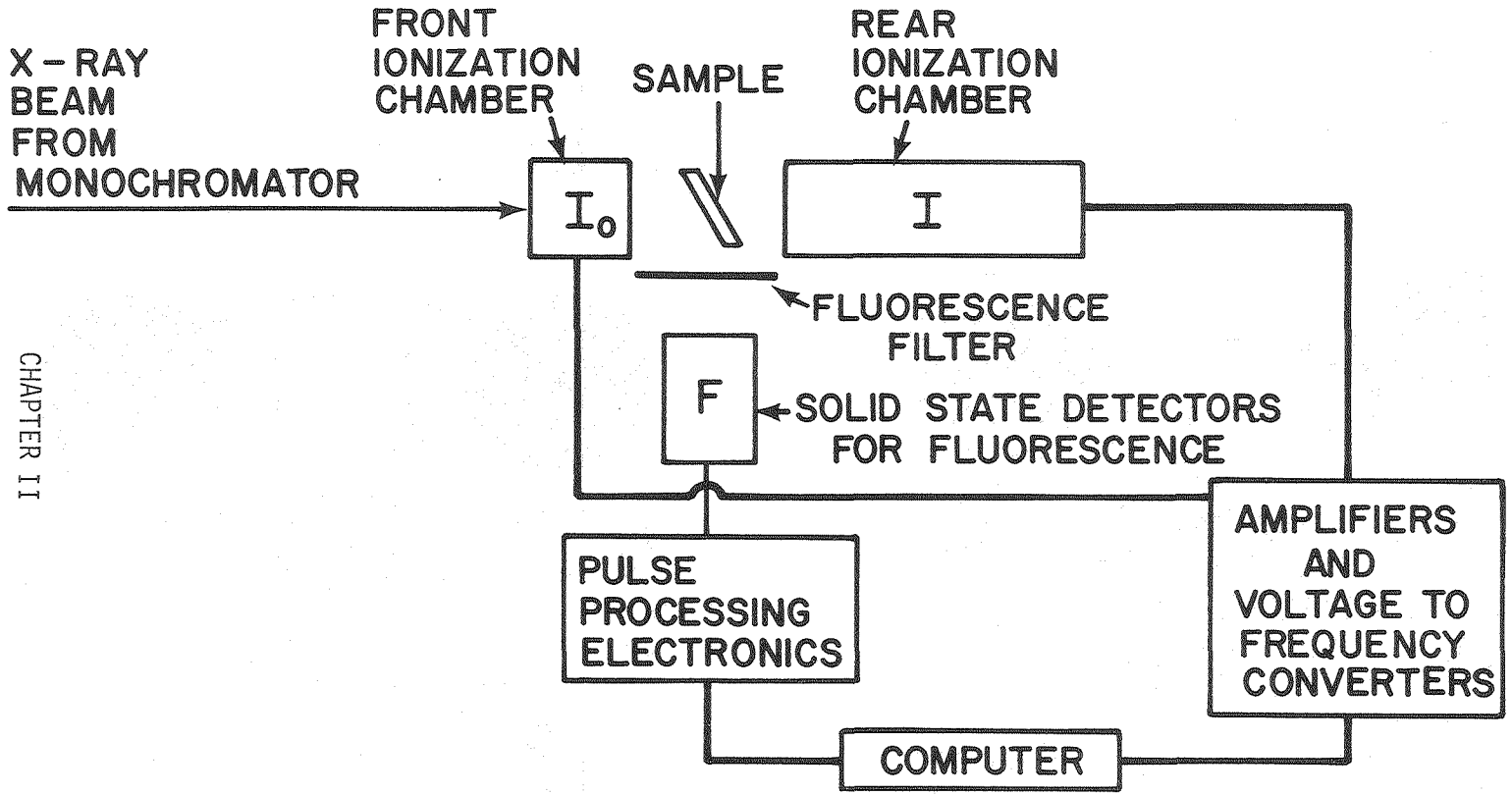

APPARATUS FOR EXAFS MEASUREMENT

XBL778-4525

CHAPTER II

Figure 7.

References

Chapter II

1. W. Kossel, Z. Physik, 1 (1920) 119-134.
2. R. de Kronig, Physik, 70 (1931) 317-323.
3. L. G. Parratt, Rev. Mod. Phys., 31 (1959) 616-645.
4. U. C. Srivastava and H. L. Higam, Coord. Chem. Rev., 9 (1972-73) 275-310.
5. R. A. Van Nordstrand, Non-Crystalline Solids, ed. V. D. Frechette, J. Wiley & Sons, N.Y. (1958) 168-198.
6. R. A. Nordstrand, Handbook of X-rays, ed. E. F. Kaeble, McGraw-Hill Book Co., N.Y. (1967) 43-1 to 43-18.
7. E. Vainshtein, R. Ovrutskaya, B. Kotlyar and U. R. Linde, Soviet Physics: Solid State, 5 (1964) 2150-2153.
8. S. Cramer, T. Eccles, F. Kutsler, K. Hodgson and L. Mortenson, J. Am. Chem. Soc., 98 (1976) 1286-1287.
9. H. L. Higam and U. C. Srivastava, Chem. Comm., 14 (1971) 761-763.
10. R. G. Shulman, Y. Yafet, P. Eisenberger and W. Blumberg, Proc. Nat'l. Acad. Sci.- USA, 73 (1976) 1384-1388.
11. C. E. Moore, Atomic Energy Levels, Vol. II (1952) National Bureau of Standards (U.S.) Circular 467.
12. J. E. Muller, O. Jepsen, O. I. Andersen and J. W. Wilkens, Phys. Rev. Letters, 40 (1978) 720-722.
13. K. Tsutsumi, O. Aita and K. Ichikawa, Phys. Rev. B, 15 (1977) 4638-4643.
14. L. V. Azaroff, Rev. Mod. Phys., 35 (1963) 1012.
15. R. de L. Kronig, Z. Physik, 70 (1931) 317.
16. R. de L. Kronig, Z. Physik, 75 (1932) 191.

References, Chapter II, continued

17. T. Hayasi, Sci. Repts. Tohoku Univ., 33 (1949) 123.

18. T. Hayasi, Sci Repts. Tohoku Univ., 33 (1949) 183.

19. R. de L. Kronig, Z. Physik, 75 (1932) 468.

20. H. Petersen, Z. Physik, 80 (1933) 258.

21. D. R. Hartree, R. de L. Kronig and H. Petersen, Physica, 1 (1934) 895.

22. A. I. Kostarev, Zh. Eksperim. I Teor. Fiz., 11 (1941) 60.

23. A. I. Kostarev, Zh. Eksperim. I Teor. Fiz., 19 (1949) 413.

24. T. Shiraiwa, T. Ishimura and J. Sawada, J. Phys. Soc. Japan, 13 (1958) 847.

25. T. Shiraiwa, J. Phys. Soc. Japan, 15 (1960) 240.

26. A. I. Kozlenkov, Izv. Akad. Nauk. SSSR, 25 (1961) 957.

27. D. E. Sayers, Ph. D. Thesis, University of Washington (1971).

28. D. E. Sayers, F. W. Lytle and E. A. Stern, Advances in X-Ray Analysis, Vol. 13, Plenum Press (1970).

29. E. A. Stern, Phys. Rev. B, 10 (1971) 3027-3037.

30. B. M. Kincaid, Ph. D. Thesis, Stanford University (1975).

31. B. M. Kincaid and P. Eisenberger, Phys. Rev. Lett., 34 (1975) 1361-1363.

32. C. A. Ashley, Ph. D. Thesis, Stanford University (1974).

33. C. A. Ashley and S. Doniach, Phys. Rev. B, 11 (1975) 1279-1288.

34. T. M. Hayes and P. N. Sen, Phys. Rev. Lett., 34 (1975) 956.

35. T. M. Hayes, P. N. Sen and S. H. Hunter, J. Phys. C: Solid State Phys., 9 (1976) 4357-4364.

36. P. A. Lee and J. B. Pendry, Phys. Rev. B, 11 (1975) 2795.

37. P. A. Lee and G. Beni, Phys. Rev. B, 15 (1977) 2862-2883.

References, Chapter II, continued

38. B.-K. Teo and P. A. Lee, J. Am. Chem. Soc., 101 (1979) 2815.

39. J. Jaklevic, J. A. Kirby, M. P. Klein, A. S. Robertson, P. Eisenberger and G. S. Brown, Solid State Comm., 23 (1977) 679-682.

40. J. A. Kirby, Manual for EXAFS Program, Lawrence Berkeley Laboratory Report No. UCID-3952, Berkeley, CA (1977).

41. C. J. Ballhausen and H. B. Gray, Molecular Orbital Theory, Benjamin/Cummings Publishing Co.,Inc., Reading, Mass. (1964).

42. F. S. Goulding and R. H. Pehl, "Semiconductor Radiation Detectors", in Nuclear Spectroscopy and Reactions, Part A, Academic Press, N.Y. (1974).

43. J. P. Smith, Ph.D. Thesis, University of California, Berkeley (1978).

C H A P T E R III

EXTENDED X-RAY ABSORPTION FINE STRUCTURE (EXAFS) DATA ANALYSIS AND COMPARISON OF THE TWO MAJOR PHOTOELECTRON WAVEVECTOR SPACE CURVE FITTING MODELS

I. Introduction

There has been a great resurgence in activity in X-ray absorption spectroscopy (XAS) in the last decade. The main impetus behind this renewal of interest has been two major developments. First, the development of a good theoretical understanding of the post-absorption edge modulations of the X-ray photoelectron cross section, known as Extended X-ray Absorption Fine Structure or EXAFS,[1,2,3] has permitted the use of XAS as a tool for studying the local structures of many different non-crystalline materials, such as glasses and metalloproteins. Second, the availability of intense synchrotron radiation X-ray sources permits a sufficiently large data accumulation rate that samples which are dilute in the element of interest may be studied successfully.[4]

The purpose of this presentation is two-fold. First, one methodology for analyzing EXAFS data from acquisition to completion of curve fitting will be presented. Most of the steps described here are generally followed by others doing EXAFS studies; however, they have not been enumerated in any one publication but are spread throughout the literature. Some of the alternative procedures used by other researchers will be described. Second, a very extensive comparison of the two main EXAFS models that are used to fit photoelectron wave vector space EXAFS spectra will be presented and current limitations of this method of curve fitting analysis will be discussed. It should be noted that up to a certain step the same data processing procedures are used for X-ray Absorption Edge Spectroscopy (XAES) and so appropriate references are contained in the text.

II. Presentation Outline

To understand many of the analysis procedures, certain features of the current EXAFS theory must be presented. Section III thus contains a brief discussion of EXAFS theory.

Section IV contains the description of the data preparation and preliminary analysis. The description is specialized for absorption mode data collection[5] and for data which does not exhibit any unusual characteristics which require special procedures. The special procedures used to overcome the problems and to process data acquired in the fluorescent X-ray detection mode[6] are deferred to the appendices of this presentation. Subsection A contains the description of the initial processing which results in the normalized X-ray absorption spectrum for the 1s or K shell electrons of the absorbing element in the sample being studied. This subsection and Appendix C describe the spectrum preparation necessary for XAES analysis. Subsection B describes the extraction of the EXAFS pattern from the normalized X-ray absorption spectrum. Subsection C describes the preliminary analysis which utilizes finite Fourier transforms of the EXAFS obtained in subsection B.

A major analysis technique for obtaining accurate results from EXAFS is to simulate the EXAFS by curve fitting in photoelectron wave vector space. Section V is a description of this technique and the two major curve fitting models that have been presented in the literature.

Sections VI through IX contain the results of the application of the analysis process described in Sections III, IV and V to various

manganese and arsenic containing compounds. Section VI contains a brief description of the experimental samples and the experimental method. Sections VII and VIII present the fitting results with just one fitting shell and with multiple fitting shells. Section IX contains the discussion of the fitting results and the conclusions drawn.

The appendices contain descriptions of the methodologies that were developed to handle a number of flaws which occasionally occur in XAS data. Appendix D contains the description of a method to make an approximate elemental identity of ligands of the absorbing atom when the ligands are unknown.

III. EXAFS Theory

The presently accepted theory is an outgrowth of half a century of theoretical work. This theory postulates that the EXAFS is due to a sinusoidal modulation of the photoelectron cross section by the presence of a scattered photoelectron component of the final state wavefunction.[1,2,3] The scattered wavefunction component is not zero in the region of the initial state wavefunction and exhibits a phase shift when compared to the unscattered part of the final state wavefunction. This phase shift has two main components: a slowly varying part due to the presence of the atomic potentials a scattered photoelectron would traverse and, a phase retardation due to the distance between the absorbing and scattering atoms. This retardation is responsible for the sinusoidal modulations (EXAFS), because changing the energy of the photoelectron changes its wavelength and, therefore, the total phase shift.

The normal definition for the EXAFS phenomena is the difference between the observed and the free atom photoelectric cross sections; normalized by the free atom photoelectric cross section, or:

$$\chi(k) = \frac{\mu(k) - \mu_0(k)}{\mu_0(k)} \tag{1}$$

where χ is the photoelectron cross section modulation (EXAFS modulation), $\mu(k)$ is the observed photoelectric cross section, $\mu_0(k)$ is the free atom photoelectric cross section, and k is the photoelectron wavevector defined by

$$k = 2\pi(2m_e\ (E-E_0))^{\frac{1}{2}}/h \tag{2}$$

where E is the incident X-ray energy, E_0 is the binding energy of absorbing electron, m_e is the mass of the electron, and h is Planck's constant.

A generalized form of the present EXAFS theory is presented in Equation 3.

$$\chi(k) = \sum_{i=1}^{n_s} \frac{N_i}{k\ R_i^2}\ e^{-R_i/\lambda_i}\ e^{+\sigma_i k^2}\ |f_i(k,\pi)| \cdot \sin\ (2kR_i + \alpha_i(k)) \tag{3}$$

where n_s = number of backscattering shells, N_i = number of atoms in ith backscattering shell, R_i = distance to ith backscattering shell, λ_i = effective photoelectron mean free path for the ith shell, σ_i = thermal and static disorder parameter (Debye-Waller effect is contained in this parameter), $|f_i(k,\pi)|$ is backscattering amplitude function for the ith shell and $\alpha_i(k)$ = phase shift for the ith shell due to the presence of atomic potentials. In practice it is impossible to deal with the mean free path, so all λ_i's are set to positive infinity ($\exp(-R_i/\lambda_i) \rightarrow 1$).

This form is generally accepted, but in utlizing Equation 3, models must be used for $|f_i(k,\pi)|$ and $\alpha_i(k)$ to obtain accurate structural information from the EXAFS modulation. The models used will be described later.

Further examination of Equation 3 yields the motivation for many of the analysis procedures that were utilized. If it is assumed that $|f_i(k,\pi)|$ and $\alpha_i(k)$ are slowly varying functions of k (and they are[3]), then $\chi(k)$ is essentially a sum of sine waves in k-space with approximate frequencies $2R_i$. This means that if a sufficient number of sinusoidal periods can be observed in the EXAFS, the application of a finite k-space Fourier transform should separate the different ligand distances into unique peaks in the Fourier transform conjugate space (see for example, Figure 9). This conjugate space (called R-space) is not the ligand distances R_i, since $\alpha_i(k)$ has a significant linear term which changes the value of R_i observed in R-space. In practice, the change is approximately -0.5Å. Knowing the approximate value of the peak shift permits estimates of the values of R_i. Also, if the ligand distances are sufficiently different, then the R-space Fourier transform

peaks should be separated. If so, then the different EXAFS sine waves can be studied individually by using the technique known as Fourier filtering described in Section IV.

If it is assumed that $|f_i(k,\pi)|$ and $\alpha_i(k)$ vary from element to element, then it should be possible to make elemental identification of the ligands. Fourier transforms and curve fitting simulations of Equation 3 yield some ligand identification capability. This capability is presented in Appendix D.

IV. Data Preparation and Preliminary Analysis

This section contains a detailed description of the initial data processing leading to the preliminary distance and peak assignments obtained from Fourier transform analysis. The description is somewhat specialized for data collected at the Stanford Synchrotron Radiation Laboratory (SSRL), Stanford University, Stanford, CA, 94305. However, any XAS data collected will require similar processing steps to yield useful results. The three main subsets of this section are: A) Initial Data Processing, which describes the conversion from the format as collected to the normalized XAS spectrum; B) Isolation of the EXAFS, which describes the extraction of $\chi(E)$, and the conversion to photoelectron wavevector space (k-space); and C) Initial Fourier Analysis, which describes the use of finite Fourier transforms to estimate ligand distances, to make tentative elemental assignments, and to separate ligand coordination spheres into individual EXAFS spectra (Fourier filtering).

A. Initial Data Processing

i. Initial transcription

The data collected at SSRL were transported to Lawrence Berkeley Laboratory (LBL) on magnetic tape in a form which contained an entry for each discrete spectral point collected and a description of each spectrum collected. Each entry consisted of the relative angle of the crystal X-ray monochrometer, incident and transmitted photon flux measurements, I_0 and I, (from ion chamber currents) and, if present, the counts obtained from fluorescent X-ray detectors F_j.

Each set of entries is then processed at the LBL computer center to yield individual data scans corresponding to each input channel; i.e., an absorption scan from I_0/I and fluorescent scans from F_j/I_0 or F_j. (The necessity for the unnormalized fluorescent scans is explained elsewhere.[7]) After some processing the individual scans are co-added to obtain one final absorption scan and if collected, individual input channel fluorescent scans.

ii. Initial examination

Each data scan is then examined for experimental aberrations. The most common aberrations are the localized crystal "glitches." The crystal "glitches" are rapid changes in incident photon flux which are due to the monochromator crystal used and its orientation and are restricted to specific X-ray energy regions.[8,9] The glitches are relatively small so removing them does not affect the EXAFS analysis, but they are sufficiently large that if a glitch occurs in the XAES region of the data, the scans are likely to be useless for edge analysis. The spectral points affected by the crystal glitches are usually reproducible from scan to scan, so removal of the glitches by point deletion is

deferred until the final co-added spectrum has been created. An example of a typical crystal glitch can be seen in Figure 1 at approximately 12,150 eV.

Occasionally individual scans will have an aberration similar to a crystal glitch but which does not appear in other scans. To be able to add these scans it is necessary to remove these glitches. This is done by replacing the defective points with a straight line fit between the two points on each side of the glitch. Others have fit polynomials to the data outside the glitch region.[9,10] In theory these two methods are not equivalent since our method maintains the statistical independence of all the spectral points, but in practice the difference is negligible in the final co-added scan.

Another common type of aberration is due to a sudden change in the incident photon flux. Since the absorption detectors are only linear with small flux changes, a sudden large flux change results in sudden spectral changes. Such a spectral change terminates the useable portion of the scan. In general, these truncated scans are not co-added. Techniques for utilizing these scans when needed were developed and are described in Appendix A.

The last aberration occasionally encountered is a shift in the X-ray energy represented by a particular monochromator crystal angle. These shifts are usually produced by small changes in the X-ray source's incidence angle or by the mechanical linkages in the monochromator. The shifts are detected by comparing the positions of the edges and prominent edge features for the different scans of the same sample. The positions were obtained from numerically differentiating a series of polynomial fits, each successive fit centered about the next

spectral point. If any significant shift was detected, then special procedures were used to remove the energy biases before co-adding. These procedures are described in Appendix B. For EXAFS analysis, shifts of the order of a few electron volts are considered negligible since this is a small fraction of the size of EXAFS features. For XAES studies, shifts must be significantly less than an electron volt to be considered negligible due to the narrowness of edge features.

The data scans which survive this initial scrutiny are then co-added, each input channel separately if fluorescence data were collected.

iii. Conversion From Monochromator Angle to X-ray Energy

At SSRL, the incident energy is specified by the step number of a stepping motor that drives the goniometer table upon which the crystal monochromator is mounted. By common convention a certain step number corresponded to the X-ray energy for the K-shell edge of copper foil (approximately 9000eV). The copper point then approximately calibrated the monochromator. The calibration of the X-ray energy in the region of interest was accomplished by using standard compounds which had been previously calibrated, by comparison with metal foils when possible. The standard compounds used in this study were As_2O_3 for the As K-edge and $KMnO_4$ for the Mn K-edge. The absolute accuracy of these energy scales is estimated to be about 2 eV. The internal accuracy is better than 0.3 eV for As and 0.2 eV for Mn.

After calibration of the standard compound scans taken during the same time frame, the co-added scans are then converted to incident X-ray energy or E-space scans.

It is also necessary to convert to the absorption cross section form before further processing can be performed. In the case of absorption scans this is accomplished by utilizing the absorption law or

$$\frac{I_o}{I} = e^{\mu x}$$

Taking the natural logarithm of the spectral values yields a measured spectrum which is proportional to the absorption cross section μ. Unfortunately, the measured spectrum also contains a slowly changing experimental background[7,8] due to the nature of the detection method. This experimental background must be removed.

In the case of fluorescence scans, the source of the measured spectral values is different,[6] so a somewhat different method is used to obtain the K-shell information. The procedure is described in Appendix C.

iv. Pre-edge Background Removal

The measured spectrum has cross sectional contributions from two distinct sources, the absorption from the elemental K-shell of interest and the absorption and scattering from the rest of the electrons in the sample. The unwanted contribution is monotonicly decreasing throughout the spectrum and is the only measured quantity prior to the onset of the K-shell absorption (see Figure 1). It has been modeled by the famous Victoreen formula[11] ($\mu = C\lambda^3 + D\lambda^4$ where λ is the photon wavelength and C and D are fitted constants) and more recently by McMaster, et al., using fits with a third order polynomial in ln(E) where E is the photon energy. When the experimental background has no

structure, i.e., its value is a constant, then the Victoreen formula or the McMaster fits can be used to remove this pre-edge contribution.[8,13] Usually, the theoretical pre-edges are inadequate.[7,10,14] Our preferred pre-edge background removal is to subtract a quadratic fit of the McMaster form $(a_0 + a_1 \ln(E) + a_2 (\ln(E))^2)$, fitting the spectrum from 350 - 500 eV to 50 eV below the edge onset. The fit is extrapolated over the rest of the spectrum. A different type of fit is used if the preferred method yeilds an extrapolation which exhibits any significant curvature. The presence of curvature in the pre-edge fit causes problems with later steps. Figure 1 contains a good pre-edge fit. A polynomial in E is generally not used because it often exhibits curvature when it is extrapolated.

After the pre-edge background is removed the spectrum should be similar to Figure 2.

v. Post-edge Normalization

The detection methods used do not permit determination of the cross section but only the relative cross section. Therefore, all XAS spectra are normalized to an edge rise of 1 at the same energy. This is equivalent to determining the absorption cross section $\mu(E)$ per absorbing atom (see Equation 1). This is done by fitting a polynomial to the post-edge region of the pre-edge removed spectrum from 300 eV above the edge to the end of the spectrum. This fit is extrapolated to 50 eV above the edge. The normalized spectrum is then created by dividing the ordinate values by the extrapolated fit value. The normalized spectrum obtained from $CsAsF_6$ (Figure 1) is presented in Figure 2 with its normalizing fit.

The normalized spectrum is the common source for both EXAFS and XAES analysis. For XAES analysis, the normalized spectra of different samples are compared since they represent the normalized absorption cross sections. For EXAFS analysis, it is necessary to obtain $\chi(k)$.

B. Isolation of EXAFS

This subsection describes the extraction of the EXAFS, $\chi(k)$, from the normalized absorption cross section spectrum, $\mu_0^*(E)$. Using Equation 1, all that should be necessary is to convert to k-space using Equation 2, subtract the normalized free atom absorption cross section, $\mu_0^*(k)$, from $\mu^*(k)$, and divide by $\mu_0^*(k)$.

The normalized free atom cross section, $\mu_0^*(k)$, can be obtained from using either the Victoreen formula[11] or the McMaster, et al., fits.[12] An example of the McMaster fit for As, $\mu_m^*(E)$, is plotted in Figure 3 with the normalized spectrum, $\mu^*(E)$, for $CsAsF_6$.

Comparison of $\mu_m^*(E)$ in Figure 3 with the fit in Figure 2 shows that there is significant curvature in the background for $CsAsF_6$. Therefore, it is not practical to use Equation 2 to obtain $\chi(k)$. Instead, Equation 1 is modified to

$$\chi(k) = \frac{\mu^*(k) - B^*}{\mu_0^*(k)} \qquad (4)$$

where B* is a function that includes both μ_0^* and the experimental background. Equation 4 is the form of $\chi(k)$ generally used.[5,7,8,9,10,13,14] In order to utilize Equation 4 it is necessary to transform to k-space and to determine the post-edge background B*.

i. Determination of E_o

In order to convert to k-space it is necessary to determine E_o, the K-shell binding energy. Currently, E_o cannot be easily determined experimentally, so an approximate value is chosen. A reasonable choice is 10 eV above the highest energy for the major edge transition in the samples being studied. The EXAFS region does not begin until at least 50 eV above the edge, so a sizable error can be tolerated because k varies more slowly than the energy (Equation 2). The important point is to use the same value for E_o for all the samples being studied of the same absorbing element, because changing E_o changes the effective distance results. The values used in this study are 6565 eV for manganese and 11932 eV for arsenic.

Once E_o is chosen then $\mu^*(E)$ is converted to $\mu^*(k)$.

ii. Post-edge Background Removal

Various techniques have been used to generate B*. The most prominent procedures have been Fourier filtering,[13] polynomial fits,[8,15] cubic spline fits[9,10,16] and a running average smooth[7,14] that was suggested by Lytle.[17]

A Fourier filter is accomplished by removing some frequencies from a Fourier transform and then inverse transforming. The resultant inverse transform is similar to the original source except that the undesired frequencies are missing. In this particular case, the normalized spectrum has a straight line subtracted (to yield an average value of zero) and the spectrum is converted to k-space. This k-space spectrum is Fourier transformed. The remaining part of B* is expected to be slowly varying so its major transform contribution should be

near zero effective distance in R-space. Thus, to remove the last remnants of B*, the low values in R-space (less than 1Å) are zeroed, and the filtered transform is inverse transformed to k-space.[13] This technique is adequate when the nearest ligands are at least 2.5Å away and the remaining part of B* is small. If the first ligand is too close or if B* has significant curvature, it will be necessary to remove part of the finite Fourier transform peak generated by the nearest ligand when B* is removed. Removing part of a transform peak in R-space distorts the resultant k-space sine wave.

Polynomial fits will often work if B* has little curvature. However, a polynomial of a least 4th order in E-space or k-space is usually required to fit B*. With this order of polynomial the fit will follow the EXAFS when the sample has close (1.6 to 2.0Å), low atomic number first ligands. This removes part of the EXAFS and is, therefore, unacceptable. With long first ligand distances (greater than 2Å) and high atomic number ligands, polynomial fits will often be satisfactory.[8]

Cubic spline fits usually work well in matching most of B*. But the cubic spline leaves a significant background peak in the Fourier transform between 0.4 and 0.8Å.[18] If the first ligand distance is 1.8Å or less, then the R-space transform distance will be less than 1.3Å. The residual background peak is likely to interfere with the ligand peak.

iii. Running Average Smooths

The running average smooth in k-space is the method used in

this work. If B* has any significant curvature, a quadratic polynomial fit is first subtracted from the spectrum in either E-space or k-space, the best fit being used. Then the running smooth is applied after the k-space values have been equally spaced (linearized). A first order smooth, S^1, is obtained by averaging all the spectral values in a fixed k-space interval centered about each k-space point. At the extremes of a spectrum a quadratic fit has been used to estimate the smooth value. This process can be successively repeated as often as necessary to obtain the desired smoothing. Usually a third order smooth, S^3, was used (smooth of the smooth of the smooth $\equiv S^3$). The advantage of the running smooth is that it removes the same low frequencies everywhere in the k-space spectrum because the number of points used in each average is the same everywhere. The upper limit of the frequencies removed is only dependent on the width of k-space interval used and thus is easy to adjust and control so that negligible amounts of the EXAFS are removed.

Examples of various running smooths applied to $CsAsF_6$ are presented in Figure 4. In this sample, the EXAFS period is approximately 1.2Å^{-1}. Therefore, to avoid removing the EXAFS either a high order smooth is required (ex., S^5) or a k-space interval significantly larger than 1.2Å^{-1} is needed. To illustrate this statement, several different choices of smooths are included in Figure 4. Figures 4b to 4f are plots of the following smooths: (b) a first order smooth (S^1) with a 2Å^{-1} interval; (c) a third order smooth (S^3) with a 1.2Å^{-1} interval; (d) S^3 with a 2Å^{-1} interval; (e) S^3 with a 4Å^{-1} interval; and (f) a fifth order smooth (S^5) with a 2Å^{-1} interval. It is obvious that smooths (b)

and (c) follow the EXAFS and, therefore, are unacceptable. Smooths (e) and (f) are also unacceptable because they do not follow the large dip in B* at low k values. Thus, smooth (d) is most likely to be close to B*. The usual problem with B* removal is to determine when an adequate approximation to B* has been obtained.

The smooth chosen resulted in small Fourier transform R-space values near R = 0 $\mathring{A}$ (typically less than one-tenth of the largest EXAFS peak) and in negligible change in the first ligand's transform peak. As a final check the smooth used is plotted with a quadratic fit subtracted, so that the frequencies contained in the smooth can be examined.

It should be noted that special care must be taken at low k-values since a quadratic fit is used instead of the running smooth. Control of the fit's shape is accomplished by selecting the lowest k-space spectral point to keep during the smoothing process. Since spectral points with k less than $2.5\mathring{A}^{-1}$ are never used in EXAFS analysis, selecting the lowest k value does not affect the results as long as a good approximation of B* is obtained (see Figure 4).

A single well-chosen smooth is usually sufficient for B*. However, a considerable part of EXAFS analysis utilizes the function $k^3\chi(k)$ and its Fourier transform, $\phi_3(R)$, which is described in the next section. So, occasionally, a second smooth is needed to remove the residual part of B* that may exist at high k values when the quadratic fit at the end of the smooth does not model B* well enough. Generally, the same smooth used for B* is applied to $k^3(\mu(k) - B^*)$.

Then this second fit is subtracted from $k^3(\mu(k) - B^*)$ and the k^3 factor is removed upon multiplication by k^{-3}.

The normalized spectrum with B* subtracted needs only to be divided by $\mu_0^*(k)$ to yield $\chi(k)$.

iv. Free-atom Absorption Cross Section

As described earlier, the Victoreen formula[11] and the McMaster, et al., fits[12] provide excellent approximations to the free-atom absorption cross section, $\mu_0(E)$. In this work the McMaster fits, $\mu_m(E)$, are used since they are already expressed in photon energy rather than wavelength. $\mu_0(E)$ is normalized to obtain $\mu_0^*(E)$ by dividing $\mu_0(E)$ by the value of μ_0 at the reference energy used to create $\mu^*(E)$ from $\mu(E)$ in Section A. $\mu_0^*(E)$ $(= \mu_m^*(E))$ is then converted to k-space to obtain $\mu_0^*(k)$. $\mu_0^*(k)$ is used to obtain the EXAFS spectrum, $\chi(k)$, from $\mu^*(E) - B^*$ as defined by Equation 4.

It should be noted that others[8,19] have used B* as an approximation of $\mu_0^*(k)$. This choice is reasonable when the experimental background contribution to B* is small. This is generally the case when the sample is concentrated in the element being studied and the incident photon flux does not produce marginal detection conditions.

C. Fourier Transform Analysis

This section describes the procedures used to obtain ligand distance estimates, and to prepare the EXAFS spectrum, $\chi(k)$, and its individual constituents for simulation by curve fitting.

i. The Fourier Transforms Used

Separation of the EXAFS into its various distance components via finite Fourier transform is used as an aid for background removal and as an integral part of the analysis technique described below. As defined in Equation 3, the theoretical form of the EXAFS is a sum of sinusoidal functions with the argument $2kR + \alpha(k)$ so the following Fourier transform can be used to extract structural information[13,20]:

$$\phi_n(R) = \int_{k_j}^{k_f} \{k^n W(k) \chi(k)\}^{i2kR} \, dk \qquad (5)$$

where k_j and k_f are the initial and final k values, W(k) is an apodization window function (to decrease the side lobes in finite Fourier transform), and k^n is a weighting function where n has been varied from -3 to 7 under some circumstances (for an example see Figure 5).

Typically, n is 1 or 3, because Stern and co-workers[1,20] have shown that $\phi_1(R)$ is related to the spatial variation of the scattering matrix and $\phi_3(R)$ is related to the pseudocharge density. In practice the k^n factor is merely a spectral weighting function which allows different portions of $\chi(k)$ to be emphasized in the Fourier transforms. Since the backscattering amplitude function, $|f_i(k,\pi)|$, varies for different elements, the different transforms can be used for ligand identification. This is explained in Appendix D.

Multiplication by k^n with $n > 0$ has other effects on the Fourier transforms. First, it tends to reduce the damping of the EXAFS modulation (see for example, Figure 7). This results in improved peak resolution in $\phi_n(R)$ (see for example, peak narrowing in Figure 8).

Positive values of n also increase the transform noise level since the EXAFS signal to noise ratio is poorer at high k due to signal damping. However, the higher k part of the spectrum more closely resembles the current theory[1,2,3], so a positive value of n is desirable.

EXAFS extends from $k_i = 0$ to $k_f = \infty$, but the analysis must be restricted to a finite region. Using a value of k_i less than 2.5A^{o-1} is not practical since the current theory is not valid at the low k values. The upper limit is solely a function of the experimental conditions. Usually the EXAFS is smaller than the noise upon reaching a k value of 16A^{o-1} (1000 eV above the edge). These practical k limits result in the observation of only a small number of oscillations in the EXAFS. This means that the finite Fourier transform of the EXAFS does not result in just one peak for a single distance, but a series of peaks, the main peak and side lobes (sin x/x type pattern, see Figure 6). These extra peaks interfere with other transform peaks and greatly complicate other analysis tools such as Fourier filtering. Therefore, an apodization window, W(k) in Equation 5, is applied to the k-space spectrum before transforming to reduce the sidelobes. The Kaiser window[21] is used in this work. Kaiser[21] has shown that this type of window is nearly optimal since the maximum transform contribution is concentrated in the main peak for a given peak broadening. A family of Kaiser windows is presented in Figure 5. The Fourier transforms for the square window (W(k) = 1) and two of the Kaiser windows in Figure 5 (curves B and D) are presented in Figure 6. Figure 6 shows that using a Kaiser window of 3.0 (curve 5D) greatly reduces the sidelobes and only slightly increases the width of the central peak. Due

to presence of a finite Fourier transform noise level, the sidelobes of the Kaiser window with Kaiser parameter equal to 3.0 are seldom observed, so this window is used in this work.

Hayes has used a gaussian convoluted with the square window as W(k).[22] Sayers[23] has modified the Hamming window.[24] The use of non-rectangular window functions is discussed in Reference 24 and its application to EXAFS in References 25 and 26.

The Fourier transforms which were used to select the background used for B* (see Equation 4) are $\phi_1(R)$ and $\phi_3(R)$ with a Kaiser window with Kaiser parameter equal to 3.0, k_i = 2.0 - 4.0 A^{-1} and k_f = 13.5 - 18.0 A^{-1}, depending on the spectrum examined.

ii. Initial Ligand Distance Estimations and Element Identification

The Fourier transform is used to estimate ligand distances and to make an approximate element identification of the ligands. As a qualitative example, consider As_2O_3. The EXAFS, $k^2\chi(k)$ for As_2O_3 is plotted in Figure 7. In Figure 8 the power spectra of the Fourier transforms ϕ_1 and ϕ_3 of As_2O_3 are plotted (Kaiser window, k_i = 4.0 A^{-1} and k_f = 15.6 A^{-1}). The first peak has an effective distance of approximately 1.4A ($|\phi_3|$) and arises from oxygen ligands at an average distance of 1.80A. The second peak has an effective distance of 2.7A ($|\phi_3|$) and contains a mixture of oxygen ligands with an average distance of 3.02A and or arsenic ligands with an average distance of 3.23A. The two peaks thus show that the real distances are shortened by approximately 0.4A when presented in R-space. A further examination

of Figure 8 shows that the relative peak magnitudes between the first and second peaks increased due to the extra k^2 multiplication factor used before transforming ($|\phi_1|$ compared to $|\phi_3|$). Since the only difference between the two peaks is the presence of the As in the second peak, this seems to indicate a possible way to distinguish between different ligand elements.

The major reason for the relative magnitude change is demonstrated in Figure 9. The three curves in Figure 9 are theoretical backscattering amplitudes, $|f_i(k,\pi)|$, obtained from calculations by Teo and Lee[27], one of the two backscattering models discussed later. The three main observations from Figure 9 are, as the atomic number increases: (1) the maximum point of the backscattering cross section moves to higher k values; (2) the total backscattering capability increases; (3) the heavier elements scatter more effectively at high k values. These characteristics imply that if two different atoms are at the same distance, then the heavier one will backscatter more efficiently and if the EXAFS spectrum is multiplied by k^n with $n > 0$, then a heavier atom's transform peak will be preferentially enhanced.[28] This behaviour usually permits the transform peaks of the heavier ligands to be identified.

For a quantitative example, consider the entries in Table 1 which are the result of a typical preliminary Fourier transform analysis of threee different manganese compounds. Examining Table 1(a) shows that with the exception of the first manganese ligands of α-MnO_2, the heavier ligand peaks increased faster with increasing n in the k^n multiplication. In all cases, the oxygen to manganese peak ratio increased

dramatically. In the case of α-MnS, the sulfur to manganese peak ratio increased only from 0.70 to 0.72. This small increase is reasonable when the relative atomic number differences between oxygen, sulfur and manganese, and the NaCl crystal structure of αMnS is considered. First, sulfur is significantly heavier than oxygen so it should also increase significantly with higher n. Also the nearest neighbor Mn atoms in α-MnS are directly behind the first coordination sphere sulfur ligands and, therefore, subject to the well known "focusing effect" of waves passing through a potential.[3] For the Mn ligands in α-MnS, the focusing effect resulted in an amplitude decrease at high k compared to a normal Mn ligand, thereby reducing the k^n amplification.

Table 1(a) also illustrates another problem, the inability to accurately predict the number of ligands in a transform peak from the magnitudes of the Fourier transform peaks except in the case of very similar samples.[8,10] It is not reasonable to assume that the six oxygens in α-MnO_2 scatter twice as well as the six sulfurs in α-MnS. Thus, it is not possible to compare absolute transform peak heights from sample to sample.

Examination of Table 1(b) shows why it is difficult to use Fourier transform peak positions for distance determinations. The transform's peak positions can be shifted by numerous effects including nonlinear phases, spectral noise and variation in backscattering amplitude shapes from sample to sample. However, it has been possible in certain cases, primarily when similar model compounds are available for comparison, for the Fourier transforms to be used to obtain good results.[13,29]

Good initial estimates of the true distances can be obtained for the curve fitting analysis by taking the $k^3\chi(k)$ transform peak positions and adding 0.5Å (Table 1(b)). Also, good initial guesses of ligand elemental composition can be obtained from the relative transform peak heights, the known chemistry of the absorbing element (good estimates of the oxidation state can be obtained from XAES) and the estimated ligand distances. (See Appendix D.)

iii. Pre-curve Fitting Fourier Transform Processing: "Fourier Filtering"

For curve fitting, it is desirable first to perform single shell fits on single isolated transform peaks and then to attempt multishell fits on either "clean" multipeak spectra or single isolated transform peaks. In order to perform single shell fits, the fitted k-space spectrum must represent a single peak distance. These spectra are created by applying a standard technique of digital signal processing; that is "Fourier Filtering", the application of a frequency domain Fourier transform digital filter and subsequently inverse transforming back to the time domain.[30] For EXAFS, the time and frequency domains correspond to k-space and R-space, respectively. Single distance EXAFS spectra are obtained by applying Fourier Filtering isolation windows (generally the modified Hamming window mentioned earlier [23,24]) to resolved R-space Fourier transform peaks and then inverse transforming the windowed result to k-space.

This isolation technique works well if the atomic ligands are well separated in radial distance from the absorbing atom (approximately 1Å). If this separation criterion is not met, then usually

multipeak fits and synthetic modeling will be necessary to obtain accurate results.[31] When two transform peaks are too close together there is not only a large overlap of their sidelobes, but their main peaks will also overlap (see Figure 6). If a Fourier Filtering window separates closely spaced peaks, part of the basic signal of each peak will be removed and the isolated peak will be heavily contaminated with a contribution from the removed peak. The overlap will produce k-space distortions when the inverse transform is performed.

A final "clean" multipeak k-space spectrum is obtained by a variation of the isolation technique. Since high frequency noise (which is observed predominantly at higher R-values even though it is "white" in nature) and the little remaining low frequency background (less than 0.8Å in the Fourier transform) can cause convergence problems when fitting, a very broad filtering window is applied to the Fourier transform to remove these unwanted contributions. The window is set broad enough to not remove any contribution of significance to the EXAFS spectrum, but removes the background and noise. For example, in Figure 8, the left side of the filter would be set to have a value of zero at approximately 0.5Å and a value of unity at approximately 0.8Å and the right side of the filter would be zero at approximately 3.8Å and unity at approximately 3.5Å. (Note, in the case of the transform in Figure 8, it is possible to retain the first sidelobes of the second peak (at 2.0Å and 3.3Å) due to a high signal-to-noise ratio of the EXAFS for this sample. In general, it is not possible to observe the sidelobes due to either the noise level and/or peaks in the transform.)

V. EXAFS Simulation by Curve Fitting in k-space

The next step in EXAFS analysis is to perform simulation curve fits to obtain accurate radial distances, estimates of the number and type of backscattering atoms (see Appendix D), and in certain special cases, estimates of relative structural disorder. There are two types of curve fits that can be performed; fits to the EXAFS modulations directly (usually in k-space) or fits to the Fourier transforms in R-space. R-space curve fitting has been extensively developed by Hayes and coworkers.[22] It seems to be successful when working with the heavier elements such as germanium.[22] Only k-space fitting will be discussed in this work, but R-space fitting should be considered by any potential EXAFS users.

A. Models

The two main backscattering models in use today for k-space fitting are the models proposed by Hodgson and Doniach[15] (H-D model) and by Teo and Lee[27] (T-L model). There is an earlier parameterized version of the T-L model,[32] but the current model has been found to be more useful.[33] The two models are very different.

In the H-D model simple forms are assumed for $|f(k,\pi)|$ and $\alpha(k)$, and E_o is a fixed parameter for each absorbing atom. Known compounds with different backscattering ligands are fit with all the model parameters variable until the best fit is obtained. The best fit results are used to define the model parameters for that particular absorber-backscatter pair.

In the T-L model the values for $|f(k,\pi)|$ and $\alpha(k)$ are obtained from

the published theoretical calculations.[27] When the desired elements are included in the tables of reference 27, the calculated values are used directly. When the desired elements are not calculated, linear interpolations between the values for the published elements are used to obtain the desired model values. In this model, the binding energy of the atom, E_0 (Equation 2) is considered to be an adjustable parameter, primarily to obtain the best fit for the experimental phase with the theoretical $\alpha(k)$. In reference 27, there are two sets of calculations described; one set generated using Herman-Skillman wavefunctions and another set generated using Clementi-Rosetti wavefunctions. All the fits described in this study were performed using the Clementi-Rosetti set. The two sets are not compatible, but are self-consistent and should not be mixed.

To summarize and fill in the details of the models for each fitting shell in Equation 3:

i) Hodgson-Doniach Model (H-D)[15]

$|f_i(k,\pi)| = A_i/k^{\beta}i$

$\alpha_i(k) = a_{0i} + a_{1i}k + a_{2i}k^2$

Fitting parameters: N_i, R_i

Fixed parameters: $E_0, A_i, \sigma_i, \beta_i, a_{0i}, a_{1i}, a_{2i}$

The H-D fixed parameters used in this study are presented in Table 2.

ii) Teo-Lee Model (T-L)[27]

$|f_i(k,\pi)| = B_i(k)$ (theoretical backscattering amplitude)

$\alpha_i(k) = \alpha_{ai}(k) + \alpha_{bi}(k)$ (theoretical absorber and backscatter phase shifts)

Fitting parameters: σ_i

Fixed parameters: B_i, α_{ai}, α_{bi}

In reference 27, only certain discrete k values are reported, so quadratic fits through three adjacent points of the B_i, α_{ai} and α_{bi} model values are used to extrapolate between the discrete values. The quadratic fits permit approximation of the curvature exhibited in the model calculations.

Comparison of these two models leads to several immediate conclusions. The H-D model has no free parameters to simulate EXAFS amplitude changes since σ_i is used as part of the amplitude model. Therefore, the H-D model cannot be used to study disorder effects. However, as will be discussed later, there is a strong fitting correlation between N_i and σ_i in the T-L model. Thus, the T-L model must be used with care when studying disorder effects. Next, since the H-D model has only one amplitude (N_i) and one phase fitting parameter (R_i), neither of which affect the "shape" of their respective functions, while the T-L model has parameters which affect both the amplitude and phase magnitudes (N_i and R_i) and "shapes" (E_o and σ_i), the T-L model is expected to yield much better fits. For this reason, only the final results of the fitting process may be used when the two models are compared. Finally, since the H-D model requires reference fits, the effect of the choice of the reference compounds must be considered when evaluating that model.

B. Fitting Method Used

The fitting process minimizes the average weighted least squares error between the input EXAFS spectrum (filtered single or multiple

peaks) and the EXAFS model presented in Equation 3. The fitting equation minimized is:

$$F = \sum_{i=1}^{m} \{y_i - \chi(k_i)) \cdot k_i^n\}^2 / m \qquad (6)$$

where F is the average least squares error, m is the total number of fitted points (typically equal to 200), y_i is the ith EXAFS spectral point, $\chi(k_i)$ is the ith fitting model value, and n is the order of the fitting weight function used. In this work, n is always equal to 3 since in most cases the observed EXAFS amplitude of $k^3\chi(k)$ is approximately constant. This means that the fitting process places the same significance on low k fitting errors as on high k fitting errors. If one desires to weight different parts of the spectrum differently, then different values of n can be used ($n < 3$ emphasizes the low k region; $n > 3$ emphasizes the high k region).

Examining Equation 3 and the fitting models, it is obvious that there are both linear and nonlinear fitting parameters. The linear parameters are fit easily using the standard matrix method for solution of simultaneous linear equations which require no starting values.[34] To facilitate convergence of the nonlinear parameters, the linear parameters are recomputed whenever the nonlinear parameters are changed. To minimize F_o with the nonlinear parameters requires more sophisticated methods and good starting values. The two methods which are used for the nonlinear parameter determinations are both contained in a standard fitting package that was developed at the European high energy physics laboratory CERN. The fitting package has the name MINUIT and

is an improved version of the original MINUIT which was developed in the 1950's.[35] The two methods used from the package were a simplex method[36] and the Davidson variable matrix algorithm.[37]

Simplex minimization is a very simple method.[36] The information about the function to be minimized $F(X_1, \ldots X_n)$ is contained in n+1 evaluations of F. These n+1 points form a simplex, the simplest n-dimensional geometric figure (has only n+1 corners). The point in the simplex with the largest value of F is reflected through the center of gravity of the remaining points in such a way that a better value is obtained. Thus, a better simplex is obtained. This process continues until no improvement can be made. With all single shell fits and many of the multishell fits, this method minimized Equation 6 when good starting values for the nonlinear parameters were used (R_i for H-D and R_i, E_{oi} for T-L models). This means that for those cases, the function F has a well defined and well behaved minimum.

For many of the multishell fits it was necessary to use also the Davidson variable matrix algorithm method. In this method, the minimum is obtained by making successive approximations to the covariance matrix. This is done by attempting to zero the residual vector formed by the product of the covariance matrix and the gradient of the function $F(X_1, \ldots, X_n)$ at the current estimate for the minimum point. This residual vector is used to obtain a better estimate of the minimum's location, and the process continues until the magnitude of the residual vector is below a certain value. This method has the ability to distinguish between closely spaced local minima and the absolute minimum.[35] This ability was necessary on many of the multishell fits.

A number of the nonlinear parameters are highly correlated and the models are sufficiently inaccurate that a change in one parameter can be compensated for by a change in another parameter. This results in many local minima.

The combination of these two nonlinear fitting minimization methods was always able to find the absolute minimum value of the average least squares error. (In the difficult samples many different sets of starting values were used and in all cases the same final minimum was obtained.)

C. Choice of Starting E_0 in the Teo-Lee Model

For both models, good starting values for R_i can be obtained from the Fourier transform analysis. In the T-L model, σ_i is the only nonlinear amplitude parameter. It has a low correlation with the other two nonlinear parameters R_i and E_{oi}. Therefore, a starting value of zero was generally used and convergence of σ_i was generally very fast. This leaves the determination of a good starting value for E_{oi}. This determination is complicated by the high correlation between R_i and E_{oi} through the argument $2kR_i$ of the sine function in Equation 3.

The starting E_0 problem was solved by using the method suggested by Lee and Beni[38] in 1977 and a property of the Fast Fourier Transform (FFT) algorithm, the normal way finite Fourier transforms are computed. Lee and Beni suggested that when the proper E_0 is chosen, the peak of the imaginary part of the EXAFS Fourier transform peak coincides with the maximum in the power spectrum peak, after the theoretical phase has been removed from the complex k-space spectrum by multiplication with $\exp(-\alpha_i(k))$. The trick is to generate the complex

EXAFS k-space spectrum in the first place. This is done by using a property of the FFT which is not generally known.

The FFT's in use today have two basic steps. The first is the finite Fourier transform itself. This transforms a real sine wave of frequency f into two peaks in the complex transform conjugate space; one corresponding to frequency f and one corresponding to frequency -f. In an infinite transform these two frequencies are different, but in a finite transform they are really the same frequency. Thus, the second FFT step is the proper conversion of these two peaks into one positive frequency peak. To generate complex k-space spectra the first FFT step is used to generate the two transform peaks. Instead of condensing the peaks into one, the peak corresponding to the negative frequency is zeroed and only the positive frequency peak is retained. The remaining peak is inverse transformed resulting in a complex k-space spectrum. The phase rotation by $-\alpha_i(k)$ is performed. The rotated result is Fourier transformed to R-space and the imaginary and power spectrum peak positions are determined. E_0 is changed and this process is duplicated until the peak position criteria of Lee and Beni is obtained. In general, this choice of E_0 is quite good ($\pm$5eV). An example of the transform results of this process is presented in Figure 10.

D. Phase Only Teo-Lee Fits

One of the by-products of the Lee and Beni E_0 determination method is a complex k-space EXAFS spectrum. This k-space corresponds to keeping only the positive frequency part of the complex sine wave expression or:

$$\sin(2\pi ft) = \frac{e^{i2\pi ft} - e^{-i2\pi ft}}{2i} \rightarrow \frac{e^{i2\pi ft}}{2i} \qquad (7)$$

Substitution of Equation 7 into Equation 3 shows that no information has been lost from the EXAFS spectrum, but Equation 3 has been converted to a more versatile form. The complex form permits the user to extract just the amplitude or the phase parts of a single transform peak. Thus, the fitting process can be broken down into separate fits on the phase and on the amplitude. In practice, only the phase fits are performed separately since the largest single source of fitting error is the inability of the amplitude models to fit the observed EXAFS amplitudes well (for example, see Figure 11).

E. Teo-Lee Distance Error Estimates

In the H-D model there is only one phase fitting parameter, so only one distance result is possible. However, in the T-L model both E_o and R_i affect the frequency of the sine waves so a method was devised to estimate the distance error due to the correlation with E_o when fitting with a single shell. First the absolute minimum is obtained. Then a matrix of the fitting error is obtained by varying R_i and E_o about their minimization values. The matrix is then scaled by setting the minimum error equal to zero and the fitting error, which is twice the minimum fitting error, equal to 10. The scaled matrix is plotted and the distances where the fitting error is twice as large as the minimum (value of 10 in the matrix) are used as the estimate of the fitting error.

For example, consider the full single shell EXAFS fit of Figure 11. This minimum fit is used to generate the error matrix in Figure 12. Using the error matrix, the average radial distance from the As to the fluorines is 1.726Å with an estimated error of $\pm$ 0.013 R, E_o for this shell would be 11889.3 eV with an estimated error of +5.0eV and -6.0eV.

The general form of the matrix in Figure 12 is characteristic of all of these matrices. As E_{oi} increases R_i increases so the minimum error "valley" always has a positive slope. If the EXAFS fit is a phase only fit or the amplitude function fits especially well, the "valley" is quite short (estimated errors in R_i and E_{oi} are very small) and "valley" walls are quite steep. If the EXAFS fit is a normal amplitude fit then the "valley" will appear similar to the "valley" in Figure 12. As indicated in Figure 11, the model amplitude does not usually match that of a single peak well, so the amplitude mismatch is compensated somewhat by a frequency mismatch during fitting. This results in a broader minimum "valley" and, therefore, a larger uncertainty in the distance. For this reason both full (with amplitudes) and phase only fits are performed with the Teo-Lee model when single peaks can be isolated. The results of both fits with estimated errors (in parentheses in the tables) are included later.

VI. Samples and Experimental

All of the samples used in these experiments were either obtained from commerical sources or prepared from published methods. Those samples which exhibit environmental sensitivity were kept in special sample cells or in special inert atmospheres to guarantee that the

samples were not contaminated. Data scans for almost all compounds were collected on more than one sample, usually on a different day. The results were compared for consistency.

Experimentally, the standard absorption technique using two ionization chambers, described in great detail elsewhere,[7,8,9,10,14] was used. This technique utilizes ionization chambers for measuring the incident photon flux (I_0) and the transmitted photon flux (I). Generally, the total absorption in the ionization chambers was maintained at approximately 10% for I_0 and 40% for I by selection of the ion chamber gas mixture. The sample absorption was adjusted where possible to be 90% absorbing above the K absorption edge (K-edge).

VII. Single Shell Curve Fitting Results

All the results presented in this section are obtained from single shell fits on the EXAFS spectra created by Fourier Filtering single Fourier transform peaks. For each peak from each sample there are three spectra generated and fit; one for the H-D fits, all with the same E_0, one for the full T-L fits, and one for the phase only T-L fits. If the fitted E_0 obtained was significantly different than the E_0 used to create $\chi(k)$ (a difference greater than 2 eV), then a new EXAFS spectrum was created using the fitted E_0 and the fits were redone. If these two E_0's are very different, then the T-L fits on different samples cannot be compared because the fits will have been performed over different regions of k-space.

In addition to fits with the correct backscattering models, fits using other backscattering elements were performed on the spectra to

develop and verify[9,15] criteria for ligand elemental identification. The criteria are described in Appendix D.

A. Single Shell Distance Results

The distance results from single shell EXAFS fits for many manganese compounds are presented in Table 3. The distance results for the arsenic fluoride compounds studied which have known ligand distances are presented in Table 4. The distance differences between the crystallographic or electron diffraction distances and the EXAFS results are presented in Table 5. Table 5 also includes an indication of whether or not the "true" distance is within the estimated error obtained from the R vs. E_0 fitting matrix (see Figure 12).

A scan of the compounds listed in Tables 3, 4, and 5 indicates that many different types of compounds have been examined, ranging from the "ionic" compound α-MnS to the highly covalent pi bonding compounds $Mn_2(CO)_{10}$ and $K_3Mn(CN)_6$. This diversity was intential, in order to test the universality of these fitting models as well as the EXAFS technique itself.

Before comparing the results of the two models, some comments need to be made on the compounds which were selected for the H-D references. The choices for the carbon, nitrogen, and sulfur reference compounds were easy. For carbon, $K_3Mn(CN)_6$ did not have a normal low atomic number EXAFS amplitude, so $Mn_2(CO)_{10}$ was the only possible choice. For nitrogen, chloro-$\alpha,\beta,\gamma,\delta$-tetraphenyl porphinato (pyridine) manganese (III) (in the tables, MnTPPCl) was the only compound studied which had first coordination sphere nitrogen ligands. For sulfur,

both compounds seemed well behaved, so the covalently linked compound was chosen in case there was any chemical effect present in the EXAFS.

The choices for oxygen and manganese were not as easy to make due to the large selection of compounds. For oxygen, Tris(acetylacetonate) manganese (III) (in the tables, $Mn(AcAc)_3$) was chosen because it is one of the few Mn(III) compounds present in a collection which contains predominantly Mn(II) and Mn(IV) species. For manganese, di-μ-oxo-tetrakis (2,2'-bipyridine) dimanganese (III, IV) (in the tables, Mn(3,4)Bipy) was selected due to its importance in another study.[31] Unfortunately, after the majority of the fits had been performed using these two samples as references, it became obvious that while the amplitude functions seemed reasonable, the H-D distances were significantly different from the T-L distances. The differences were all in the same direction, which immediately implied problems with the reference samples. It was decided to use adjusted distance corrections (corrected a_{1i} in the H-D model. See Table 2). In the case of oxygen the value of a_{1i} was selected to yield a distance of 1.935 Å instead of 1.987 Å, the average distances of the four closest oxygen atoms and of the six closest oxygen atoms, respectively. For manganese, a_{1i} was adjusted to yield the correct distance for Mn_4N, the only model compound studied which has Mn in the "first" coordination sphere. As will be shown later, these corrections seem to be quite reasonable.

i. H-D and T-L Distance Results With "Full" Fits

Since the H-D fits are both phase and amplitude fits, the H-D results will be compared to the equivalent results for the T-L model

(third and fourth columns in Tables 3 and 4, and columns two and three in Table 5).

Scanning down the columns of Table 5 it is obvious that with the exception of a few compounds, the two models predict the same distances within a couple of hundredths of an angstrom. Of the compounds listed, each model was closest to the "true distance" seven times for first coordination sphere ligands. For second coordination sphere ligands, primarily carbon and manganese, the T-L model was closer on six of nine distances. For the three compounds where the H-D and T-L results differed greatly, the H-D model was the one that performed poorly. However, the discrepancies can be explained. For $KMnO_4$, the H-D model had two problems. First, the fixed value for E_o of 6565 eV is much too low for a Mn(VII) as evidenced by the T-L fitting value of 6588.6 eV. This E_o difference is sufficiently large to cause a distance error of 0.2 Å and to result in a best fit with a negative amplitude (180° phase error). Thus, the H-D model has problems when significantly different oxidation states are encountered. The second problem with $KMnO_4$ is the same problem also encountered with the other two poorly fit samples, the carbon ligands in bis(acetylacetonato) manganese(II) dihydrate (in the tables, $Mn(II)(AcAc)_2 \cdot 2H_2O$) and the manganese ligands in α-MnS. In all three samples the model amplitude function did not fit the EXAFS amplitude very well, so the phase result was distorted to compensate for the poor amplitude match. In T-L fits, σ_i permits change in the model's amplitude shape, so that the phase fit did not need to compensate as in the H-D model fits. The EXAFS amplitude mismatch is discussed in detail later.

After accounting for the three big distance differences, it must be concluded that the distance results for the two models are essentially equivalent.

ii. T-L Distance Results With "Phase Only" Fits

The rightmost columns of results in Tables 3 to 5 contain the T-L fitting results for distance determinations. Examination shows that phase only fits are equally likely to yield better distance results as poorer results. However, in the cases where R_i changes by at least 0.01 Å, then the phase only fits resulted in better distances (for example, see carbon distance in $K_3Mn(CN)_6$ and manganese distance in α-MnS). In the cases where large R_i changes occurred the model amplitude shape forced a compromise between fitting the phase properly and being able to fit the EXAFS amplitude. Performing a phase-only fit removed this restriction.

In one set of compounds, the arsenic fluorides, the phase-only fitting results were spectacular (see Table 4). If extremely long As-F distances are excluded from the "true" average distance calculations, then the distance results have errors of less than 0.005Å.[14,39] Six other AsF_6^- compounds have also been studied (not presented) in which the diffraction distances have never been determined. All of the EXAFS fitting distances are within 0.005 Å of the distances presented in Table 4.[14,39] This is compatible with the powder diffraction determinations which were used to estimate the ligand distances.[14,39] Therefore, in at least one case, excellent average distance measurements were obtained from the phase-only T-L fits.

iii. Curve Fitting Results In Predicting The Number of Ligands

Presented in Table 6 are the determinations of the number of backscattering ligand atoms in a transform peak, obtained from the curve fitting results (i.e., determination of N_i). For the H-D model almost all of the numbers fell between $N_i/2$ and N_i+2, with many of the results between N_i-1 and N_i+1. The values that are obtained for N_i are highly dependent on the choice of the model compounds. However, this range is compatible with the results obtained by others using the H-D method.[9,10,15,18] So the reference compounds selected seem to be reasonable.

For the T-L model the values obtained for N_i are consistently low, in most cases by a factor of two or greater. Ligands subject to the "focusing" effect mentioned earlier (ex. Mn in α-MnS) have been excluded from consideration. In the Teo-Lee model paper[27] it was stated that in order to obtain good agreement with some experimental data they examined, they arbitrarily increased the theoretical amplitudes by a factor of 2. The low results for N_i in Table 6 appear to argue that this arbitrary increase was a mistake.

While performing the T-L fits it became obvious that N_i and σ_i are highly correlated and some correction factor for this correlation is needed.

The values obtained for σ exhibit a broad range; from -0.04 to unphysical positive values as high as +0.01. If the value of σ was just dependent on vibrational effects, then σ should have a value close to -0.005.[5] Therefore, σ is being used to adjust the model's backscattering shape to obtain a better match with the observed EXAFS

amplitude. For example, consider $KMnO_4$, where the EXAFS amplitude does not fall off as fast as the T-L model predicts. The fitting process compensates for this by using a positive σ. A positive σ decreases the model's amplitude at low values of k and increases the model's amplitude at high k values relative to the midpoint of the fit (see Figure 9). In fact, with a value of σ equal to +0.01, the total oxygen model amplitude (see Figure 9) is almost flat when multiplied by k^3 the fitting weight function. This is exactly the behavior of the EXAFS amplitude of $KMnO_4$ when plotted as $k^3\chi(k)$.

As a result of multiplying $|f_i(k,\pi)|$ by an increasing positive function instead of the normally expected decreasing function, the fitting routine compensates by decreasing the value of N_i. In an attempt to account for this effect, several of the multiplication factors needed to obtain the correct number of atoms were calculated and plotted as a function of σ. The points used in the plots are displayed in Figure 13 and listed in Table 7. Many of the oxygen containing compounds and all of the arsenic fluoride compounds were excluded in order to test the correction factors. The surprising result was the presence of a linear relationship for a large number of the correction factors for both the low atomic number elements and Mn (see Figure 13). Straight line fits were made through the points which obviously exhibited a linear correlation. The linear fits are included in Table 7. It should be noted that the single Mn correction factor was needed for another study.[31] Consequently, the same slope as for the multiple Mn was used and a new intercept value was calculated.

The linear fits were used to correct the values of N_i obtained from the T-L model. The corrected values of N_i are listed in Table 6. Examining Table 6 one observes mixed results. For the non-oxygen samples, including the arsenic fluoride compounds, the correction was reasonably good. The oxygen values for N_i were improved, but are still too small by a factor of about two to three for those samples which were not used to obtain the line. Thus, the general conclusion must be that, while the correction helps, there are still other effects which must be taken into account when using EXAFS to predict the number of ligands.

VIII. Multishell Curve Fitting Results

There are two different types of multishell curve fits that can be done. The first type is to fit an entire EXAFS spectrum with one model shell per Fourier transform peak. The second type is to use more than one shell to fit a single nonseparable transform peak.

A. Multishell-Multipeak Fits

When the entire EXAFS spectrum is fit using the results of the single shell fits, generally the same results as the single shell fits are obtained. However, in some cases where the amplitude models did not fit well there can often be a dramatic improvement in the fit since one shell often complements the other by compensating for part of the amplitude mismatch of the other shell. While this often may improve the distance result, usually the number of atoms prediction gets worse.

As a general rule, the single shell results are, at least, as reliable and the problem of cross interaction between the shells is avoided.

B. Multishell-Single Peak Fits

There are two types of multishell fits on single transform peaks, one where there is some indication of the presence of at least one other shell, and one where there is no indication of additional distances or where more fitting shells are being used than the indications would imply.

There are three main indications of the presence of more than one distance in a transform peak. The most common indication is the presence of additional unresolved peaks or large shoulders on the side of a transform peak. For backscattering elements lighter than about Kr, the presence of the extra peaks or shoulders is certain to indicate multiple constituents in the transform peak. For backscatters heavier than Kr the amplitude and phase functions begin to exhibit significant structures which can produce unusually shaped Fourier transforms.[27] Thus, when working with heavier elements care must be taken before assuming that multipeaked Fourier transforms indicate the presence of more than one backscattering species or distance. The other two indications usually appear together. One is the appearance of an unusually broad Fourier transform peak (greater than 1 Å). This could indicate the presence of many different distances clustered about a common average distance (see for example, RbN_3 in Chapter 5, Reference 14). Usually, when this condition is present, the last of

the indications is also present; that is, amplitude beats in the EXAFS spectrum of that transform peak. Whenever there are EXAFS beats, there must be more than one basic distance in the Fourier transform, however, the beat may be present due to other physical reasons. The most likely other source of the beats is the previously mentioned "focusing" effect.[38] A concrete example of this phenomena is the manganese backscattering shell of α-MnS, which has a beat in its EXAFS amplitude, but no structural dispersion in the ligand distances. Luckily, however, the appearance of the "focusing" effect is also accompanied by phase disruptions as well, and in general, should be identifiable.

When there is evidence of more than one distance, then additional fitting shells should be used in the fit, but in practice no more than two shells should be used without the presence of three or more distinct features in the transform peak.

The reason for the fitting shell limitation is the same one as the reason why two shells should not be used on a single transform peak. Unless the model amplitudes and phases match the real EXAFS amplitudes and phases well, the multishell fit's individual shells interact too strongly and the result is generally nonsense. As examples, consider the fits presented in Tables 8 and 9, which are two of the best results obtained. In Table 8, the single and double shell fits on the Mn-O peak of α-MnO_2 are presented. From Table 3 it can be seen that the single shell Mn fits are compatible with all the rest of the single shell Mn fits with this same basic type of structure, although the results in this case may be affected by the oxygen

contribution to the peak. It can be seen immediately in Table 8 that the good single shell Mn fit is dramatically improved by using an additional shell. However, with both models the resulting two shell fits are nonsense. In the case of the H-D model the positive amplitude result (number 1) has a distance separation which is sufficiently large to appear in the transform as well as being +0.2 Å in error. The second trial (number 2) resulted in a closer distance, however, the amplitude is negative indicating that it is the wrong element or the "focusing" effect is involved. Neither of these statements is true. In the case of the T-L fits while an excellent fit was obtained, there were three things wrong with the fit. First, the distance result for they oxygen shell was 0.1 Å too long. Second, the E_o for Mn is too high for it to be a Mn atom (see Table 3 and Appendix D). Third, the σ_i's for both shells are much too large, indicating that strong shell interaction was occurring. Thus, this fit is not believable and did not work.

Now consider Table 9, the As_2O_3 T-L model fits. The H-D model fits were not included because no arsenic model parameters were available. The distance results are excellent and the number of atoms predicted are compatible with the previously observed results. However, this fit is not believable. First, the E_{oi} value for the oxygen shell of the second peak is 50 eV too high. If the difference between the two oxygen E_{oi}'s had been as large as 10 eV then this result would have been acceptable. (Note: a + 50 eV change in E_{oi} corresponds to approximately a +0.1 Å change in R_i when fitting.) Second, the value for σ_i for arsenic is unusually high for a heavy atom (see Table 6),

but coupled with the disastrously large value of σ_i for oxygen, it was obvious that here the shell models were strongly interacting as in Table 8. For these reasons the fit results of Table 9 would not have been believed if they had been performed on an unknown compound's transform peak.

The general conclusion that must be drawn from the many multishell fits performed during this study using both models is that unless there is strong evidence of the presence of an additional shell, multishell fits in general will not be believable unless it can be demonstrated on a similar known compound that the multishell fits work in that particular system. If there is evidence that multidistance backscatterers are present, it is recommended that synthetic sample EXAFS spectra, created using one of the models, would be a much better starting point in analyzing a new sample than the multishell fits. After working with synthetic spectra and gaining experience with the behavior of the transforms and the simpler fits, then multishell fits should be attempted, but failure of the multishell fitting approach should be expected.

IX. Discussion and Conclusions

The primary goals of this study when it was begun, were to compare the two main k-space EXAFS fitting models and to determine the limitation of the EXAFS technique. As to the first goal, the results presented earlier show that fitting single shells to individual transform peaks results in essentially equivalent results using either of the models. However, the general conclusion that must be drawn is

that the Teo-Lee model is the preferable one to use on the basis of its versatility. By fixing E_o and σ_i for a given element fitting model, the Teo-Lee model reduces to the Hodgson-Doniach model in operation. However, the additional parameters allow the user to handle unusual cases, such as $KMnO_4$, and to perform disorder studies, if so desired. Thus, it is recommended that EXAFS users develop the capability to utilize the Teo-Lee model.

The most serious question concerned with the limitations of the EXAFS technique was whether the EXAFS spectra are chemically sensitive. The elements most likely to exhibit chemical sensitivity are the light elements so as many samples as possible were selected which contained light elements. The EXAFS results in Table 6 show that the backscattering amplitudes are definitely chemically sensitive, as evidenced by the large variation in σ_i. The question of whether the EXAFS phase also exhibits extensive chemical sensitivity is a more complex question. Looking at the results of Tables 3 to 5, the answer would immediately be yes, but before this conclusion is reached an important effect must first be considered. In a paper published by Eisenberger and Brown[40] on disordered systems, they noted that in many cases the observed EXAFS distances are shorter than expected, often by the non-appearance of exceedingly long ligand distances in a coordination sphere. If this phenomena is a common one, then the reference distances used to compute the distance errors in Table 5 could be wrong. The distances that would be changed are listed in Table 10. Comparison of Tables 5, 6 and 10 shows that for the cases of $Mn_2P_2O_7$ and Mn(II) $AcAc_2 \cdot 2H_2O$, there is some kind of averaging process going on,

but the exact weighting function to use may be open for debate. For the other four oxygen samples and most definitely for the two arsenic samples, the dramatic improvement in the EXAFS results indicate that certain ligands seem to contribute little to the EXAFS spectrum. Thus, it seems clear that some form of distortion induced invisibility is present in some EXAFS compounds.

By taking distortion effects into account all of the bad distance errors not previously accounted for have now been reduced to the point where the expected EXAFS error range is reduced to approximately ± 0.03 Å. But it still does not account for the unusual effect observed for manganese distances (see Tables 3 and 5). Manganese is a sufficiently heavy element that chemically induced EXAFS phase changes would not be expected. When the Mn is in the first coordination sphere (Mn_4N) then the distance result is very good. It is also quite good when in the second coordination sphere except when a very special configuration is observed. When the Mn atoms are bridged through two oxygen atoms (di-μ-oxo bridged) then the T-L results are between 0.03 Å and 0.04 Å short. This short distance result occurs on all of the two oxygen bridged Mn structures that were studied (see also Reference 31); therefore, it cannot be a random distance error, but a systematic one. Apparently, the presence of the two oxygen atoms' potentials create a different phase shift than the simple model used in the theoretical calculations. A likely candidate for the cause of this discrepancy is a violation of the muffin-tin potential assumption.[27] In any case, this effect needs to be explored theoretically in order to be understood.

The only conclusion that can be drawn as result of this study is that the EXAFS technique is chemically sensitive. Therefore, in order to utilize this technique successfully, it is necessary to perform a complete analysis on a model compound or model system which physically and chemically resembles the system to be studied so possible deviations can be detected and compensated for.

It is also obvious that a great deal of work needs to be done on the analysis methodology before multishell fits can be used as a general analysis tool.

Appendix A.

Adding Scans Which Contain Level Shifts

Occasionally, data scans exhibit sudden signal level shifts which exceed the linear range of the detectors. These level shifts result in level shifts in the detected cross sections. These level shifts terminated the useable portion of the data scan.

To recover the good, lower energy part of the scan, special programs were developed to add this type of data. The co-added scan was split into at least two regions; one which has the truncated scan(s), and one without. Each region of the co-added scan had its own specific weighting which reflected the total data collection time for each point in that region. When all of the desired scans were co-added, the final scan was produced using the weightings. Data processing then proceeded normally.

Some co-added scans exhibited discontinuities at the add region boundaries. This was due to a different background function in the truncated scan(s) than was exhibited in the other co-added files. To remove this problem an option in the program adjusted the slope and intercept of the truncated file to match the slope of the previously co-added scans, thereby eliminating the discontinuity.

Appendix B.

Adding Energy Shifted Scans

It is quite common to observe data scans which exhibit slight energy shifts from one scan to another. These shifts at SSRL were due to changes in the storage ring operating conditions and mechanical problems with the crystal goniometer. Special programs were developed to handle this problem.

Energy shifts are detected and calibrated by examining numerical derivatives (using polynomial fits) of the K-edge and its features. One scan is selected as the reference standard and all the shifts relative to this standard are determined. All glitches, including "crystal glitches" are removed from the scans to be added to prevent contamination of additional data points by the shifting process. The point substitution method described in Section IV.A was used. All of the scans to be co-added are shifted by the required amount. The scans are returned to the same crystal angle or X-ray energy as the reference scan by linear interpolation. The shifted scans are then co-added. The bad point(s) at the end(s) of the co-added scan, resulting from the shift(s), is(are) deleted. Processing then continues normally.

Appendix C.

Fluorescent Data Preparation

The fluorescent data collection technique monitors the X-ray absorption cross section by measuring the X-ray fluorescence produced by the absorption phenomena. What follows is a brief description of the initial data processing used for fluorescent data (equivalent to Section IV. A.).

The equation describing fluorescent detection reduces directly to $\mu(E)$ when the sample is dilute in the element of interest.[6] Therefore, the natural logarithm step used in absorption analysis is not used with fluorescent data.

Any obvious glitches are fixed as before. If the scan contains too many glitches or a level shift is seen, the scan is discarded. Edge derivatives are taken and any energy shifting that may be necessary is performed. Only scans from a particular data collection channel are co-added at this point.

The pre-edge background does not exhibit a Victoreen behaviour, so the pre-edge removal techniques described in the main text usually do not work. It is very difficult to obtain a reasonable fit which can be extrapolated over the entire scan without exhibiting significant curvature. Thus, no pre-edge background removal is normally done. Instead, the lowest points just before the edge onset are adjusted to zero. A low order post-edge polynomial fit is used to scale the edge jump to a value of one as before. This polynomial is extrapolated

over the entire scan and subtracted from the data in an attempt to remove the bulk of the post-edge background. Unity is then added to the data scan to obtain a normalized cross section for each individual data channel. The individual $\mu_j^*(E)$'s should now have small residual backgrounds, so the individual $\mu_j^*(E)$'s are added and again normalized to unity to obtain the final normalized cross section spectrum, $\mu_j^*(E)$. Data processing then continues normally.

Appendix D.

Ligand Element Identification

It is not possible to make absolute element identifications from EXAFS analysis when the ligands have similar atomic number or are unknown. However, it is possible to make estimates of ligand identity using the approach described below, especially if the basic elemental composition of the sample is known.

For the purpose of this discussion, two elements are considered different if their atomic numbers differ by at least 5; i.e., carbon, nitrogen, oxygen, and fluorine are considered the same while oxygen vs sulfur, oxygen vs manganese, and oxygen vs arsenic, are different elements.

The first step is to make a good estimate of the first coordination sphere ligand. This is done by utilizing the first ligand's estimated distance obtained from the Fourier transforms, the estimated formal oxidation state of the absorbing atom obtained from the K-edge position (reference 41 and Chapter V) and the known chemistry of the absorbing species. This usually yields a good guess. In addition, if the elemental composition of the sample is known, then the ligand can usually be identified.

The second step is to examine the behavior of the Fourier transform peak heights in $|\phi_n(R)|$ (equation 5) as a function of n. In no sample analyzed in this laboratory, including a number of additional manganese and molybdenum compounds not included here, has the ratio of

a lighter ligand's peak height and a heavier ligand's peak height increased as n is increased. This statement excludes transform peaks which are obviously affected by interference, either by another nearby peak or by an excess noise level.[31] This statement does not exclude peaks which are affected by the "focusing effect".[3] In those cases, the expected decrease in the ratio due to the ligand's atomic number difference is not realized (see for example α-MnS in Table 1). The predominant reason for this behavior is displayed graphically in Figure 9. Heavier elements have enhanced backscattering capability at higher k-values, so the k^n multiplication in $\phi_n(R)$ preferentially enhances the heavier element's transform peaks. Using the ratio information, the estimated ligand distances and the sample composition, if known, good starting guesses for the identity of the other ligands can be made.

The final step is to test these guesses using the curve fitting models. Table 11 contains examples of curve fits using different element guesses on the same Fourier filtered k-space spectra. The identification method used with the Hodgson-Doniach model,[15] was developed by Hodgson and co-workers.[9,10,15] The two basic criteria are a positive fitting amplitude and the best fitting error. For illustration consider the sulfur ligands in α-MnS (Table 11). The first and second criteria predict sulfur, which is correct. A note of caution must be added with these criteria. The first criterion will usually not be valid when a ligand is subjected to the focussing effect. So care must be exercized when examining higher order shells. The second criterion occasionally will also not be satisfied in the case of poor fits by all

the element guesses. In this case, the proper element's model does not fit the EXAFS amplitude well, so the resulting fit is a compromise between the amplitude and phase parts. When this happens it is often possible for a heavier element's model to fit the high k region of the spectrum well and the lower k region poorly, but the fitting value will be better than the fit for the correct element. This case is identified by visually inspecting the resulting fits.

When using the Teo-Lee model,[27] additional criteria must be used due to the larger number of fitting parameters. One criterion is a reasonable value for E_0. Examining Table 3 it can be seen that each element has a region in which E_0 should fall. For example, E_0 for carbon, nitrogen, and oxygen ligands in manganese compounds is expected to be greater than 6560 eV and near 6570 eV; E_0 for manganese ligands in manganese compounds is expected to be near 6550 eV. Any model whose E_0 was significantly outside its expected range normally would be rejected. This last additional criterion is the expectation that σ should be between -0.005 $\mathring{A}^2$ and -0.10 $\mathring{A}^2$. As discussed in the main text, this is not always true, but if positive or large negative values are observed, then that choice of element must be examined closely.

For example, consider the two sets of ligand fits presented in Table 11. For the manganese ligand in Mn(3,4)Bipy, all of the criteria point to manganese as the correct element. Only Mn has an E_0 which is really close to the desired values, but the observed differences for the other models are not sufficient to exclude them absolutely.

The negative amplitude criterion excludes sulfur since its amplitude is negative. The σ criterion strongly suggests Mn and when coupled with the excellent Mn model fit, excludes nitrogen and oxygen as ligands. For the oxygen ligand in $Mn_2P_2O_7$, the results suggest nitrogen or oxygen as the ligand. Sulfur is excluded by both the negative amplitude and the high E_0. Mn is excluded by its large negative and then a visual inspection which showed an excellent high k fit but a poor low k fit, the condition described earlier which often yields good numerical fits, but poor overall fits. As illustrated in Table 11, it is not possible to distinguish between nearby elements, so either nitrogen or oxygen could be the correct choice.

Table 1. Examples of Fourier Transform Power Spectrum Peaks, Relative Magnitudes and Position

E_0 = 6565eV, Transform Range 3. to 13. $\mathring{A}^{-1}$, Kaiser = 3 window

Shell (no. of atoms)		$k^0\chi(k)$	$k^1\chi(k)$	$k^2\chi(k)$	$k^3\chi(k)$
α-MnO_2					
Oxygen	(6)	1.00	1.00	1.00	1.00
Manganese	(4)[b]	.57	.58	.55	.51
Oxygen-Manganese	(6-4)	.62	.88	1.13	1.37
α-MnS					
Sulfur	(6)	.62	.58	.52	.47
Manganese	(6)[c]	.44	.45	.40	.34
Mn(3,4)Bipy[a]					
Oxygen	(2)	.61	.67	.72	.76
Manganese	(1)	--[d]	.42	.53	.62

Table 1 (continued)

(b) Peak Positions and Distance Offsets (Å)

	$k^0\chi(k)$		$k^1\chi(k)$		$k^2\chi(k)$		$k^3\chi(k)$	
Shell	Position	Offset	Position	Offset	Position	Offset	Position	Offset
α-MnO_2								
Oxygen (1.89 A)	1.38	.51	1.44	.45	1.49	.40	1.51	.37
Manganese (2.87 A)	2.40	.47	2.41	.46	2.40	.47	2.40	.47
Oxygen-Manganese (3.44 A)	2.92	.52	2.95	.49	2.97	.47	2.99	.45
α-MnS								
Sulfur (2.61 A)	1.92	.69	1.97	.64	2.01	.60	2.05	.56
Manganese[c] (3.69 A)	2.96	.73	2.99	.70	3.08	.61	3.14	.55

Table 1 (continued) (b) Peak Positions and Distance Offsets (Å)

Shell	$k^0\chi(k)$ Position	$k^0\chi(k)$ Offset	$k^1\chi(k)$ Position	$k^1\chi(k)$ Offset	$k^2\chi(k)$ Position	$k^2\chi(k)$ Offset	$k^3\chi(k)$ Position	$k^3\chi(k)$ Offset
Mn(3,4)Bipy[a]								
Oxygen[b] (1.82 A)	1.06	.76	1.15	.67	1.30	.52	1.37	.45
Manganese (2.72 A)	--[d]	--	2.16	.56	2.24	.48	2.26	.46

[a] Mn(3,4)Bipy = di-μ-oxo-tetrakis (2,2'-bipyridine)dimanganese (III,IV)

[b] Peak is contaminated by interference from nearby peak(s) and has significant static disorder.

[c] Directly behind sulfur first shell and therefore subject to "focussing" effect. See P. A. Lee and J. B. Pendry, Phys. Rev. B., 11 (1975) 2795 (Reference 3).

[d] Peak is not observable due to noise.

Table 2. Hodgson-Doniach (H-D) Fitting Parameters

Absorber	Scatterer	Ref Compound[a]	Fit Error[b] ($\times 10^4$)	A	σ	β	a_0	a_1	a_2
Mn	C	$Mn_2(CO)_{10}$	8.7	0.0267	.0442	-.888	2.9990	-.507	11.12
Mn	N	MnTPPC1[e]	2.5	0.3182	.0368	.807	-.3639	-.797	8.49
Mn	O	$Mn(III)AcAc_3$	0.17	1.2595	.0080	2.66	.0626	-.801[c]	7.11
Mn	S	$Mn(II)(SC_6H_5)_4^{-2}$	4.3	0.1078	.0319	.0524	1.4092	-.664	17.01
Mn	Mn	Mn(3,4)Bipy	0.06	0.1506	.0209	.0872	-1.4424	-.629[d]	11.73
As	F	AsF_3	6.2	0.1179	.0105	1.01	.0876	-.554	26.04

EXAFS parameters: Mn E_0 = 6565eV k = 4-12$\mathring{A}^{-1}$

A E_0 = 11943eV k = 5.5-13.5$\mathring{A}^{-1}$

[a] MnTPPC1 ≡ Chloro-α,β,γ,δ-tetraphenylporphinato (pyridine) manganese (III)

$Mn(III)AcAc_3$ ≡ Tris (acetylacetonato) manganese (III)

$Mn(II)(SC_6H_5)_4^{-2}$ ≡ $[(C_6H_5)_4P]_2$ $[Mn(II)(SC_6H_5)_4]$

Mn(3,4)Bipy ≡ di-μ-oxo-tetrakis (2,2'bipyridine) dimanganese (III,IV)

Table 2. Hodgson-Doniach (H-D) Fitting Parameters, Continued

[b] Fit error = least square error per point with k^3 weighting.

[c] This parameter was adjusted to yield a distance of 1.935 $\mathring{A}$, the average of the four closest oxygen atoms. This parameter yields much better results for most other oxygen distances.

[d] This parameter was adjusted to yield the correct Mn distance for Mn_4N. Most other manganese fits yield better results with this value.

[e] Fit from k = 4 to 11$\mathring{A}^{-1}$ due to trace iron contamination in sample.

Table 3. Observed EXAFS distances in Manganese Compounds and Complexes from k = 4 to 12 $\mathring{A}^{-1}$ Fits

Compound	Average Distance($\mathring{A}$)[a]	H - D (E_0=6565eV)	T - L Distance w/amp	T - L E_0 +6500eV	T - L Distance w/o amp	T - L E_0 +6500eV
(a) IN FIRST COORDINATION SPHERE						
Carbon						
$Mn_2(CO)_{10}$	1.823	(ref)	1.877(105)	78.2	1.882(30)	81.0
$K_3Mn(CN)_6$	2.002	1.968	1.964 (44)	59.8	1.985(35)	66.5
Nitrogen						
MnTPPCl[b,h]	2.010	(ref)[f]	2.021 (38)	65.1	2.018(19)	64.9
Oxygen						
$Mn_2P_2O_7$	2.124	2.158	2.163 (48)	68.5	2.169(30)	69.0
Mn(II)AxAc$_2\cdot 2H_2O$[b]	2.179	2.160	2.152 (66)	63.0	2.175(42)	66.5
Mn(II)Oxalate$\cdot 2H_2O$[b]	2.120	2.197	2.177 (40)	63.0	2.184(24)	63.8
$MnCl_2\cdot 4H_2O$[f]	2.206	2.251	2.255 (36)	67.3	--[i]	--[i]
Mn(II)Acetate$_2\cdot 4H_2O$	(unk)[c]	2.175	2.158 (46)	63.1	2.168(19)	64.4

Table 3. Observed EXAFS distances in Manganese Compounds and Complexes from k=4 to 12$\mathring{A}^{-1}$ Fits, Continued

Compound	Average Distance($\mathring{A}$)[a]	H -D (E_0=6565eV)	T - L Distance w/amp	T - L E_0 +6500eV	T - L Distance w/o amp	T - L E_0 +6500eV
Mn_3O_4	2.073	1.934	1.921 (36)	64.6	1.930(28)	67.8
Mn_2O_3	2.019	1.930	1.936 (16)	71.0	1.938(16)	71.4
$Mn(III)AcAc_3$[b]	1.987	1.935[d]	1.910 (17)	60.0	1.915 (7)	61.4
Mn(3,4)Bipy[b]	1.819	1.790	1.814 (54)	75.0	1.812(19)	75.5
α-MnO_2	1.892	1.890	1.926 (32)	80.0	1.930(31)	81.7
$KMnO_4$	1.629	1.802[e]	1.665 (22)	88.6	1.671(13)	90.4
Sulfur						
α-MnS	2.612	2.601	2.601 (18)	57.9	2.595 (6)	57.3
$Mn(II)(SC_6H_5)_4^{-2}$[b]	2.442	(ref)	2.432 (20)	55.8	2.428 (8)	55.4
Manganese						
Mn_4N	2.729	(ref)[g]	2.732 (14)	50.2	2.732 (3)	50.1

Table 3. Observed EXAFS distances in Manganese Compounds and Complexes from k=4 to 12$\mathring{A}^{-1}$ Fits, continued

Compound	Average Distance(A)[2]	H - D (E_0=6565eV)	T - L Distance w/amp	T - L E_0 +6500eV	T - L Distance w/o amp	T - L E_0 +6500eV
(b) IN SECOND COORDINATION SPHERE						
Carbon						
Mn(II)$AcAc_2 \cdot 2H_2O$[b]	3.066	3.181	3.135 (56)	57.6	--[j]	--[j]
MnTPPCl[b]	3.030	3.075	3.073 (50)	62.3	--[j]	--[j]
Nitrogen						
$K_3Mn(CN)_6$	3.143[x]	3.137[y]	3.071 (20)[y]	53.1	3.086 (3)[y]	55.8
Manganese						
α-MnS	3.694[x]	3.539[x]	3.642 (52)	41.9	3.698(72)	46.8
Mn_3O_4	3.430	3.445	3.444 (46)	52.3	3.434(60)	50.5
Mn_2O_3	3.138	3.091[z]	3.101 (18)[z]	53.1	3.092(20)[z]	53.6
Mn(3,4)Bipy[b]	2.716	2.684[g,z]	2.683 (12)[z]	48.6	2.677(16)[z]	46.7
α-MnO_2(Mn)	2.870	2.860[z]	2.831 (46)[z]	45.5	2.832(15)[z]	46.5
α-MnO_2(Mn-O)	3.454[k]	3.417[k,z]	3.423 (13)[k,z]	53.6	3.420 (4)[k,z]	52.7

Table 3. Observed EXAFS Distances in Manganese Compounds and Complexes from k=4 to 12$\mathring{A}^{-1}$ Fits, cont'd.

---

[a] Average Crystallographic distances reported in the literature weighted by R^{-2}.

[b] MnTPPCl = Chloro-α,β,γ,δ-tetraphenyl porphinato(pyridine)manganese(III)

Mn(III)$AcAc_3$ = tris(acetylacetonato)manganese(III)

Mn(3,4)Bipy = di-μ-oxo-tetrakis(2,2'-bipyridine)dimanganese(III,IV)

$Mn(II)(SC_6H_5)_4^{-2}$ = $[(C_6H_5)_4P]_2$ $[Mn(II)(SC_6H_5)_4]$

[c] This structure is believed to be similar to the Ni(II) and Co(II) acetates·$4H_2O$ which both have average oxygen distances of 2.10$\mathring{A}$

[d] Reference distance for oxygen fits obtained by neglecting the two long oxygen distances caused by Jahn-Teller distortions.

[e] H-D model was unable to compensate for the large edge shift due to the Mn(VII) since E_0 is fixed at 6565eV.

[f] Distance is probably distorted by contribution due to chlorine ions whose backscattering contribution is missing.

[g] All parameters from Mn(3,4)Bipy except distance which is adjusted to yield correct Mn_4N distance.

[h] Fits from k = 4 to 11$\mathring{A}^{-1}$ due to trace iron contamination.

[i] Due to the suspected contamination of this shell with chlorine backscatter, only the basic fits were performed.

Table 3. Observed EXAFS Distances in Manganese Compounds and Complexes from k=4 to 12$\mathring{A}^{-1}$ Fits, cont'd.

j This peak was only a factor of 2-3 above the noise level so only the basic fits were performed.

k This shell also contains oxygens which could distort the distance result. The fit distances are very close (<.01A) to the average oxygen distance.

x Atoms in this shell are directly behind first shell ligands and thus are subject to a "focussing" effect. See Lee and Pendry (1975), reference 3.

y Negative amplitude. In H-D model this indicates that this is the wrong element.[15] Also, see note x above.

z Short distance by approximately 0.035$\mathring{A}$ seems to be characteristic of di-μ-oxo bridged manganese distances (distorted di-μ-oxo bridged in the case of α-MnO_2).

Table 4. Observed EXAFS Fluorine Distances in Arsenic Fluoride Compounds

Sample	Average Distance(Å)[a]	H - D (E_0=11943eV)	T - L Distance w/amp	T - L E_0 (+11800eV)	T - L Distance w/amp	T - L E_0 (+11800eV)
AsF_3	1.706	(ref)	1.709 (13)	86.	1.710 (7)	87.
AsF_5	1.678	1.670	1.678 (15)	88.	1.681 (4)	89.
$XeFAsF_6$	1.750[b]	1.703	1.727 (15)	91.	1.732(11)	93.
$Xe_2F_3AsF_6$	1.740[c]	1.719	1.739 (30)	93.	1.728(22)	90.

[a] Average crystallographic distance for $XeFAsF_6$ and $Xe_2F_3AsF_6$ and average electron diffraction distance for AsF_3 and AsF_5.

[b] If one long F distance is ignored (1.860Å), then average distance is 1.730Å.

[c] Has four distinct distances separated by over 0.1Å, however, if longest F distance is ignored (1.790Å), then average distance is 1.731Å.

Table 5. Distance Differences Between Diffraction Determined Distances and EXAFS Results (Diffraction - EXAFS)

Compound	Difference(Å)	T - L Differences w/amp(Å)	Within Error	w/o amp(Å)	Within Error
(a) IN FIRST COORDINATION SPHERE					
Carbon					
$Mn_2(CO)_{10}$	(ref)	-.054	Y	-.059	N
$K_3Mn(CN)_6$	.034	.038	Y	.017	Y
Nitrogen					
MnTPPCl[a]	(ref)	-.011	Y	-.008	Y
Oxygen					
$Mn_2P_2O_7$	-.034	-.039	Y	-.045	N
$Mn(II)AcAc_2 \cdot 2H_2O$[a]	.019	.027	Y	.004	Y
$Mn(II)Oxalate \cdot 2H_2O$	-.077	-.057	N	-.064	N
$MnCl_2 \cdot 4H_2O$[b]	-.045	-.049	N	--[a]	--[a]
Mn_3O_4	.139	.152	N	.143	N
Mn_2O_3	.089	.083	N	.081	N
$Mn(III)AcAc_3$[a,c]	.052[d]	.077	N	.072	N

Table 5. Distance Differences Between Diffraction Determined Distances and EXAFS Results (Diffraction - EXAFS) Continued.

Compound	H - D Difference(Å)	T - L Differences w/amp(Å)	Within Error	w/o amp(Å)	Within Error
Mn(3,4)Bipy	.029	.005	Y	.007	Y
α-MnO_2	.002	-.034	N	-.038	N
$KMnO_4$	-.172[e]	-.036	N	-.042	N
Fluorine					
AsF_3	(ref)	-.003	Y	-.004	Y
AsF_5	.008	0.	Y	-.003	Y
$XeFAsF_6$	.047	.023[g]	N[g]	.018[g]	N[g]
$Xe_2F_3AsF_6$	.021	.001	Y	.012	Y
Sulfur					
α-MnS	.011	.011	Y	.017	N
$Mn(II)(SC_6H_5)_4^{-2}$[a]	(ref)	.010	Y	.014	N
Manganese					
Mn_4N	(ref)	.003	Y	.003	Y

Table 5. Distance Differences Between Diffraction Determined Distances and EXAFS Results (Diffraction - EXAFS) Continued.

Compound	H - D Difference(Å)	T - L Differences w/amp(Å)	Within Error	T - L Differences w/o amp(Å)	Within Error
(b) IN SECOND COORDINATION SPHERE					
Carbon					
$Mn(II)AcAc_2 \cdot 2H_2O$[a]	-.115	-.069	N	--[a]	--[a]
MnTPPCl[a]	-.045	-.043	Y	--[a]	--[a]
Nitrogen					
$K_3Mn(CN)_6$	.006[x]	.072[x]	N	.057[x]	N
Manganese					
α-MnS	.155[x]	.052[x]	Y	.004[x]	Y
Mn_3O_4	-.015	-.014	Y	-.004	Y
Mn_2O_3	.047[z]	.037[z]	N	.046[z]	N
Mn(3,4)Bipy[a]	.032[z]	.033[z]	N	.039[z]	N
α-MnO_2(Mn)	.010[z]	.039[z]	Y	.038[z]	N
α-MnO_2(MnO)	.037[f,z]	.031[f,z]	N	.034[f,z]	N

Table 5. Distance Differences Between Diffraction Determined Distances and EXAFS Results (Diffraction - EXAFS) Continued

[a] See Table 3.

[b] Believe oxygen shell is contaminated with some chlorine backscatter.

[c] H-D reference. Distance adjusted to 1.935Å, the average distance for the four closest oxygens.

[d] Reference distance for oxygen fits. Obtained by neglecting the two long oxygen distances caused by Jahn-Teller distortions.

[e] H-D model was unable to compensate for the large edge shift due to the Mn(VII) since E_0 is fixed at 6565eV.

[f] This peak contains oxygen contamination. See note k, Table 3.

[g] If long As-F is dropped, errors are (+.003, Y) and (-.002, Y) respectively.

[h] If long As-F is dropped, errors are (+.008, Y) and (-.003, Y) respectively.

[x] Atoms are subject to a "focussing" effect (see note x of Table 3). Best fit had negative amplitude indicating 180° phase shift (see note Y of Table 3).

[z] Short distance by at least 0.03Å seems to be characteristic of di-μ-oxo bridge manganese distances (and distorted di-μ-oxo bridged in α-MnO_2 case).

Table 6. Predicted Number of Atoms in a Shell Using EXAFS (Fits from k = 4 to 12$\mathring{A}^{-1}$)

Compound	No. of Atoms	Hodgson-Doniach	Teo - Lee		
			Fit	σ	Corrected[a]
(a) FIRST COORDINATION SPHERE					
Carbon					
$Mn_2(CO)_{10}$	5	(ref)	4.4	-.0066	6.0
$K_3Mn(CN)_6$	6	2.9	1.5	+.00525	5.9
Nitrogen					
MnTPPCl[b]	4	(ref)	3.0	-.0130	3.0[y]
Oxygen					
$Mn_2P_2O_7$	6	4.0	1.1	-.0066	1.5
$Mn(II)AcAc_2 \cdot 2H_2O$	6	5.3	1.7	-.0129	1.7[y]
$Mn(II)Oxalate \cdot 2H_2O$	6	11.3	2.8	-.0075	3.2
$MnCl_2 \cdot 4H_2O$	4[f]	5.8	2.1	-.0172	2.1[y]
$Mn(II)Acetate_2 \cdot 4H_2O$	6[c]	4.3	1.4	-.0131	1.4[y]
Mn_3O_4	5.33	5.9	0.8	+.0021	2.6
Mn_2O_3	6	4.4	0.7	+.00005	1.9

Table 6. Predicted Number of Atoms in a Shell Using EXAFS (Fits from k = 4 to 12$\mathring{A}^{-1}$) Continued.

Compound	No. of Atoms	Hodgson-Doniach	Teo - Lee		
			Fit	σ	Corrected[a]
$Mn(III)AcAc_3$[b]	6	(ref)	0.9	-.00558	1.4
Mn(3,4)Bipy[b]	2	5.1	1.0	-.0051	1.8
α-MnO_2	6	6.4	1.1	-.00023	2.4
$KMnO_4$	4	-13.0	0.8	+.0095	4.0
Fluorine					
AsF_3	3	(ref)	1.1	-.0007	2.9[g]
AsF_5	5	4.8	1.6	-.0003	4.4[g]
$CsAsF_6$	6	5.0	1.9	-.0014	4.8[g]
$NaAsF_6$	6	4.1	1.5	-.0012	3.9[g]
$XeFAsF_6$	6	3.7	1.8	-.00156	4.4[g]
$Xe_2F_3AsF_6$	6	3.3	2.3	-.00524	3.8[g]
Sulfur					
α-MnS	6	1.9	1.1	-.0123	2.5[h]
$Mn(II)(SC_6H_5)_4^{-2}$	4	(ref)	2.0	-.00965	5.1[h]

Table 6. Predicted Number of Atoms in a Shell Using EXAFS (Fits from k = 4 to 12$\mathring{A}^{-1}$) Continued.

Compound	No. of Atoms	Hodgson-Doniach	Teo - Lee		
			Fit	σ	Corrected[a]
Manganese					
Mn_4N	6	2.3	3.4	-.0165	7.4
(b) SECOND COORDINATION SPHERE					
Carbon					
Mn(II)AcAc·$2H_2O$[b]	4	1.7	2.3	-.0079	2.5
MnTPPCl[b]	8	3.7	2.5	+.00217	8.1
Nitrogen					
$K_3Mn(CN)_6$	6[x]	-8.6	-4.3	+.00037	-12.4
Manganese					
α-MnS	6[x]	-0.9	6.2	-.0397	5.5
Mn_3O_4	4[e]	2.9	1.2	+.00006	3.8
Mn_2O_3	6	2.1	3.4	-.0180	7.2
Mn(3,4)Bipy[b]	1	(ref)	0.8	-.00679	0.9

Table 6. Predicted Number of Atoms in a Shell Using EXAFS (Fits from k = 4 to 12$\mathring{A}^{-1}$) Continued.

Compound	No. of Atoms	Hodgson-Doniach	Teo - Lee Fit	Teo - Lee σ	Teo - Lee Corrected[a]
α-MnO_2(Mn)	4	0.7	0.6	-.00785	1.6
α-MnO_2(Mn-O)	4[d]	3.3	1.3	+.00075	4.1

---

a See text, Table 7 and Figure 14.

b MnTPPCl = Chloro-α,β,γ,δ-tetraphenylporphinato(pyridine)manganese(III)

Mn(III)$AcAc_3$ = tris(acetylacetonato)manganese(III)

Mn(3,4)Bipy = di-μ-oxo-tetrakis(2,2'-bipyridine)dimanganese(III,IV)

Mn(II)$AcAc_2 \cdot 2H_2O$ = bis(acetylacetonato)manganese(II)dihydrate

$Mn(II)(SC_6H_5)_4^{-2} = [(C_6H_5)_4P]_2[Mn(II)(SC_6H_5)_4]$

c This structure is believed to be similar to the Ni(II) and Co(II) acetate tetrahydrates which are six coordinate in oxygen.

d Contaminated with oxygen atoms.

e Mn(II) has 8 Mn(III) neighbors; the two Mn(III)'s have 2 Mn(II) neighbors

f Peak seems to be contaminated with some presence of Cl atoms

g Used CNO correction factors

Table 6. Predicted Number of Atoms in a Shell Using EXAFS (Fits from k = 4 to 12$\mathring{A}^{-1}$) Continued.

[h] Used multiple Mn correction factors

[x] Second shell atom is linearly behind first shell and thus subject to "focussing" effects. See Lee and Pendry (1975), reference 3.

[y] $|\sigma|$ is too large for amplitude correction.

Table 7. Least Square Linear Fits Calculated to Correct Teo-Lee Fits for Number of Atoms in a Shell (See Figure 14).

(a) CNO[a] CORRECTION

Shell		Sample[e]	σ[b]	Correction Factor Needed
Carbon	(A)	$K_3Mn(CN)_6$	+.0053	3.97
	(B)	$Mn_2(CO)_{10}$	-.0066	1.14
	(D)	MnTPPCl[c]	+.0022	3.21
Nitrogen	(C)	MnTPPCl[c]	-.0130	1.33[d]
Oxygen	(1)	Mn_2O_3	+.00005	8.96[d]
	(2)	$KMnO_4$	+.0095	4.82
	(3)	α-MnO_2	-.0002	5.71[d]
	(4)	Mn(3,4)Bipy[c]	-.0051	1.92
	(5)	Mn(4,4)Phen[c]	-.0010	2.70
	(6)	Mn(3,4)Phen[c]	-.0057	1.55
	(7)	Mn_3O_4	+.0021	4.94[d]

Fitting result (standard deviations in parentheses):

$$\text{Scale Factor}_{CNO} = 216.1\ (96)\ \sigma + 2.796\ (51)$$

Table 7. Least Square Linear Fits Calculated to Correct Teo-Lee Fits for Number of Atoms in a Shell (See Figure 14) Continued.

[a] CNO = carbon or nitrogen or oxygen atoms

[b] See Teo-Lee fitting model in text.

[c] MnTPPCl = Chloro-α,β,γ,δ-tetraphenylporphinato (pyridine) manganese(III)

Mn(3,4)Bipy = di-μ-oxo-tetrakis(2,2'-bipyridine) dimanganese(III,IV)

Mn(3,4)Phen = di-μ-oxo-tetrakis(1,10-phenanthroline) dimangenses(III,IV)

Mn(4,4)Phen = di-μ-oxo-tetrakis(1,10-phenanthroline) dimanganese(IV,IV)

[d] These values were not included in the least squares fit. See Figure 13.

[e] Letters and numbers in parentheses refer to Figure 13.

(b) MANGANESE CORRECTIONS

	Multiple Manganese Atoms in a Peak		
	Sample[a]	σ[b]	Correction Factor Needed
(1)	Mn_4N	-.0165	2.35
(2)	Mn_2O_3	-.0180	1.75
(3)	α-MnO_2	+.00075	3.05

Table 7. Least Square Linear Fits Calculated to Correct Teo-Lee Fits for Number of Atoms in a Shell (See Figure 14) Continued

(b) MANGANESE CORRECTIONS - Multiple Manganese Atoms in a Peak, continued.

	Sample[a]	σ[b]	Correction Factor Needed
(4)	α-MnS	-.0397	0.97
(8)	Mn_3O_4	+.00006	3.28

Fitting result (standard deviations in parentheses):

$$\text{Scale Factor}_{\text{multi Mn}} = 55.7\ (77)\ \sigma + 3.098\ (161)$$

Single Manganese Atom in a Peak (Used same slope as for multiple manganese atoms and changed constant)

(5)	Mn(3,4)Bipy[c]	-.00679	1.33
(6)	Mn(4,4)Phen[c]	-.00688	1.27
(7)	Mn(3,4)Phen[c]	-.0105	0.83

Fitting result for new constant, same slope:

$$\text{Scale Factor}_{\text{single Mn}} = 55.7\ \sigma + 1.592$$

[a] Number of sample refers to Figure 13.

[b] See Teo-Lee fitting model in text.

[c] See note c, Table 7(a) for proper names.

Table 8. Comparative Results of Two Shell Fits on the Third Shell of α-MnO_2 (One Shell Manganese Fits Included for Comparison)

Crystallographic Structure: 6 oxygen atoms at 3.41Å, and
4 manganese atoms at 3.45Å

(a) H - D FITS

Fitting Shell	Fitted Distance	Fitted No. of Atoms	Average Fitting Error[a]
With One Shell			
1) Manganese	3.417	3.3	.804
With Two Shells			
1) Oxygen	3.187	7.0	.431
Manganese	3.412	3.6	
2) Oxygen	3.377	-11.6	.508
Manganese	3.403	3.9	

(b) T - L FITS

Fitting Shell	Fitted Distance	E_0 +6500eV	σ[b]	Fitted No. of Atoms	Corrected No. of Atoms	Average Fitting Error[a]
With One Shell						
1) Manganese	3.423(13)	53.6	+.00075	1.31	4.1	.187

Table 8. Comparative Results of Two Shell Fits on the Third Shell of α-MnO_2 (One Shell Manganese Fits Included for Comparison) Continued

Fitting Shell	Fitted Distance	E_0 +6500eV	σ^b	Fitted No. of Atoms	Corrected No. of Atoms	Average Fitting Error[a]
With Two Shells						
1) Oxygen	3.515	65.0	+.0128	1.62	9.0	.003
Manganese	3.414	59.5	+.0114	0.58	2.2	

[a] Average least square error per point when weighted by k^3.

[b] See Teo-Lee model equation in text.

Table 9. Teo-Lee Model Fitting Results on As_2O_3

Fitting Shell	Average Distance	Fitted Distance	E_{0i}	σ_i	Fitted No. of Atoms	Corrected No. of Atoms
First Peak						
6 oxygens	1.80	1.80(2)	11888(5)	-.0024	1.3	3.0
Second Peak						
3 oxygens	3.02	3.02(4)	11937	+.0200	0.4	2.8
3 arsenics	3.23	3.22(2)	11872	+.0053	0.3	--[a]

[a]No correction factor available for arsenic

Table 10. Corrected EXAFS Differences Using Non-Distorted Model Compound Distances (See Tables 3, 4, and 5)

		H - D	T - L Differences	
Compound[a]	Distance[b]	Differences	w/ Amp	w/o Amp
Oxygen				
$Mn_2P_2O_7$	2.083	-.075	-.080	-.086
$Mn(II)AcAc_2 \cdot 2H_2O$	2.140	-.020	-.012	-.035
$Mn(II)Oxalate \cdot 2H_2O$	2.149	-.048	-.028	-.035
Mn_3O_4	1.958	+.024	+.037	+.028
$Mn(III)AcAc_3$	1.935	(ref)	+.025	+.020
Fluorine				
$XeFAsF_6$	1.730	+.027	+.003	-.002
$Xe_2F_3AsF_6$	1.731	+.012	+.008	-.003

[a] See Table 3 for Correct Compound Names

[b] Average distance excluding the minority long or short ligand distances.

Table 11. Use of "Full" EXAFS Fits for Element Identification

(a) USING THE HODGSON-DONIACH MODEL

Sulfur peak of α-MnS. 6 atoms at 2.612Å

Fitting Shell	Distance	No. of Atoms	Average Fit Value
Nitrogen	2.663	-3.35	.137
Oxygen	2.645	-6.64	.143
Sulfur	2.601	1.91	.041
Manganese	2.610	-0.66	.270

(b) USING THE TEO-LEE MODEL

Fitting Shell	Distance	σ	No. of Atoms	E_0	Average Fit Value
i) Manganese peak of Mn(3,4)Bipy[a]. 1 atom at 2.716Å					
Nitrogen	2.702(46)	+.0040	1.32	6558.5	.192
Oxygen	2.685(42)	+.0045	1.04	6560.3	.198
Sulfur	2.684(24)	-.0004	-0.68	6560.2	.070
Manganese	2.683(12)	-.0068	0.75	6548.6	.016

Table 11. Use of "Full" EXAFS Fits for Element Identification. Continued

ii) Oxygen peak of $Mn_2P_2O_7$. 6 atoms; 4 at 2.083Å, 2 at 2.206Å

Fitting Shell	Distance	σ	No. of Atoms	E_0	Average Fit Value
Nitrogen	2.179(50)	-.0077	1.43	6565.8	.097
Oxygen	2.163(48)	-.0066	1.07	6568.5	.102
Sulfur	2.163(63)	-.0146	-0.78	6568.3	.113
Manganese	2.142(80)	-.0291	1.38	6549.3	.158

a See Table 3 for formal name.

Figure Captions

Chapter 3

Figure 1. Absorbance of $CsAsF_6$. The extrapolated fit used for a pre-edge background removal is overplotted. Note monochromator crystal produced "glitch" at 12,150 eV.

Figure 2. Normalized K-shell absorbance of $CsAsF_6$. (a) is the scaled plot; (b) is plotted to an arbitrary expanded scale. The smooth lines in (a) and (b) are plots of the extrapolated post-edge function used for height normalization. The "edge jump" is set equal to 1.0 using this function.

Figure 3. Normalized K-shell absorbance of $CsAsF_6$. (a) is the scaled plot; (b) is plotted to an arbitrary expanded scale. The smooth lines in (a) and (b) are plots of the normalized As K-shell free atom absorbance, μ_M^* (Reference 13). This file is representative of the discrepancies normally observed between μ_M^* and the measured background function.

Figure 4. Comparison of different "Running Average Smooths" applied to $CsAsF_6$ As EXAFS attempting to find the "best" background function. See text for details. Curve (a) is the original $CsAsF_6$ spectrum that was smoothed.

Figure Captions, Chapter 3, Continued

Figure 5. A family of "Kaiser" apodization windows. The window functions are used to multiply the k-space EXAFS before Fourier transforming to reduce sidelobe intensity (see Figure 6).

Figure 6. Fourier Transform magnitudes of window functions, showing the attenuation of sidelobes by the use of a Kaiser window function. In the Fourier transform of actual EXAFS data, the sidelobes would be symmetrically distributed on both sides of each structural peak.

Figure 7. $k^2\chi(k)$ plot of EXAFS data for As_2O_3.

Figure 8. $|\phi_3(R)|$ and $|\phi_1(R)|$ radial distribution function plots of EXAFS data for As_2O_3.

Figure 9. Backscattering amplitudes $|f_i(k,\pi)|$ calculated from original Teo-Lee model.[32] Elements displayed are oxygen, sulfur and manganese.

Figure 10. $|\phi_3(R)|$ radial distribution function plot (dotted curve) of $CsAsF_6$ data with theoretical phase removed and E_0 adjusted so that the imaginary part (solid curve) of the transform peaks at the same position as the magnitude

Figure Captions, Chapter 3, Continued

spectrum ($|\phi_3(R)|$). Note that this peak's position is very close to the true radial position.

Figure 11. $k^3\chi(k)$ plot of $CsAsF_6$ EXAFS data (dotted curve) and the best fit with the amplitude included (solid curve).

Figure 12. Error contour plot for the best fit on $CsAsF_6$ (see Figure 11). The contour for a 100% increase in the fitting error is drawn (solid curve).

Figure 13. Observed amplitude correction factors as a function of σ. Solid curves are linear fits to obtain estimated correlation. See Table 7 for identification of the points.

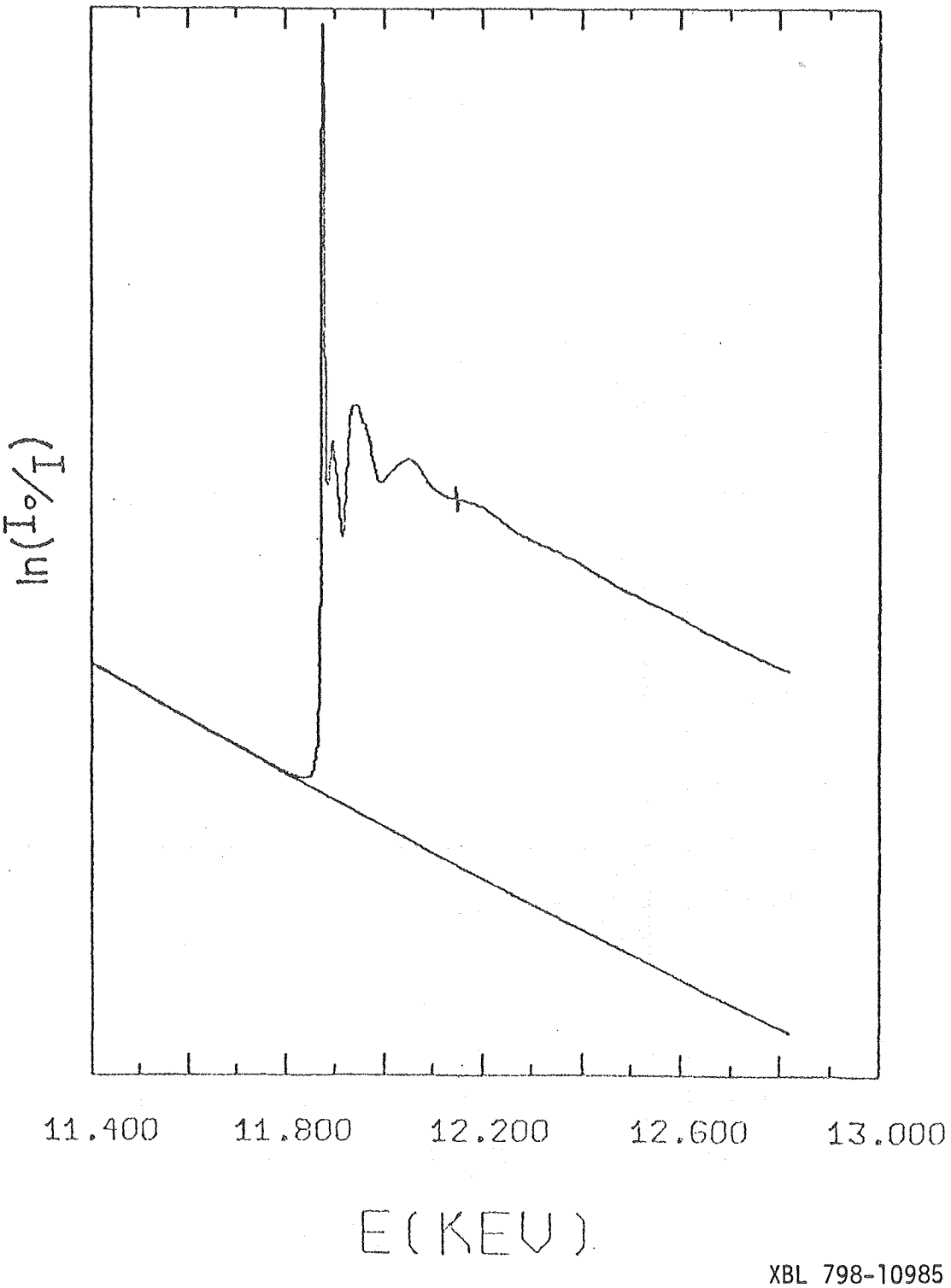

XBL 798-10985

CHAPTER III

Figure 1.

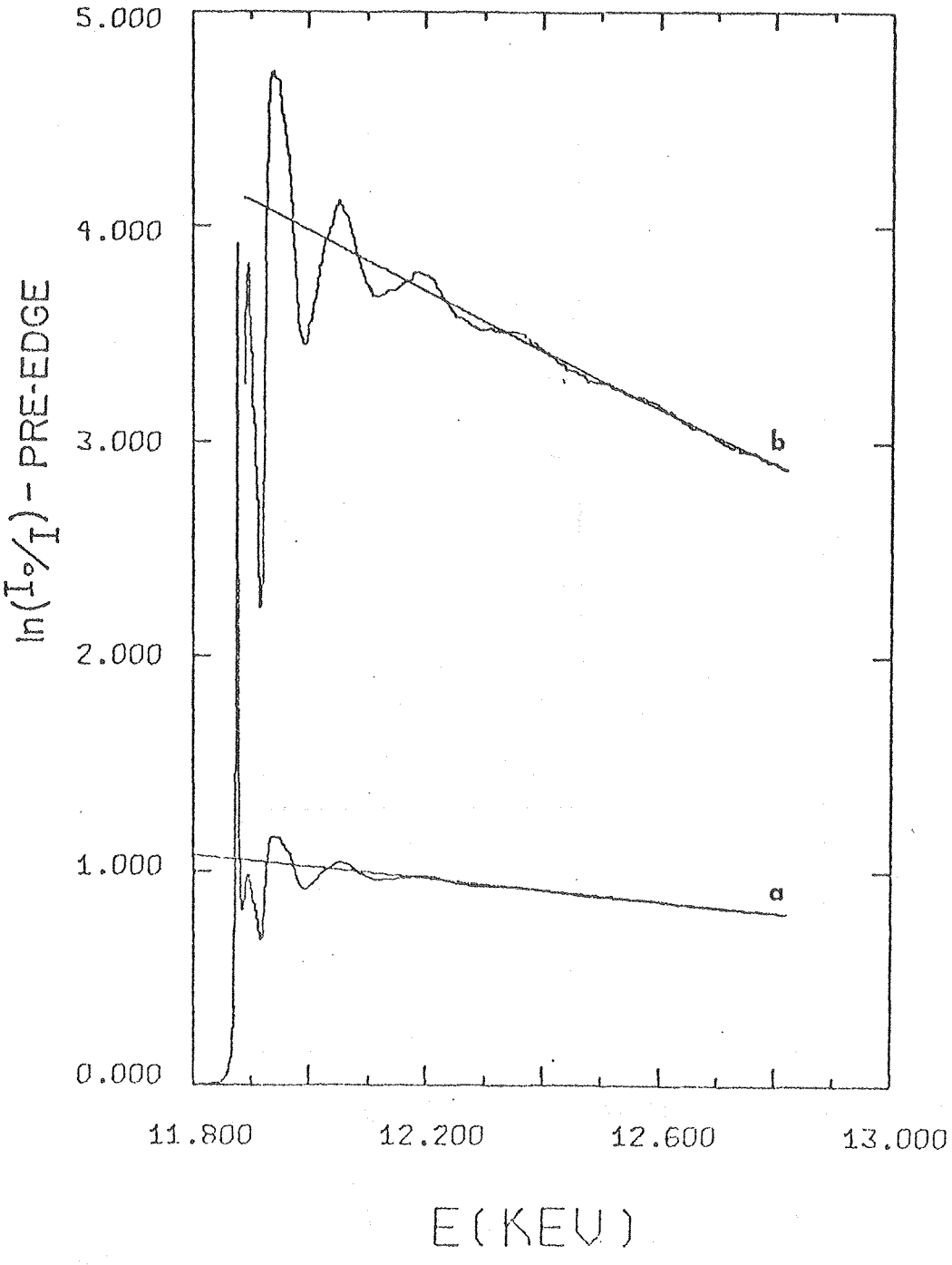

XBL 798-10984

CHAPTER III

Figure 2.

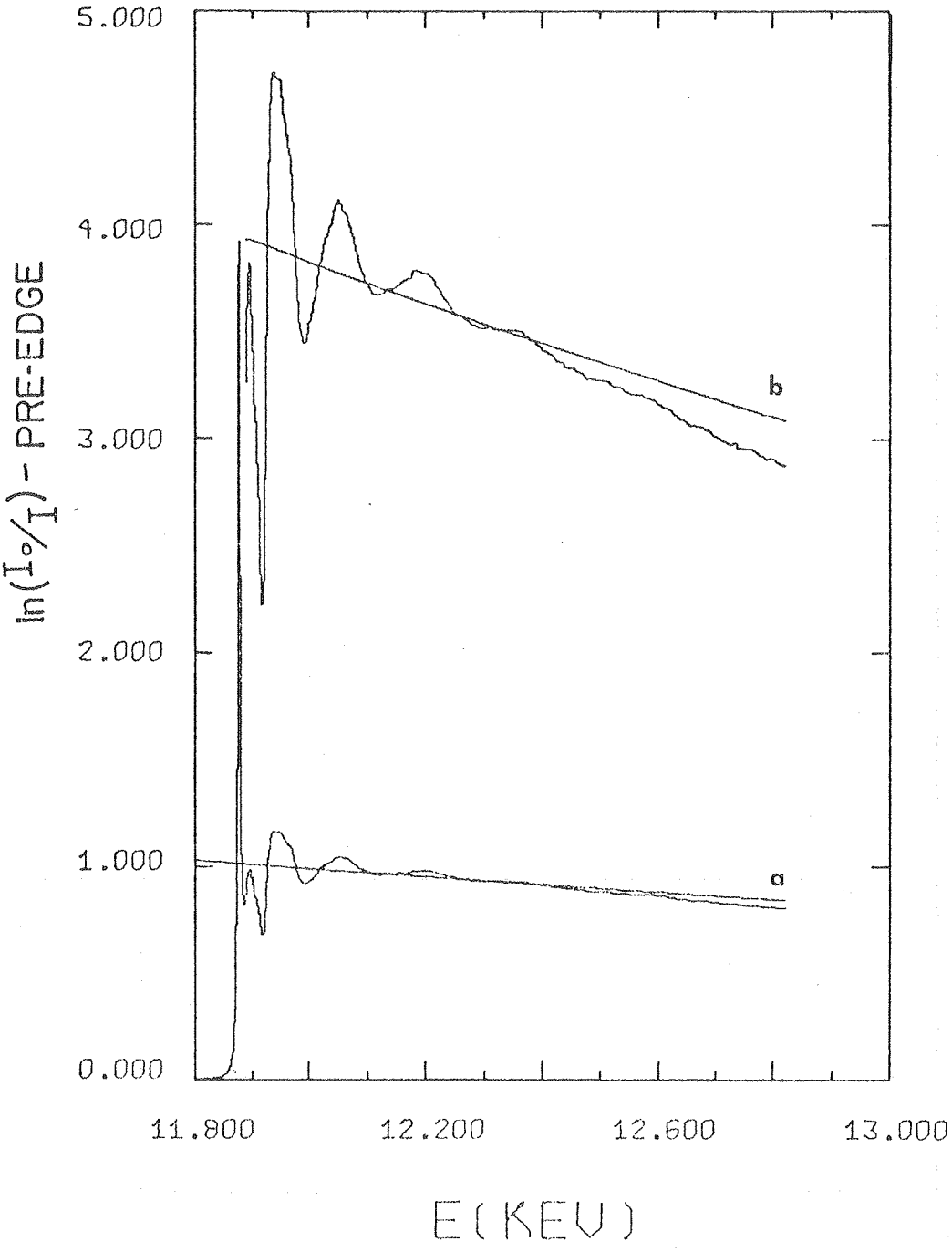

XBL 8011-2603

CHAPTER III

Figure 3.

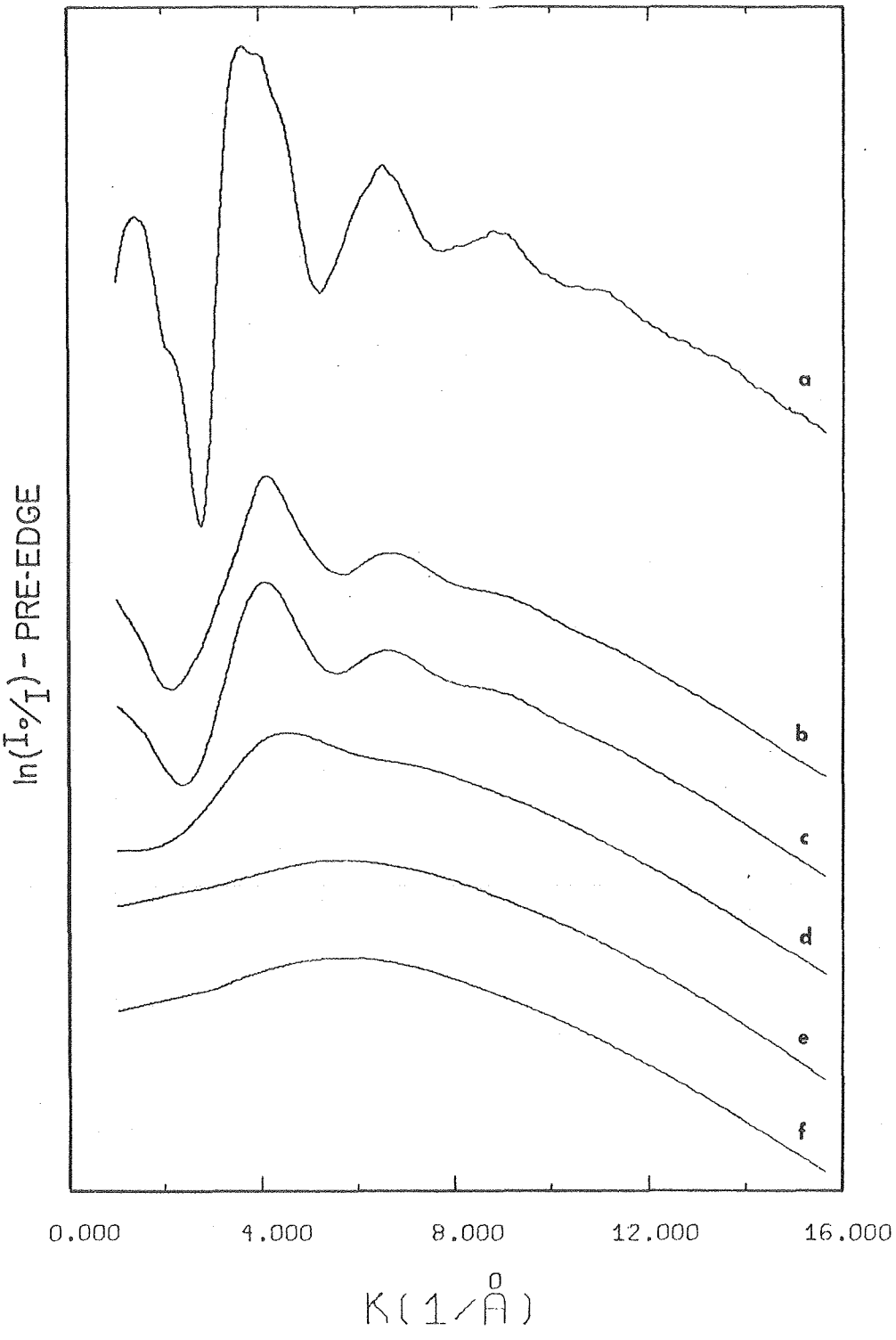

CHAPTER III XBL 8011-2604

Figure 4.

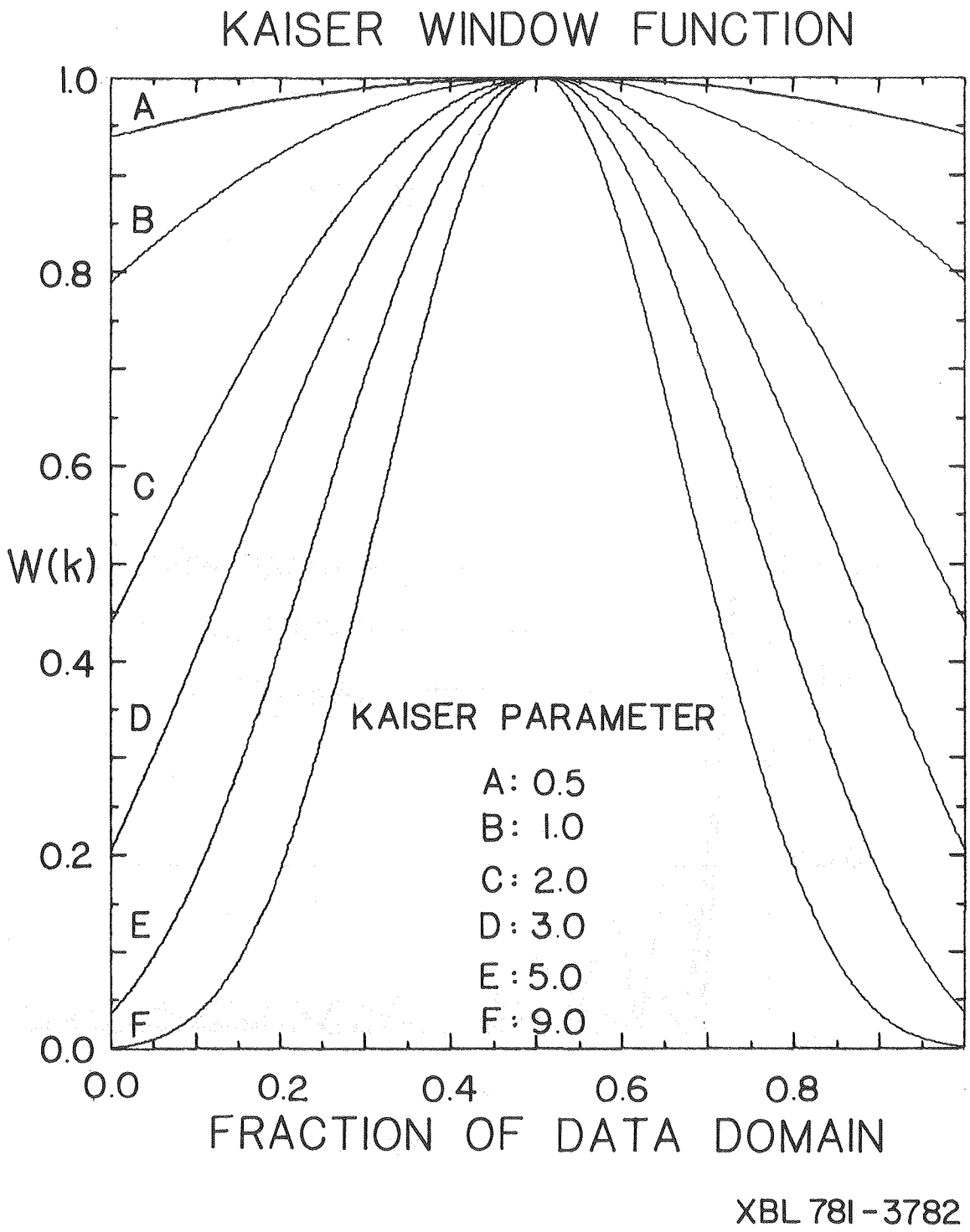

CHAPTER III

Figure 5.

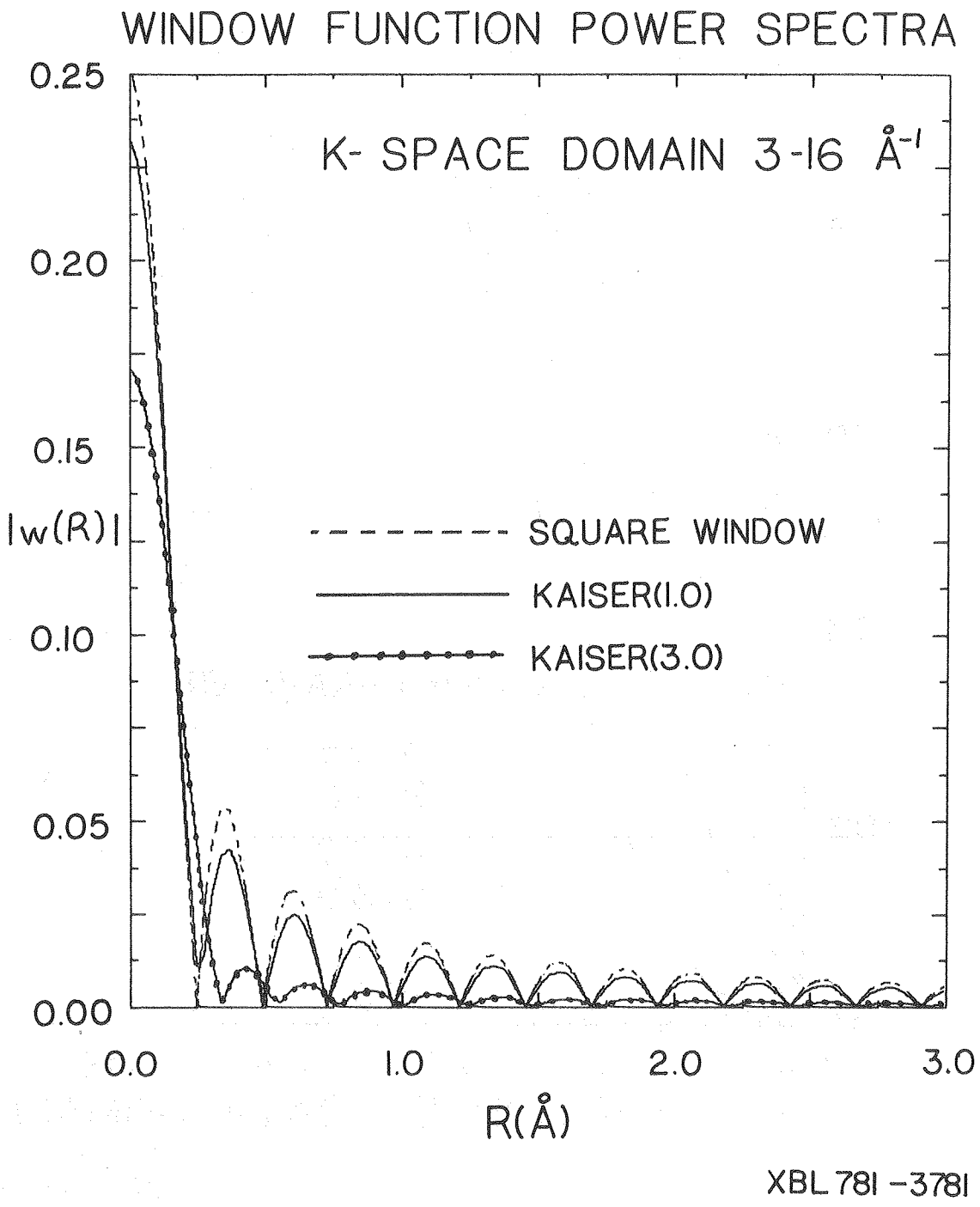

CHAPTER III

Figure 6.

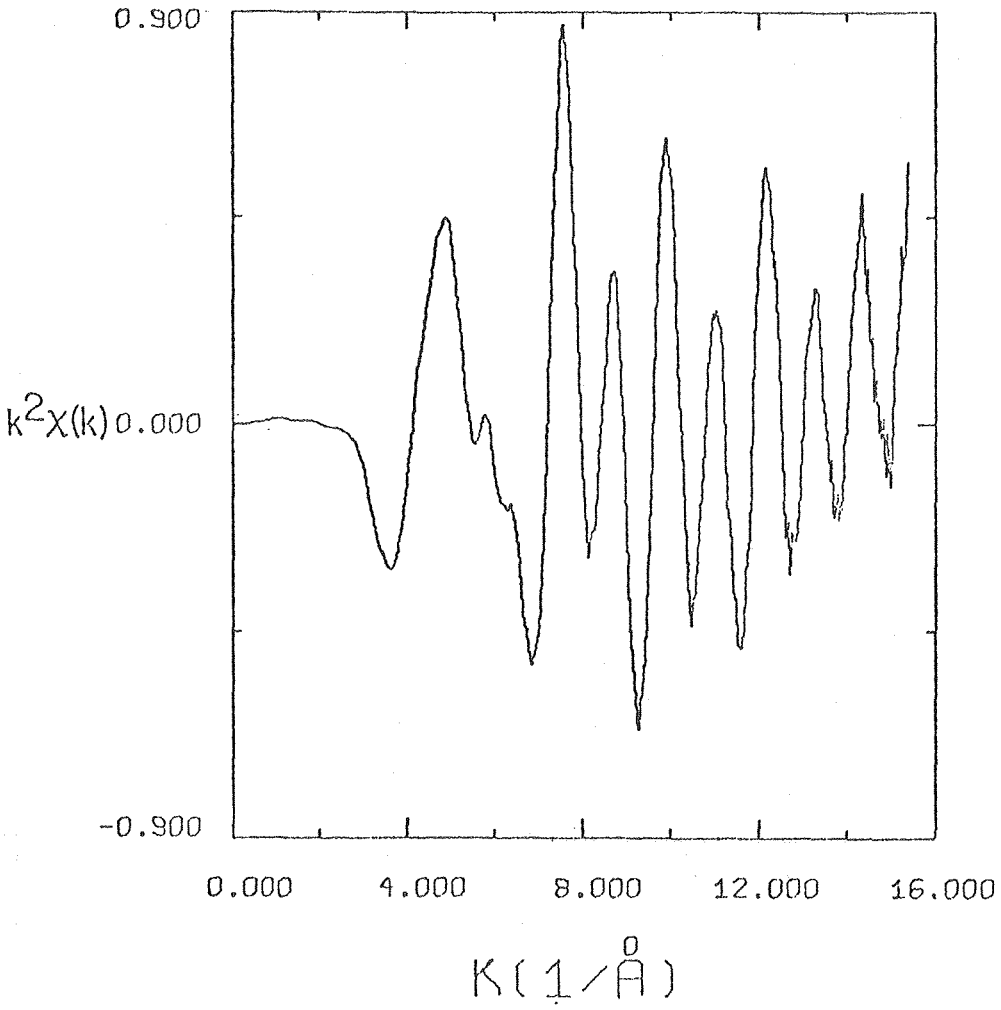

XBL 798-10980

CHAPTER III

Figure 7.

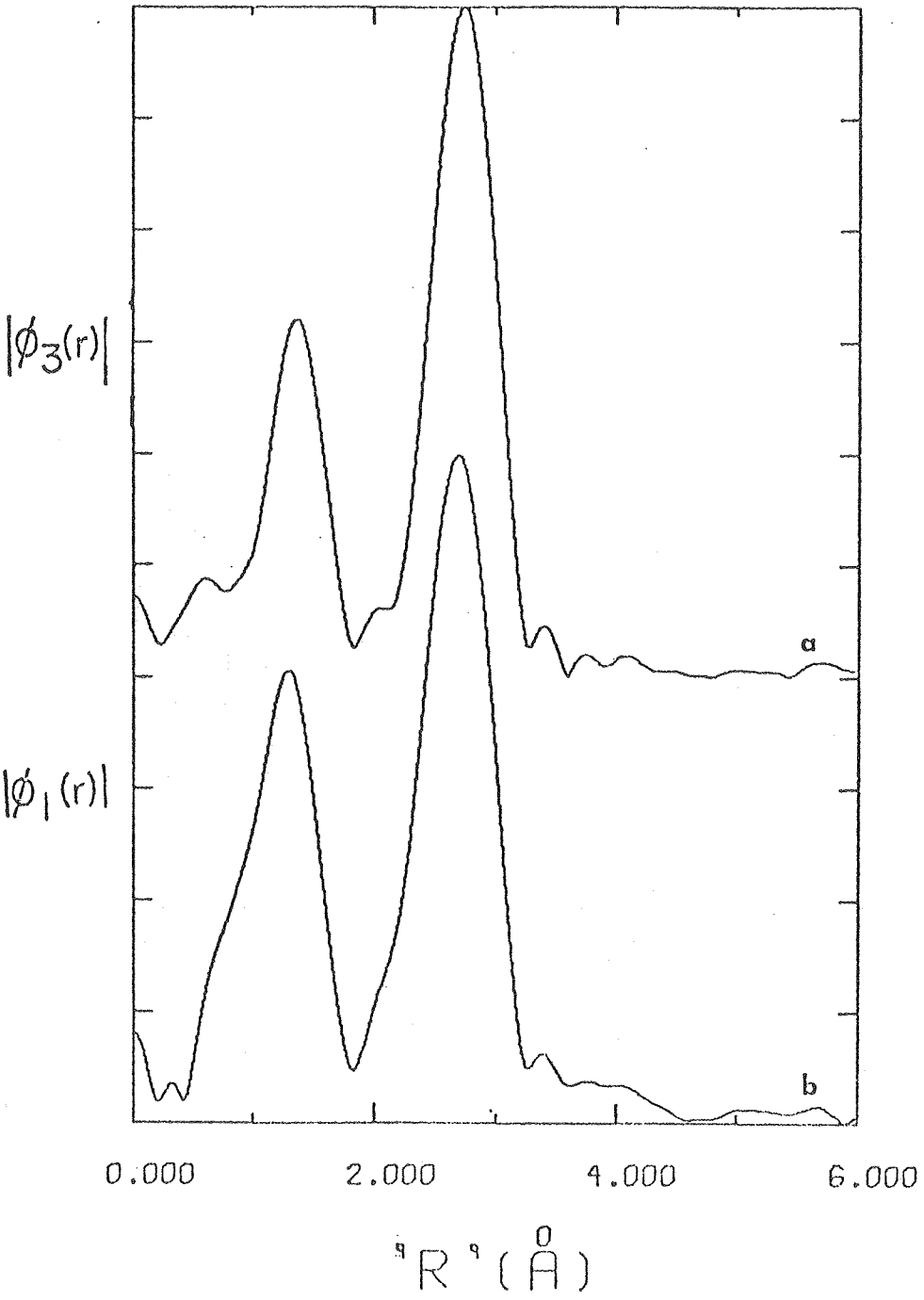

XBL 798-10981

CHAPTER III

Figure 8.

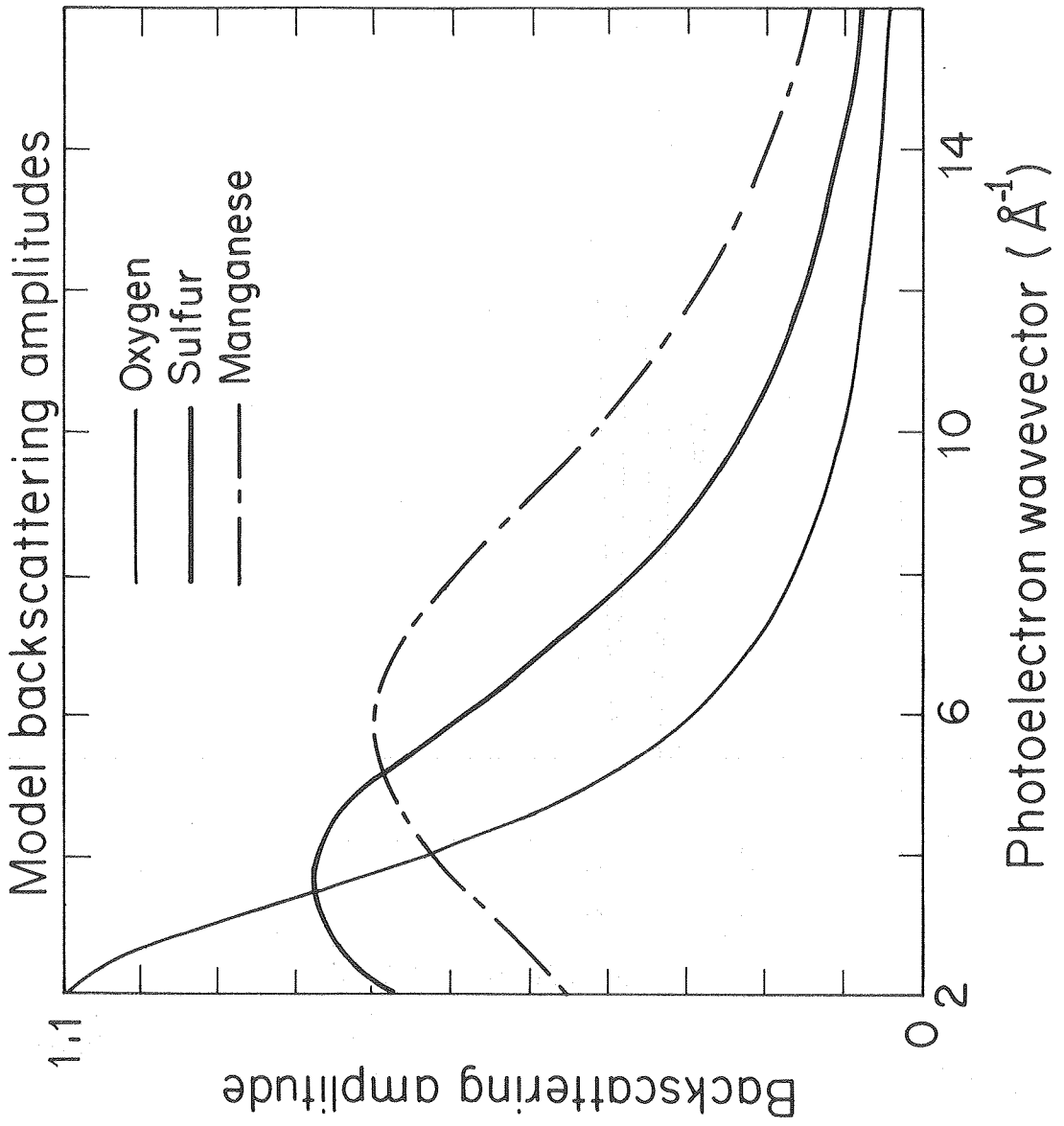

XBL 794-4743

CHAPTER III

Figure 9.

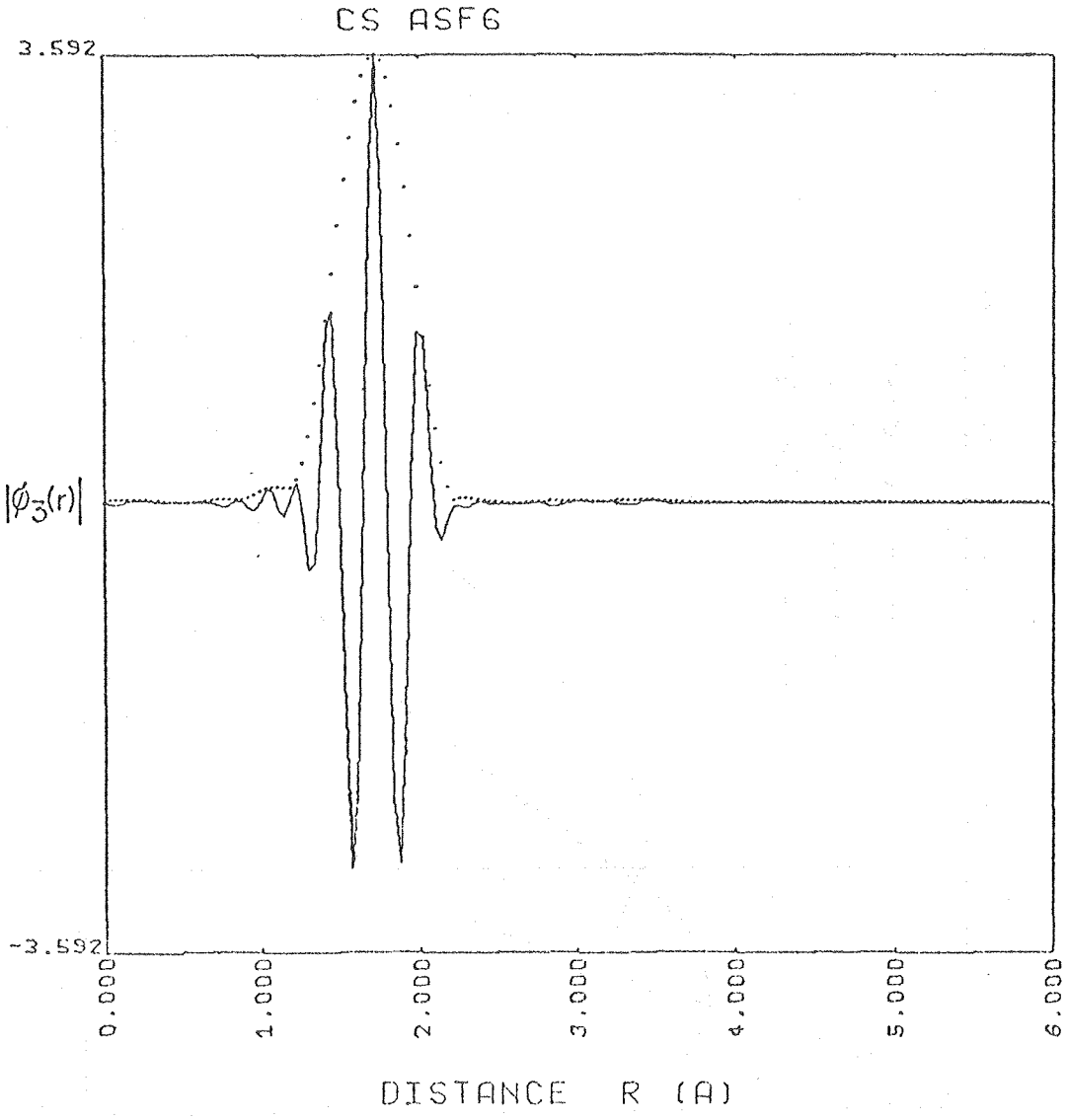

XBL 798-10979

CHAPTER III

Figure 10.

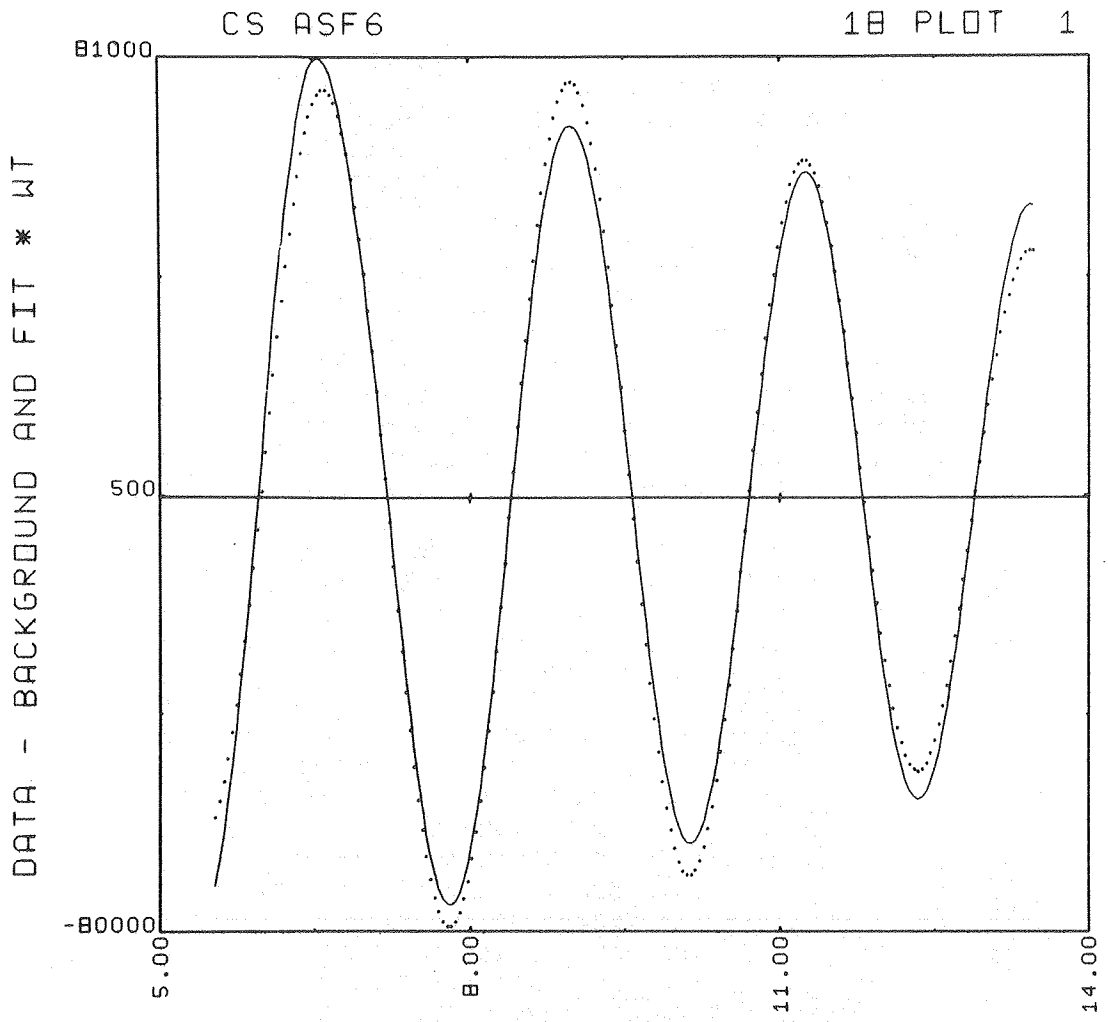

XBL 798-10752

CHAPTER III

Figure 11.

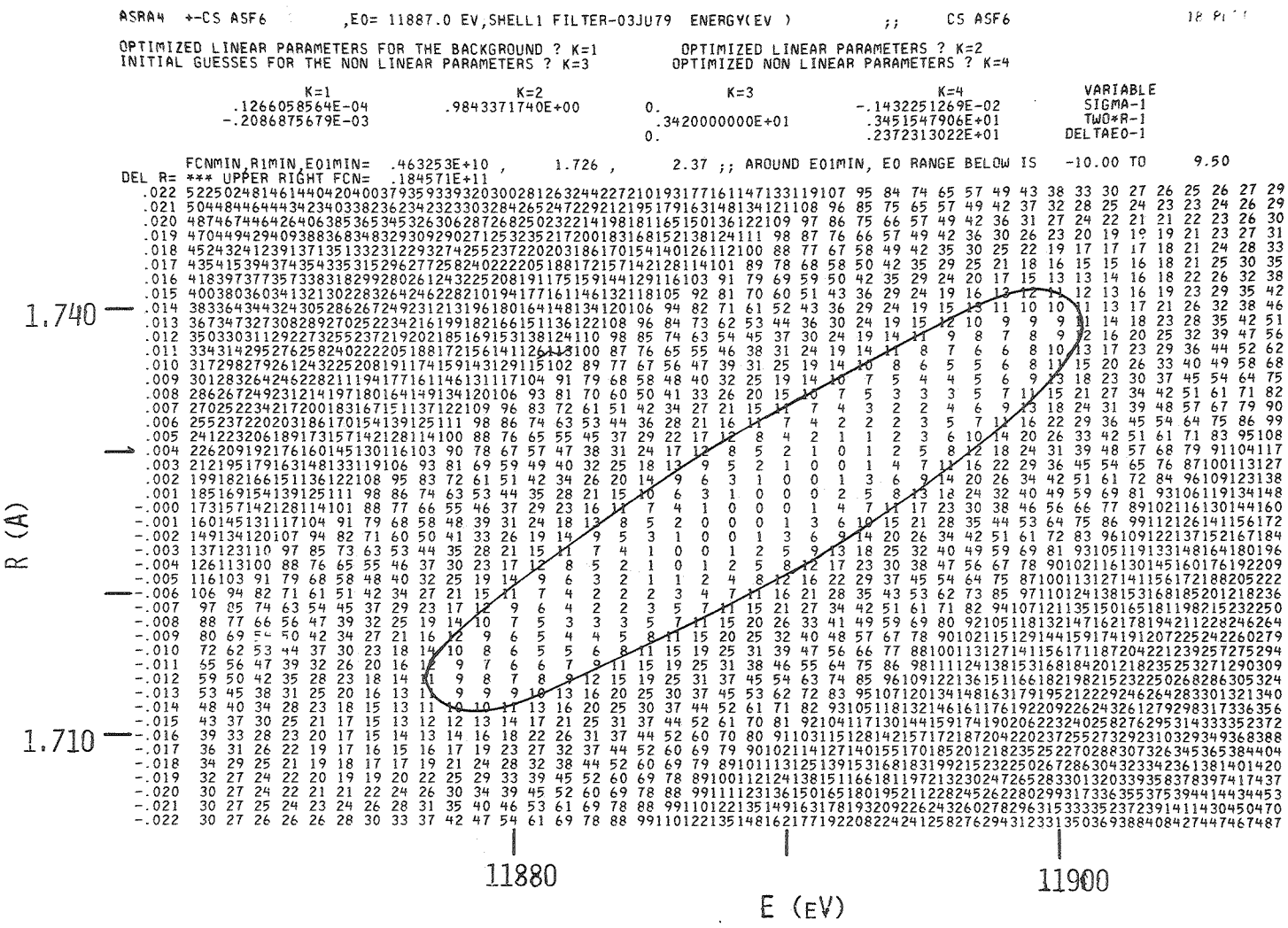

Figure 12.

XBL 798-10987

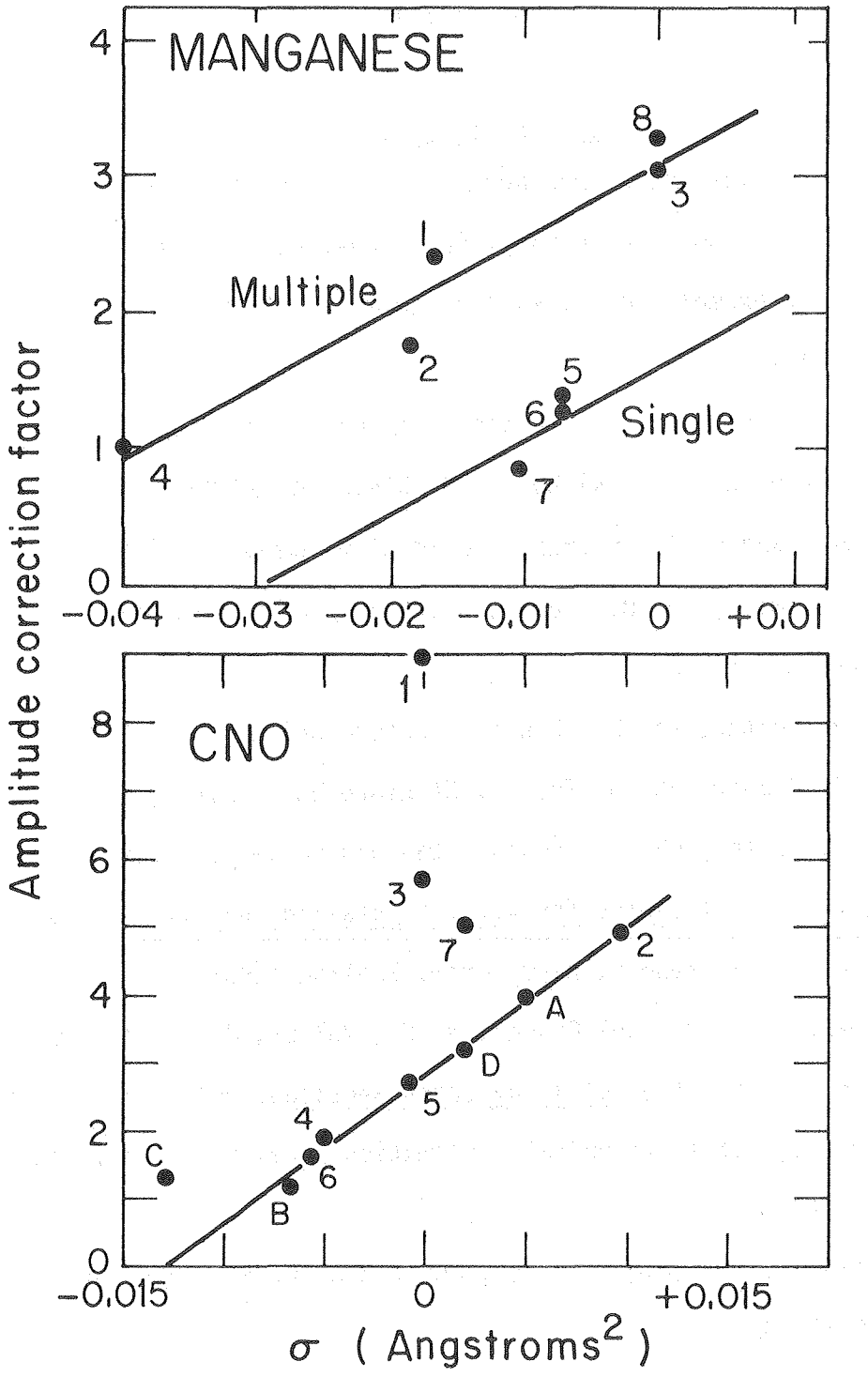

CHAPTER III

Figure 13.

References

Chapter III

1. E. A. Stern, Phys. Rev. B, 10 (1974) 3027
2. C. A. Ashley and S. Doniach, Phys. Rev. B, 11, (1975) 1279
3. P. A. Lee and J. B. Pendry, Phys. Rev. B, 11, (1975) 2795
4. See for example, R. E. Watson and M. L. Perlman, Science, 199 (1978) 1295
5. B. M. Kincaid, Ph. D. Thesis, Stanford University (1975).
6. J. Jaklevic, J. A. Kirby, M. P. Klein, A. S. Robertson, G. S. Brown, and P. Eisenberger, Solid State Comm. 23, (1977) 679.
7. J. P. Smith, Ph. D. Thesis, University of California, Berkeley, (1978).
8. S. H. Hunter, Ph. D. Thesis, Stanford University (1977).
9. S. P. Cramer, Ph. D. Thesis, Stanford University (1978).
10. T. K. Eccles, Ph. D. Thesis, Stanford University (1978).
11. International Tables for X-ray Crystallography III, ed. K. Lonsdale, et al, Kynoch, Birmingham, England (1962).
12. McMaster, W. H., Del Grande, N. K., Mullet, J. H., and Hubbell, J. H., Compilation of X-ray Cross Sections, UCRL-50174, Section II Rev. I., Nat'l. Technical Information Service, Springfield, VA (1969).
13. Lytle, F. W., Sayers, D. E., and Stern, E. A., Phys. Rev. B., 11, (1975) 4825.
14. A. S. Robertson, Ph. D. Thesis, University of California, Berkeley (1979). Del Grande, N. K., in Proceedings of the International Symposium on X-ray Spectroscopy and Electronic Structure of Matter.,

References, Chapter III, continued.

ed. A. Faessler, University of Munich Press, Munich (1973) 183.

15. S. P. Cramer, T. K. Eccles, F. Kutzler, K. O. Hodgson, and S. Doniach., J. Am. Chem. Soc., 98, (1976) 8059.
16. B. K. Teo, P. Eisenberger, and B. M. Kincaid. J. Am. Chem. Soc. 98, (1978) 1735.
17. F. W. Lytle, private communication.
18. S. P. Cramer, private communication.
19. T. M. Hayes, private communication.
20. E. A. Stern, D. E. Sayers, and F. W. Lytle. Phys. Rev. B., 11 (1975) 4836.
21. J. F. Kaiser, System Analysis by Digital Computer, F. F. Kuo and J. F. Kaiser, eds. J. Wiley and Sons, New York (1966).
22. T. M. Hayes, P. N. Sen, and S. H. Hunter, J. Phys. C: Solid State Phys. 9, (1976) 4357.
23. D. Sayers, private communication.
24. R. B. Blackman and J. W. Tukey, The Measurement of Power Spectra, Dover, New York (1958).
25. R. G. Shulman, Y. Yafet, P. Eisenberger, and W. E. Blumberg. Proc. Nat'l. Acad. Sci. - U.S.A., 73 (1976) 1384.
26. G. Martens, P. Rabe, N. Schwentner, and A. Werner, Phys. Rev. B. 17 (1978) 1481.
27. B-K. Teo and P. A. Lee, J. Am. Chem. Soc. 101 (1979) 2815.

References, Chapter III, continued.

28. There seems to be an unexplained exception to this rule in the case of certain chloride ligands in certain compounds (such as $MnCl_2 \cdot 4H_2O$). For example, see Tables 3 and 5.

29. F. W. Lytle, G. H. Via, and J. H. Sinfelt, J. Chem. Phys. 67 (1977) 3831.

30. See for example, A. V. Oppenheim, R. W. Schaefer, and T. G. Stockton, Proc. I. E. E. E., 56 (1968) 1264.

31. J. A. Kirby, A. S. Robertson, J. P. Smith, A. C. Thompson, S. R. Cooper, and M. P. Klein (submitted to J. A. C. S.).

32a. B-K.Teo, P. A. Lee, A. L. Simons, P. Eisenberger, and B. M. Kincaid. J. Am. Chem. Soc. 99 (1977) 3854.

b. P. A. Lee, B-K Teo, and A. L. Simons, J. Am. Chem. Soc. 99 (1977) 3856.

33. W. E. Blumberg, private communication.

34. P. R. Bevington, Data Reduction and Error Analysis for the Physical Sciences, McGraw-Hill, New York (1969) 164.

35. F. James. "Function Minimization", Proc. of 1972 CERN Computing and Data Processing School, Pertisau, Austria, 10-24 September (1972. CERN document 72-21.)

36. J. A. Nelder and R. Mead. Computer J. 7 (1967) 308.

37. W. C. Davidson, Computer J. 10 (1968) 406.

38. P. A. Lee and G. Beni. Phys. Rev. B., 15 (1977) 2862.

39. A. S. Robertson, B. M. McQuillan, and N. Bartlett (submitted).

40. P. Eisenberger and G. S. Brown, Solid State Comm. 29 (1979) 481.

References, Chapter III, continued.

41. J. A. Kirby, D. B. Goddin, T. Wydrzynski, A. S. Robertson, and M. P. Klein (submitted to J. A. C. S.).

CHAPTER IV

EXAFS RESULTS ON SOME DI-MANGANESE MODEL COMPOUNDS AND ON THE MANGANESE IN PHOTOSYNTHETIC SPINACH CHLOROPLASTS

INTRODUCTION

Since the original observation in 1937 by Pirson[1] of an absolute requirement in photosynthesis for the trace element Manganese, the specific role that Mn plays has been a subject of extensive research. The general consensus is that the Mn is directly involved in photosyntehtic oxygen evolution either at the active site or as a critical component of the electron transport chain (see review by Radmer and Cheniae[2] for further details). Until now all observations which have been made concerning the activity of the chloroplast bound Mn have been by indirect methods such as NMR water proton relaxation experiments[3] and Mn release experiments using some chemical[4] or physical[5] treatments. The experimental work reported in this chapter and Chaper 5[6] is the first direct observation of the Mn contained in chloroplasts in its active environment. The technique used was X-ray Absorption Spectroscopy (XAS) utilizing the tunable X-ray sources at the Stanford Synchrotron Radiation Laboratory (SSRL), Stanford, CA.

Two types of information can be obtained from XAS. The first is an estimate of the formal oxidation state of the element of interest using X-ray Absorption Edge Spectroscopy. Such studies on the Mn in chloroplasts are reported in the following chapter.[6] The other information allows the determination of the local structure around the atom whose XAS spectrum is being obtained. This type of experiment utilizes the post-absorption edge modulations of the photoelectron

cross section which is known as Extended X-ray Absorption Fine Structure (EXAFS). The theoretical basis of the effect has been well established by Stern and by Ashley and Donaich in references 7 and 8, respectively. Analysis of the modulation patterns yield the radial distances to the neighboring atoms. To some extent the backscattering probabilities can be used for elemental identification of the ligating atoms.[9,10]

It has been known for many years that there are at least two different classes of Mn in chloroplasts. The larger fraction, the "loosely bound pool", is known to be essential for O_2 evolution. This "loosely bound pool" represents approximately 2/3 of the total Mn and the release from its normal site into an aqueous phase can be accomplished by physical and chemical methods.[2] To differentiate between these two classes of Mn, X-ray spectra were collected on chloroplasts capable of oxygen production ("active" chloroplasts) and on chloroplasts which had the "loosely bound pool" of Mn completely removed and thus were incapable of oxygen evolution ("inactive" chloroplasts).

MATERIALS AND METHODS

The preparation of various chloroplast samples is detailed in the next chapter[23] and will not be repeated here. The two samples used were an "active" broken chloroplast pellet and an "inactive" chloroplast pellet which had the "loosely bound pool" of Mn removed by treatment with Tris buffer (Tris = alkaline tris-(hydroxymethyl)-aminomethane) followed by osmotic shock. Complete removal of all aqueous Mn^{+2} was monitored by measurements of the Mn^{+2} EPR signal.

A number of model compounds were prepared or purchased for comparison with the chloroplast samples. The three reported here, di-μ-oxo-tetrakis(2,2'-bipyridine) dimanganese (III,IV) perchlorate [Mn(3,4)Bipy], di-μ-oxotetrakis(1,10-phenanthroline) dimanganese (III,IV) perchlorate [Mn(3,4)Phen], and di-μ-oxo-tetrakis(1,10-phenantroline) dimanganese (IV,IV) perchlorate [Mn(4,4)Phen], were prepared and characterized by literature methods.[11,12,13] The powdered crystalline samples were mixed with a binding agent of powdered cellulose and pressed into 1-1/4 inch diameter pellets in sufficient quantities so that approximately 90% of the incident X-ray flux was absorbed in the sample when the X-ray energy was just higher than the Mn K or 1s absorption edge.

EXPERIMENTAL

The X-ray absorption spectra were obtained at the Stanford Synchrotron Radiation Laboratory (SSRL). The model compound data were collected in the standard absorption mode, described elsewhere.[14] Due to the very low concentration of Mn in the chloroplast samples (of the order of 100 μM) and the large background absorption by the rest of the sample (e.g. water, protein, and phospholipid) it was not possible to collect usable absorption data in a reasonable period of time. The chloroplasts spectra were, instead, collected in the fluorescent detection mode where the relative X-ray absorbance was obtained by measuring the excitation function for X-ray fluorescence characteristic of Mn.[16] The X-ray detector used was a triplet Si(Li) solid state detector built by the Nuclear Instrument and Methods Group at

Lawrence Berkeley Laboratory.[17] Even with the sensitivity enhancement provided by the fluorescent EXAFS technique[16], it was still necessary to use the focused X-ray line[15] at SSRL to obtain as intense an incident X-ray flux as possible. The "active" chloroplast spectra were obtained in approximately 24 hours on a focussed line. The inactive chloroplast spectra were obtained in approximately the same amount of beam time two weeks later. The large number of individual spectra were eventually co-added to produce one data analysis spectrum for each sample.

General Data Analysis Method. EXAFS data processing is described in detail in Chapter 3[18] and thus will be only briefly outlined here.

The first step was to condense the numerous individual spectra that were collected on each sample into one final co-added spectrum. A significant problem at this step was to maintain an energy reference for each spectrum relative to a pre-selected standard. For the chloroplast spectra this presented some problems which are addressed later. The data are then expressed as a relative EXAFS modulation, generally defined by[7,8]

$$\chi(k) = [\mu(k) - \mu_{BG}(k)]/\mu_o(k) \qquad (1)$$

where χ is the fine structure modulation (EXAFS), μ is the observed X-ray absorption cross section, μ_o is the photoelectric cross section for the free atom, and μ_{BG} is the experimentally derived background which in the absence of experimental baseline would be the free atom photoelectric cross section μ_o. As indicated in Equation 1, the

EXAFS modulation, χ, is not expressed as a function of the incident X-ray photon energy but as a function of the resultant photoelectron wave vector defined by

$$k = 2\pi(2m_e(E-E_o))^{\frac{1}{2}}/h \qquad (2)$$

where k is the photoelectron wavevector, E is the energy of the incident photon, E_o is the K-shell binding energy, m_e is the mass of the electron and h is Planck's constant.

To obtain $\chi(k)$ from an X-ray spectrum, a number of procedures are utilized. First, a preabsorption edge background is removed from the spectrum. Then the spectrum is divided by the free atom photoelectric cross section (Victoreen formula) and a low frequency background is removed. Since only relative absorption cross sections are treated, it is necessary to normalize the spectrum to obtain an edge height of one. In the final operation, the energy spectrum is expressed as a function of photoelectron wave vector space, hereinafter called k-space. To make this conversion it is necessary to choose a value for the binding energy, E_o for the excited K-electron. At the present time there is no reasonable <u>a priori</u> method for estimating E_o, so approximate values are used for the first iteration.

The next analysis step is to examine the power spectra of the Fourier transforms of $\chi(k)$ multiplied by different powers of k ($k^n\chi(k)$). As can be seen from the theoretical form for $\chi(k)$[7,8] (Chapter 2)

$$\chi(k) = \sum_{i=1}^{n_s} \frac{N_i}{kR_i^2} e^{+\sigma_i k^2} |f_i(k,\pi)| \sin(2kR_i + \alpha_i(k)) \quad (3)$$

(where n_s = number of scattering shells N_i = number of atoms in the i^{th} shell, R_i = distance to the i^{th} shell in Angstroms (Å), $f_i(k,\pi)$ = backscattering amplitude for the i^{th} shell, σ_i = disorder parameter for the i^{th} shell, and $\alpha_i(k)$ = scattering phase shift). The Fourier transform of the k-space data yields a radial distribution function of the neighboring atoms hereafter called R-space. However, the Fourier transforms give only approximate distances and tentative elemental identifications, due to nonlinearities in the phase shift functions $\alpha_i(k)$ and asymmetry of the amplitude functions $f_i(k,\pi)$. More exact determinations are made by curve fitting.

The Teo-Lee model[9] and the Hodgson-Doniach model[19] were used in curve fitting. In the Teo-Lee model, theoretical calculations are used for $f_i(k,\pi)$ and $\alpha_i(k)$ in Equation 3 and the values of N_i, σ_i, R_i and E_{oi} are simultaneously fit.[18] In the H-D model, simple functional forms for $f_i(k,\pi)$ and $\alpha_i(k)$ are assumed and experimental data on model compounds are used to determine them for particular absorber-backscatter pairs.[19]

Each model has its own merits and limitations.[18] In general, the T-L model has the ability to give reasonable fits with highly disordered and chemically altered systems; for certain types of multi-shell fits there are too many parameters. The H-D model, on the other hand, has the advantage of simplicity and fewer fitting parameters (only N_i and R_i); it generally gives unreliable values for the number of scatters and poorer fits.[18] In the following

discussion, the H-D fits will be included in the tables of results for comparison, but in general will not be discussed.

Thus, the general analysis procedure is to perform the Fourier transforms and make estimates of the radial distances and guesses for the elements contributing to a given R-space feature. These values and guesses are then used as the starting points in the curve fitting.

The first curve fits performed are on resolved peaks in the R-space Fourier transforms. These fits are used to make element identifications and the first determination of the true radial distance to the atoms represented by the peak. The resolved peak is isolated by applying a window function and this feature is then transformed back to K-space for fitting. A number of single shell fits are performed using the parameters for several reasonable choices of backscattering elements. Using the criteria explained in Chapter 3[18], the element identifications and radial distance determinations are made. If two or more R-space peaks are very close together, it is not possible to accurately use the single peak Fourier isolation method. It is then necessary to isolate the composite peak and compute multi-shell fits to make reasonable identification of the ligands involved and their distances. It is often very useful to create simulated data and compare the Fourier transforms and fitting results with the unknown system. The simulated data are essentially equivalent to creating model compounds of known structure. These often aid in identification of complex multi-distance R-space peaks.

The last analysis step is to perform multi-shell fits on a Fourier isolated k-space spectrum which includes all the R-space peaks

of interest. This isolation step is only used to remove the residual low frequency background and high frequency noise, thereby greatly improving the precision of the fits.

If a single peak can be isolated, there is one additional method that can be used. With single peaks it is possible to remove the amplitude from the spectrum leaving only a non-linearily phase modulated sine wave. This permits phase-only T-L fits, which often results in better distance determinations than do total fits.[18] These phase only fits also provide a method of obtaining distance error estimates.[18] All the single shell phase only fits that were performed can be identified in the tables by the presence of error estimates.

RESULTS

Some of the R-space Fourier transform power spectra for the samples studied are presented in Figure 1 and the relative magnitudes and positions for the main peaks are tabulated in Table 2. The representations $k^0\chi(k)$ and $k^3\chi(k)$ indicate that $\chi(k)$ was multiplied by k^0 (=1) and k^3 respectively before the Fourier transform was performed. The purpose in examining the different $k^n\chi(k)$ transforms is to make tentative element identifications. With the exception of highly disordered shells, the heavier the element, the higher its relative Fourier transform peak becomes as the power of k^n increases.[18]

<u>di-μ-oxo-bridged Manganese Dimers.</u> The $k^0\chi(k)$ and $k^3\chi(k)$ R-space Fourier transforms for Mn(3,4)Bipy are presented in Figures 1(a) and

1(b) and the crystal structure is presented in Figure 2. The Fourier transforms for the other two model compounds, Mn(3,4)Phen and Mn(4,4)Phen, are quite similar, so that comparisons of the distances in Mn(3,4)Phen and Mn(4,4)Phen to the known distances in Mn(3,4)Bipy will be made with curve fits.

The curve fitting results are presented in Table 2. Examination of the contents of Figure 1(a) and 1(b) and of Table 2 leads to three immediate observations. First, the actual error for the average distance for the bridge oxygens (0.007Å) is well within the estimated error (0.019Å) for the T-L model so the comparative results for this shell should be quite accurate. Second, the Mn shell is about 0.039Å shorter than the crystal structure distance, but all three Mn results are short of the crystallographic result of approximately 2.72Å. This shortening of the Mn-Mn distance seems to be associated with the di-μ-oxo configuration since the only other model compounds examined which had short Mn-Mn distances were Mn_2O_3 and α-M_nO_2 which are also di-μ-oxo bridged. Their distances were short by almost exactly the same amount.[18] Thus, all consideration of bridged Mn-Mn distances must take this shortening into account.

The final observation is, perhaps, the most obvious one but at the same time the most perplexing. There is no feature corresponding to the four nitrogens in the first coordination sphere. The large heterogeneity in ligand distances may result in a large interference effect which reduces the nitrogen peak to the noise level. This conclusion was verified by creating a number of different simulations

of the oxygen and nitrogen atoms in the first shell of Mn(3,4)Bipy (for an example see Figures 1(i) and 1(j)). The effect will be explained in more detail in the Discussion section.

Chloroplasts. The final co-added spectra for the two chloroplast samples represent approximately 200 seconds of data acquisition per point. The added spectra are presented in Fig. 3.

The reduced counting rate for the "shocked"or inactive chloroplast sample is about that expected if 2/3 of the total Mn is released by the Tris treatment and removed by the osmotic shock. (The two samples were similar but not identical in chlorophyll concentration and the samples were run under slightly different experimental conditions).

Two other experimental effects should be noted. First, due to the much poorer energy resolution on the focussed line (>10 electron volts (eV)), the added spectra could not be energy referenced to better than a few eV. This results in a small additional dampening effect on the EXAFS modulations. Second, it should be noted that although the EXAFS data extend to higher photon energies the presence of the iron K-edge at 7100 eV forces truncationof the useable EXAFS data at that energy (see Figure 3(a)).

The first step in analyzing the chloroplast spectra was to examine the Fourier transforms to obtain estimates of ligand distances. By comparison with model compounds and by utilizing the known structural chemistry of Mn, reasonable guesses can be made regarding ligand identity. It should be noted at this point that differentiation between ligands with similar atomic number is not

possible with EXAFS at the present time. Therefore, when a reasonable low atomic number ligand of Mn is specified, it will be indicated by CNO representing carbon, nitrogen, oxygen, or some mixture. These elements are all known to ligate Mn and their dominant presence in chloroplasts strongly suggests them as the most likely ligands of low atomic number. In a similar manner, the next heavier elements likely to be encountered in chloroplasts are indicated by PClS (P, Cl, S) and MnFe (note: Cu cannot be excluded when Mn or Fe is indicated).

(a) "Active Chloroplasts. Fourier transform power spectra for $k^0\chi(k)$ and $k^3\chi(k)$ of the "active" chloroplast spectrum of Figure 3(a) are presented in Figures 1(c) and 1(d) and tabulated in Table 1. Examination of Figure 1 and Table 1 leads immediately to a comparison between (a) the first peak in the active chloroplasts and the oxygen shell in Mn(3,4)Bipy (both R_{eff} are approximately 1.3Å in the $k^3\chi(k)$ transforms), and (b) the third peak of the active chloroplasts and the Mn shell of Mn(3,4)Bipy (both R_{eff} are approximately 2.3Å in the $k^3\chi(k)$ transforms; both grew out of the noise as n in k^n was increased). This similarity is even more striking when the unusual Mn ligand distances represented by these two peaks are compared with other Mn model compounds.[18] Thus, a good starting point was to assume a CNO first coordination sphere ligand at 1.8Å and a MnFe ligand at 2.7Å, the crystallographic distances for Mn(3,4) Bipy. (see Fig. 2). The fitting analyses problems, however, were complicated by the presence of the second peak in the transform of the active chloroplast. It was too close to the first peak to be isolated so all fits on the first two peaks had to performed on the Fourier isolate of

these two peaks together. However, the relatively short distance of the second peak (approximately 2.2Å) and the known chemistry of Mn again suggested CNO ligands.[6,18]

The next step in fitting the active chloroplast spectrum was to examine the isolated third peak in the Fourier transform. Using the criteria developed for element identification (positive amplitude at expected distance and comparison of the quality of the fit with different elements),[18,19,21]), both fitting models predicted a MnFe atom at an approximate distance of 2.7Å. Due to the high noise level in the spectrum and the lack of a good separation between the peaks, the reported fitting results for this peak are deferred until consideration of the final three shell fits.

The first two peaks were difficult to identify positively. This was finally accomplished by comparing the Fourier isolation of the first two peaks and some of the simulated Mn(3,4)Bipy oxygen-nitrogen first coordination sphere models mentioned earlier. One of the simulations which closely resembled the EXAFS of the active chloroplasts is described in Tables 1 and 3 and its Fourier transforms are presented in Figures 1(i) and 1(j). With this valuable clue it was possible to obtain very good fits to the first two peaks of the active chloroplasts. The isolated spectrum, the simulated spectrum and their best T-L fits are presented in Figure 4. The one and two shell fitting results for the isolated and the simulated spectra are tabulated in Table 3.

The three shell fits (using two CNO first shells and a Mn third shell as indicated above) are tabulated in Table 4. The noise

filtered $k^3\chi(k)$ spectrum and its best T-L fit are presented in Figure 5.

(b) Inactive Chloroplasts. Analysis of the "inactive" chloroplast spectrum was performed with the primary concern of determining the exact extent to which this spectrum, which represents the residual Mn content of chloroplasts after the "loosely bound" Mn was removed, contributes to the "active" chloroplast spectrum. If no evidence of alteration in the state of this "tightly bound" Mn could be found, then an attempt to obtain the $\chi(k)$ spectrum of only the "loosely bound" Mn would be made.

The "inactive" chloroplast Fourier transform power spectra are presented in Figures 1(e) and 1(f) with the peak magnitudes and positions included in Table 1. Examination of the inactive chloroplast transforms shows no apparent correspondence between its first peak and those of any of the active chloroplast peaks. Rather, the peak corresponds to a low valent Mn^{+2} to CNO first coordination sphere distance (approximately 2.1Å when corrected by adding 0.5Å to the $k^3\chi(k)$ results). The second peak of the inactive chloroplasts, however, seems to lie at approximately the same distance as the third active chloroplast peak and may thus contibute to the active chloroplast's third peak. The third inactive chloroplast peak, when the high noise level of the spectra is considered, seems to be compatible with being a normal second coordination sphere ligand (approximately 3.1Å).

Curve fitting on the inactive chloroplasts was not very successful and, as a consequence, only the T-L one shell fitting

results on Fourier isolated R-space peaks are presented in Table 5. The first peak fits show that the ligands observed are definitely CNO-type, but the value obtained for E_o was 10eV lower than any other CNO ligand studied, which explains the failure of the H-D model fits.[18] This unusual result may imply that the first shell is highly disordered, a hypothesis which could only be explored with signficantly better data. The distance observed is approximately 2.1Å which suggests that it could be contributing to the active chloroplasts' second peak. The second and third peaks in the inactive chloroplast power spectrum could not be separated by the Fourier isolation technique and no acceptable two shell fits were obtained. It was necessary to examine the second peak to see if it might be contributing to the third peak in the active chloroplast power spectrum. A Fourier isolation was performed and the one shell fitting results are included in Table 5. Using the criteria developed to approximately identify the element of a transform peak, the one shell results indicate MnFe based on the qualitative features of the fit. In any case, it has the right distance to be present as part of the active chloroplast's third peak and thus could represent about 1/3 of the magnitude of that peak.

From this analysis it appears that the "tightly bound pool" of Mn did not appear to be affected by removing the "loosely bound pool" of Mn. Thus, if the inactive chloroplast spectrum is multiplied by 1/3 and subtracted from the active chloroplast spectrum, the difference should be a reasonable representation of the EXAFS of the "loosely bound" Mn. The resulting Fourier transforms are presented in Figures 1(g) and 1(h) and Table 1.

(c) Difference Spectrum. Examination of the transforms of this "difference" spectrum created to simulate the EXAFS spectrum for the "loosely bound pool" of Mn shows a marked reduction and slight position shift in the second peak and a 25% reduction in magnitude for the third peak when compared to the peaks of the active chloroplasts. This is exactly the result expected from comparing the transform peak magnitude of the active and inactive chloroplasts and then forming the difference in R-space.

The curve fits were then performed in a similar manner as before with the same ligand shells as previously identified for the active chloroplasts. The results are listed in Table 6 and the difference spectrum and its best fit are presented in Figure 6.

DISCUSSION

di-μ-oxo Manganese Dimers. Examination of Table 2 reveals a very interesting structural result. The bridging oxygens in Mn(3,4)Bipy and Mn(3,4)Phen have the same average distance while the oxygens in Mn(4,4) Phen have the same average distance as just the Mn(IV) atoms in Mn(3,4)Bipy. The Mn-Mn distances for Mn(3,4)Bipy and Mn(4,4)Phen are the same while the Mn(3,4)Phen Mn-Mn distance is 0.02Å shorter. These results thus predict changes in the Mn_1-O-Mn_2 bond angles. Using the average distances from Table 2 and assuming the same ligand distance difference as in Figure 2, the Mn_1-O-Mn_2 angles would be 1) 96.5° for Mn(3,4)Bipy (from the crystal structure[11]), 2) 93.9° for Mn(3,4)Phen, and 3) 97.7° for Mn(4,4)Phen. These are obviously not very large angular changes and, therefore, seem to be quite reasonable

results considering the similarity of the compounds. Should the crystal structures of Mn(3,4)Phen and Mn(4,4)Phen be obtained in the future, they will provide very good additional tests of the ability of EXAFS to measure small differences in structurally similar systems.

As mentioned earlier, an explanation for the problem of the missing nitrogen shells in Mn(3,4)Bipy, Mn(3,4)Phen, and Mn(4,4)Phen was developed by examining different simulations of the first coordination sphere of Mn(3,4)Bipy. The simulations were constructed by using the T-L model values with two oxygen atoms at 1.8 Å, two nitrogen atoms at 2.0Å, and two nitrogen atoms at 2.2Å The values of σ_i (see equation 3) were then varied to model variable amounts of static and thermal disorder. The simulations had two surprising results. First, if the σ_i's were equivalent and small, the result was one nitrogen transform peak, not two as expected, and it was not twice as large as the oxygen peak. One example of this result is given in Figures 1(i) and 1(j) with its numerical analysis tabulated in Table 1. This implies that the nitrogen shells were strongly interfering and while perturbing the oxygen shell transform peak, the strongest effect was upon their own transform peak. Second, if the σ_i's for the nitrogen atoms were significantly more negative than for the oxygen peak (example: σ_N = -.005 and σ_O = -.001), then the nitrogen atoms badly interfere, resulting in a very small transform peak which would be masked in the model compound transforms by the presence of the Mn peak and a finite noise level. The crystal structure of Mn(3,4)Bipy (Figure 2) shows that the nitrogen atoms are significantly more

disordered than are the oxygen atoms[11] so the disappearance of the nitrogen transform peak is not an unphysical result.[20]

A final question which requires consideration concerns the validity the di-μ-oxo manganese dimers as general model compounds for CNO bridged transition metal dimers, since their analyses are cornerstones in the analysis of the active chloroplast "loosely bound pool" of Mn. An extreme change that could be made would be to reduce the Mn atoms[6] and substitute carbon, a much "softer" ligand, for the nitrogen and bridging oxygen ligands. A number of Mn(II) dimer systems with all carbon ligands have been synthesized and studied by Anderson and coworkers.[22] The results are a 2.72Å Mn-Mn distance, a distance between the Mn atoms and bridging carbon ligands of approximately 1.8Å, the same structure as the bridged dimers studied in this paper. Thus, Anderson's compounds and the model systems examined here, which span a large range of Mn oxidation states and two different ligand systems, are suggestive that the bridged Mn dimer structure is essentially the same irrespective of the Mn oxidation states and the CNO first coordination sphere ligands. Therefore, using the di-μ-oxo dimers as general model compounds seems adequately justified.

Chloroplasts. The chloroplast samples were very dilute in Mn so the resulting XAS spectra were very noisy. Due to the methods of EXAFS analysis this noise level is greatly enhanced at the higher photon energies (higher k-values) where the majority of the multiple distance interference effects would be expected to occur. This makes the analysis difficult and the results less exact for transform peaks

which have a very significant part of their k-space data at the higher k-values, e.g., the first two peaks of the transforms for active chloroplasts (Figure 4) and the second and third peaks for the inactive chloroplasts. The second factor which must be taken into account is the high probability of a significant heterogeneity in "equivalent" local environments present in the model compounds. These two factors result in an assignment of fairly large errors for interatomic distances and only approximate values for the number of backscatters. Thus the approximate distances and the ratios for the number of backscatters is the primary interest as opposed to absolute fitting values.

(a) "Active" Chloroplasts. As mentioned earlier, the key to the identification of the first two peaks in the active chloroplasts' power spectrum was a recognition of the similarity between the $k^n\chi(k)$ Fourier transforms of the active chloroplasts and the $k^n\chi(k)$ transforms of some of the simulations of the first two peaks of Mn(3,4)Bipy such as in Figure 1(i) and 1(j). This observation led to comparing their EXAFS spectra, which were quite similar and subsequently, to performing the T-L fits that are presented in Table 3.

Comparisons of the one shell fits in Table 3 show a completely equivalent behavior with regard to all the fitting parameters (i.e. large positive σ_i's, equivalent changes in distance and E_o, and proportional changes in number of atoms). The second transform peak in either sample produces a strong destructive interference. As k increases, the EXAFS contribution of the second peak rapidly decreases and the EXAFS corresponding to the first peak reappears. The net

result of this interference produces a sine wave with frequency corresponding to the distance of the first peak and an amplitude increasing with k (Figure 4). Thus, a T-L model CNO single shell fit compensates for the k dependence of this amplitude function by invoking a large positive disorder parameter (σ_i). This produces a good fit at high k values and a very poor fit at lower k-values.

The two shell T-L fits again show strikingly similar results between the chloroplasts and the simulations. As in the one shell fits above, the fitting results arise from having to fit a larger number of real distances with a smaller number of shells. At the present time, as explained in Reference 18(a), fitting more than one shell to one transform peak is unreliable due to a surfeit of fitting parameters. Thus, when three shell fits were attempted on the isolated first two peaks of the active chloroplasts, the result was nonsense, while the fits to the simulations were perfect as expected.

Therefore, just looking at the comparison T-L fits in Table 3, the first peak would be predicted to be CNO with an approximate distance of 1.82Å. The second peak would be CNO with approximately twice the number of atoms of the first peak and results from more than one distinct distance with a net average of approximately 2.15Å.

The fitting results for all three peaks are tabulated in Table 4 and the noise-filtered $k^3\chi(k)$ spectrum and its best three shell T-L fit is presented in Figure 5. Comparison of the results of the two shell T-L fits on the isolated first two peaks (Table 3) and the oxygen and nitrogen shells of the three shell O-N-Mn T-L fit (Table 4) shows a discrepancy while the N-O-Mn three shell T-L fit (Table 4)

agreed with the two shell isolation fitting results (Table 3). Noting that there is little or no visual difference between the two-three shell fits, additional fits were performed with tight constraints on the allowable distances each of the different shells could have. Examining the additional fits shows that the O-N-Mn three shell fit has a local minimum which is equivalent to the two shell fit results of Table 3 and the N-O-Mn fit of Table 4, but there is an interaction between the three shells of the O-N-Mn parameters to produce a slightly better fit, also tabulated in Table 4. This better fit is primarily a compensation by the O-N fitting pair for the T-L model's inability to fit the MnFe shell (third peak) perfectly. It should be noted that additional N-O-Mn fits using starting values similar to the O-N-Mn fit returned to the tabulated result. Thus, this different result is primarily due to the noise level in the original spectrum and a special feature of the choice of the O-N pair, i.e., a model effect. This variable result indicates the range of results which can be obtained when working with disordered systems and having to fit a multicomponent shell with only two model shells. The important three shell results to note are the approximate 2 to 1 ratio for the first CNO shell ligands and the MnFe shell with the distances compatible with the prediction of a bridged structure. The second peak ligands are then the disordered set described above with an average distance of approxiamtely 2.15Å.

(b) "Inactive Chloroplasts. The fitting results on the inactive chloroplast spectrum are discussed in the Results section, and presented in Table 5. The spectrum is noisier than that of the active

chloroplasts and the fitting results are less satisfactory but some general conclusions can be drawn about the residual Mn in chloroplasts. First, there may well be more than one site, thus the EXAFS spectrum can be the sum of more than one signal. This can result in very confusing fitting results with only a few model shells as explained previously. Second, the overlap of the second and third power spectrum peaks and the proportionally larger contribution to these peaks from the high k-values have combined to make accurate element identification of these shells impossible. However, a tentative analysis suggests that 1) the first coordination sphere is composed of CNO ligands with an average distance of 2.1(1)Å (a reasonable result for a low valent Mn^{+2}); 2) the second coordination sphere is composed of CNO ligands at an average distance of 3.1(1)Å; and 3) some MnFe ligand at a distance of 2.7(1)Å. The MnFe ligand does not seem to be bridged, even though it is at a bridged distance. This suggests that it may result from bridged dimers which have been broken during the Tris treatment but for some reason were not removed during the osmotic shock treatment. To fully resolve the tentative nature of these results, significantly better data are required.

(c) Difference Spectrum. As described earlier, the difference spectrum, Figure 6, was created by subtracting from the active chloroplast spectrum the inactive chloroplast spectrum multiplied by one-third. The Fourier transforms are presented in Figure 1(e) and 1(f) and the curve fits noise than the active chloroplast spectrum (as

evidenced by the larger least squares fitting errors) but the results are compatible with all the results described above.

The important changes to note between the active chloroplasts and the difference spectrum are 1) the significant decrease in the second peak in the difference spectrum, and 2) the increase in the ratio of the bridging ligands to MnFe ligands from 2 to 1 in the active chloroplasts to 3 to 1 in the difference spectrum.

The decrease in the amplitude of the second peak in the difference Fourier transform is that expected if the second peak of the active chloroplasts arises from more than one Mn site containing a CNO ligand with an approximate distance of 2.1Å. The shortening of the fitted distance tends to suggest that the remaining ligands in the second peak have a little shorter average distance than indicated by the active chloroplast results. It should also be noted that it is possible that the remaining ligands comprising the second peak may not be due to bridged Mn atoms but are due to other Mn atoms that are also released during inactivation. If this is the case, then it will be necessary to study the photosynthetically active Mn in its native environment free of contamination of other Mn atoms that may be present and serve other functions. The possibility of multiple sites would also explain the low absolute number of atoms predicted by the fitting results, but at the present time this should be treated as conjecture until some new evidence indicates otherwise.

The change in the ligand ratio is most likely due to the poorer quality of the difference data, but should not be totally discounted when interpreting results.

CONCLUSION

Three di-μ-oxo Mn dimers were examined using the EXAFS technique. The crystal structure of one of the dimers has been published.[11] Using this published crystal structure, determinations were made concerning certain of the structural parameters for the other two compounds. These results were presented in part (a) of the Discussion section above.

Part of the study of the Mn dimers was concerned with determining why the nitrogen atoms in the first coordination sphere of the dimers did not appear in the EXAFS spectra. A simulation study showed that large disorder in the Mn-N distances was responsible. This simulation study then led to identification of the first two peaks of the active chloroplast Fourier transforms (see Figure 1).

EXAFS studies on the two chloroplast samples and comparison of the chloroplast results with the bridged Mn dimer models has resulted in a prediction for the local structure of the "loosely bound pool" of Mn in chloroplasts which is implicitly related to photosynthetic oxygen evolution. The analysis is compatible with a CNO bridged transition metal dimer (or multimer) similar to the core of the Mn dimer models studied. The chemistry of Mn suggests that oxygen is the most likely bridging ligand but carbon and nitrogen cannot be excluded. The partner transition metal is most likely another Mn, but Fe and Cu cannot be excluded, they are relatively abundant in chloroplasts. The remainder of the first coordination ligands is most likely CNO. The distances for the bridging ligands and the other transition metal ligands are quite accurately predicted, but the

distance for the other first coordination sphere ligands is poorly defined primarily due to a large spread in the individual ligand distances (see Table 7).

FUTURE WORK

Obvious extensions now in progress are the effects of actinic light, the effect of various redox reagents and known cofactors such as Cl^-. Most important will be the results obtained from a study of the Mn-containing protein whose isolation has been only recently reported by Spector and Wignet.[24]

Table 1

Fourier Transform (Power Spectra)
Peak Positions and Relative Amplitudes
(E_0 = 6565 eV)

Sample (k-space domain)	Peak	$k^0\chi(k)$[a] Effective Distance (Å)	$k^0\chi(k)$[a] Relative Amplitude	$k^3\chi(k)$[a] Effective Distance (Å)	$k^3\chi(k)$[a] Relative Amplitude
Mn(3,4)Bipy	Oxygen	1.06	1.00	1.37	1.00
(2.5-13.5 Å^{-1})	Manganese	1.96	0.53	2.26	0.82
Active	First	1.18	0.48	1.32	0.28
Chloroplasts	Second	1.79	0.47	1.68	0.32
(2.5-12 Å^{-1})	Third	-[c]	-[c]	2.30	0.42
Inactive	First	1.56	1.03	1.57	0.62
Chloroplasts	Second	-[c]	-[c]	2.19	0.39
(2.5-12 Å^{-1})	Third	2.53	0.15	2.64	0.31
Chloroplast[b]	First	1.26	0.66	1.31	0.36
Difference	Second	1.81	0.42	1.78	0.17
(2.5-12 Å^{-1})	Third	-[c]	-[c]	2.29	0.32
Simulated[d]	Oxygen	1.20	1.10	1.29	0.54
Mn(3,4)Bipy	Nitrogen	1.68	0.97	1.68	0.63
First Shell (2.5-13.5 Å^{-1})					

Table 1

Continued

Fourier Transform (Power Spectra)
Peak Positions and Relative Amplitudes
(E_0 = 6565 eV)

---

[a] The EXAFS data were multiplied by $k^0 = 1$ and k^3 respectively before Fourier transformation.

[b] The EXAFS data were created by Active - 1/3 Inactive. See text.

[c] Missing in this Fourier transform. Due to interference effects and noise in the data. Refer to Figure 1 (a).

[d] First shell simulation constructed by using 2 O atoms at 1.8Å, 2 N at 2.0Å and 2 N at 2.2Å with σ = -.001 for all and the Teo-Lee Model.[9] Amplitude corrected for σ.[18]

Table 2

One Shell Fits to Isolated Peaks
in Mn(3,4)Bipy[a], Mn(3,4)Phen[b] and Mn(4,4)Phen[c]
(All Fits Were Performed Over a Range of k = 4-12$\AA^{-1}$)

		Teo-Lee Model			
Sample	Fitting Error	Distance[d]	No. Atoms[e]	σ	Eo
Mn(3,4)Bipy					
O	.193	1.812 (19)[g]	1.8	-.0051	6575.0
Mn	.016	2.677 (16)[h]	0.9	-.0068	6548.6
Mn(3,4)Phen					
O	.400	1.811 (19)	2.0	-.0057	6575.9
Mn	.034	2.660 (21)[h]	1.2	-.0105	6544.6
Mn(4,4)Phen					
O	.105	1.778 (16)[g]	1.9	-.0010	6566.1
Mn	.014	2.678 (8)[h]	1.0	-.0069	6546.5

Table 2

Continued

One Shell Fits to Isolated Peaks
in Mn(3,4)Bipy[a], Mn(3,4)Phen[b] and Mn(4,4)Phen[c]
(All Fits Were Performed Over a Range of k = 4-12Å^{-1})

Hodgson-Doniach Model[18,20]

Sample	Fitting Error	Distance	No. of Atoms	Eo
Mn(3,4)Bipy				
0	.480	1.790	5.1	6565
Mn	stnd[f]	2.684[f]	1.0	6565
Mn(3,4)Phen				
0	.650	1.786	6.0	6565
Mn	.060	2.675	1.2	6565
Mn(4,4)Phen				
0	.038	1.786	4.7	6565
Mn	.016	2.686	1.0	6565

[a] di-μ-oxo-tetrakis(2,2' bipyridine) dimanganese(III,IV) perchlorate

[b] di-μ-oxo-tetrakis(1,10 phenanthroline) dimanganese(III,IV) perchlorate

[c] di-μ-oxo-tetrakis(1,10 phenanthroline) dimanganese(IV,IV) perchlorate

[d] Phase only fits, amplitude removed from Fourier isolated peak[18]

[e] Corrected for σ

[f] This Mn was used as the backscattering model with the distance correct for Mn_4N

Table 2
Continued

One Shell Fits to Isolated Peaks
in Mn(3,4)Bipy[a], Mn(3,4)Phen[b] and Mn(4,4)Phen[c]
(All Fits Were Performed Over a Range of k = 4-12Å^{-1})

[g] Mn(3,4)Bipy average distance = 1.819Å. Mn(IV)-O distance = 1.784Å.[11]

[h] Mn(3,4)Bipy Mn-Mn distance = 2.716Å. This distance error of -.039Å is characteristic of all di-μ-oxo Mn-Mn distances studied (these compounds and Mn_2O_3).[18] Thus Mn(3,4) Phen Mn-Mn = 2.707Å and Mn(4,4)Phen Mn-Mn = 2.717Å.

[i] Average least square error weighted by k^3.

Table 3

Fits on Active Chloroplast Isolations of First and Second Shells and Simulated O-N Shell of Mn(3,4)Bipy[a] Using Teo-Lee Model.[d] (All fits were performed over a range of k = 4-11 $Å^{-1}$)

Sample	Fitting Atom	Fitting Error	Distance	No.[b] Atoms	σ	ΔE_o[c]
	(a) One Shell Fits					
Active (1-2)	1) C	.043	1.830 (48)	1.1	+.0105	-17.7
	2) N	.049	1.816 (50)	0.8	+.0116	-14.0
	3) O	.050	1.802 (52)	0.6	+.0127	-10.3
Simulation	1) C	.030	1.813 (80)	1.8	+.0097	-18.0
	2) N	.031	1.800 (80)	1.3	+.0105	-14.0
	3) O	.032	1.786 (80)	1.1	+.0113	-10.3
	(b) Two Shell Fits					
Active (1-2)	1) O	.0011	1.791	0.9	+.0068	-8.9
	N		2.193	0.4[b]	-.0104	-3.0
	2) N	.0012	1.798	0.8	+.0081	-19.4
	O		2.193	0.4	-.0027	1.1
Simulation	1) O	.0002	1.803	1.6	+.0006	-3.9
	N		2.135	1.0[b]	-.0101	5.3
	2) N	.0014	1.802	1.7	+.0020	-12.6
	O		2.143	1.7	-.0037	12.6

Table 3

Continued

Fits on Active Chloroplast Isolations of First and Second Shells and Simulated O-N Shell of Mn(3,4)Bipy[a] Using Teo-Lee Model[d] (δ^{-1}) (All Fits Were Performed Over a Range of k = 4-11Å^{-1})

---

[a] Simulation parameters: 2 atoms of O at 1.80Å, 2 atoms of N at 2.00Å, 2 atoms of N at 2.20Å, all σ_i equal to -.001. Amplitudes corrected for σ.[18]

[b] Corrected for σ. σ <-.008 for CNO left uncorrected.[18]

[c] For active chloroplasts, difference between best fit E_o and 6571.2 eV. For simulated file this is the best fit ΔE_o.

[d] See reference 9.

Table 4

Active Chloroplast Three Shell Fits

(All fits were performed over a range of k = 4-11 $\mathring{A}^{-1}$)

Teo-Lee Model[9]

	Fitting Atoms	Fitting Error	Distance	No. Atoms[a]	σ	E_0
1)	O	.0013	1.851	1.4[b]	-.0073	6569.3
	N		2.046	3.3	-.0195	6549.1
	Mn		2.703	0.44	-.0049	6553.4
2)	N	.0036	1.789	1.0	+.0065	6549.2
	O		2.207	0.6	+.0144	6582.0
	Mn		2.688	0.45	-.0040	6550.7

Hodgson-Doniach Model[18,20]

	Fitting Atoms	Fitting Error	Distance	No. Atoms	E_0 = 6565 eV
1)	O	.0460	1.843	2.72	
	N		2.133	1.38	
	Mn		2.690	0.55	
2)	N	.0490	1.871	1.21	
	O		2.135	3.41	
	Mn		2.686	0.55	

a) Corrected for σ.[18]

b) σ < -.008 for CNO left uncorrected.[18]

Table 5

Inactive Chloroplast Fits Using One Shell

(All fits were performed over a range of k = 4-11 $\AA^{-1}$)

Teo-Lee Model[9]

Fit No.	Fitting Atom	Fitting Error	Distance[a]	No. Atoms[b]	σ	E_0
		(a) Isolated First Peak Fits				
1)	C	.157	2.106 (44)	2.5	-.0059	6546.2
2)	N	.124	2.085 (36)	2.1	-.0048	6548.7
3)	O	.094	2.068 (31)	1.8	-.0039	6550.7
		(b) Isolated Second Peak Fits				
1)	C	.0196	2.716 (24)	3.3	+.0008	6548.2
2)	N	.0128	2.696 (18)	2.6	+.0019	6550.0
3)	O	.0079	2.677 (12)	2.1	+.0027	6551.8
4)	S	.0195	2.676 (10)	-1.2	-.0034	6551.3
5)	Mn	.0507	2.674 (8)	0.44	-.0099	6540.7

a) Phase only fits.[18]

b) Corrected for σ. For sulfur a multiple Mn amplitude correction was used.[18]

Table 6(a)

Fits on Chloroplast Difference
(All fits were performed over a range of k = 4-11 $\mathring{A}^{-1}$)

Teo-Lee Model[9]

	Fitting Atoms	Fitting Error	Distance	Number of Atoms	σ	E_0
			Two Shell Fits			
1)	O	.0344	1.791	0.99[a]	+.0035	6550.0
	Mn		2.711	0.89[c]	-.0279	6557.6
2)	N	.0410	1.806	1.24[a]	+.0025	6546.0
	Mn		2.710	0.87[c]	-.0277	6557.7
			Three Shell Fits			
1)	O	.0063	1.812	0.92[a]	+.0073	6557.4
	N		2.139	0.32[a]	-.0026	6583.0
	Mn		2.694	0.23[c]	-.0225	6554.8
2)	N	.0067	1.809	0.94[a]	+.0101	6548.0
	O		2.077	0.43[b]	-.0563	6583.0
	Mn		2.706	0.29[c]	-.0188	6556.2

a) Corrected for σ.[18]

b) σ < -.008 for CNO left uncorrected.[18]

c) σ < -.023 for single Mn shell left uncorrected.[18]
Note that in general the larger σ, the smaller the number of atoms predicted by the fit. If the slope for the Mn correction from Reference 18 is used, then all four numbers of Mn atoms above are equivalent ±10%.

Table 6(b)

Fits on Chloroplast Difference

(All fits 4-11 $\mathring{A}^{-1}$)

Hodgson-Doniach Model[18,20]

E_0 = 6565 eV

	Fitting Atoms	Fitting Error	Distance	No. Atoms
		Two Shell Fits		
1)	O	.243	1.865	0.80
	Mn		2.862	0.39
2)	N	.162	1.848	1.85
	Mn		2.678	0.39
		Three Shell Fits		
1)	O	.0054	1.854	3.10
	N		2.111	1.13
	Mn		2.677	0.39
2)	N	.0222	1.888	1.51
	O		2.130	2.85
	Mn		2.676	0.38

Table 7

Proposed Ligand Structure of the Photosynthetically Active, "Loosely Bound" Pool of Manganese in Spinach Chloroplasts

Ligand[a]	Average Distance[b]	Number
CNO[c]	1.81 (2)	2-3
CNO	2.15 (5)	2-4
MnFe[c]	2.72 (2)	1

a) CNO = Carbon, Nitrogen, or Oxygen
MnFe = Manganese or Iron or Copper

b) Average results for various fits.

c) Bridged structure with CNO ligands and MnFe ligands in approximately square or trigonal bipyrimid arrangement.

FIGURE CAPTIONS

CHAPTER IV

Figure 1. Fourier transforms (power spectra) for a number of different samples with the numerical results in Table 1. Spectra (a),(c), (e), (g), and (i) are transforms of k^0 (k). Spectra (b), (d), (f), (h), and (j) are transforms of k^3 (k). Samples are: (a), (b) Mn(3,4)Bipy; (c),(d) active chloroplasts; (e),(f) inactive chloroplasts (TRIS treated, osmotically shocked); (g),(h) Difference spectrum; and (i),(j) simulated first coordination sphere of Mn(3,4)Bipy (see Table 1 for more detail).

Figure 2. Structure of Mn(3,4)Bipy as determined by Plaksin,et al., J. Am. Chem. Soc. 94, 2121.[11] (1972).

Figure 3. Fluorescence X-ray Absorption Spectra of the Manganese K-edge for (a) "Active" Chloroplasts and (b) "Inactive" or TRIS washed osmotically shocked Chloroplasts.

Figure 4. K-space spectra (a) k^3 and best two shell Teo-Lee[9] oxygen-nitrogen fits for (a) Fourier isolation of first two Fourier transform peaks of the "Active" Chloroplasts (b) k-space simulation of first coordination sphere of Mn(3,4)Bipy. See Fig. 1 for the Fourier transforms and Table 3 for the fitting results.

FIGURE CAPTIONS, CHAPTER IV, continued

Figure 5. k-space Chloroplast Difference spectrum (Active Chloroplast spectrum - (Inactive Chloroplast spectrum/3) and the best Teo-Lee[9] three shell oxygen-nitrogen-manganese fit (see Table 6).

Figure 6. K-space Chloroplast Difference spectrum (Active" Chloroplast spectrum - (Inactive" Chloroplast spectrum/3) and the best Teo-Lee[9] three shell oxygen-nitrogen-manganese fit (see Table 6).

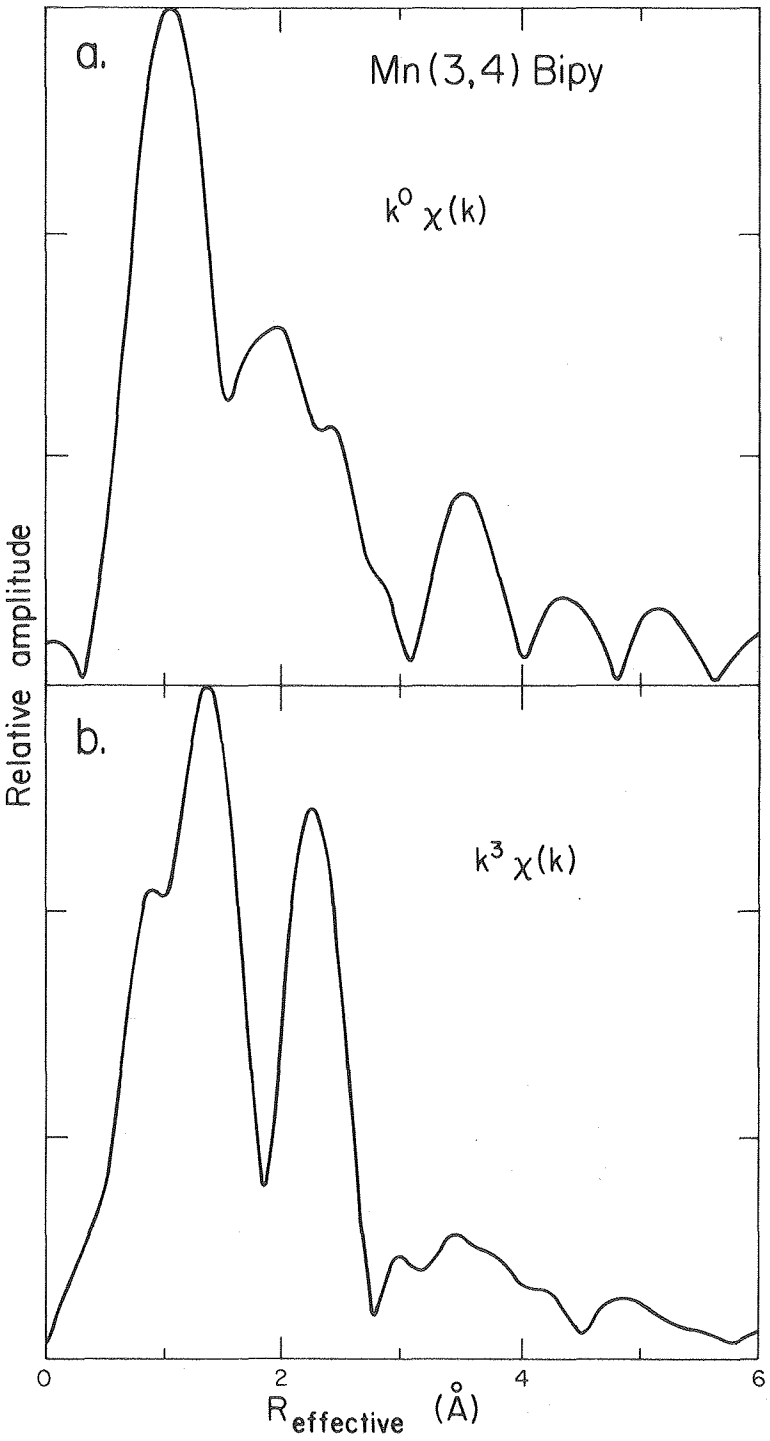

XBL 7910-5031

CHAPTER IV

Figure 1 a,b

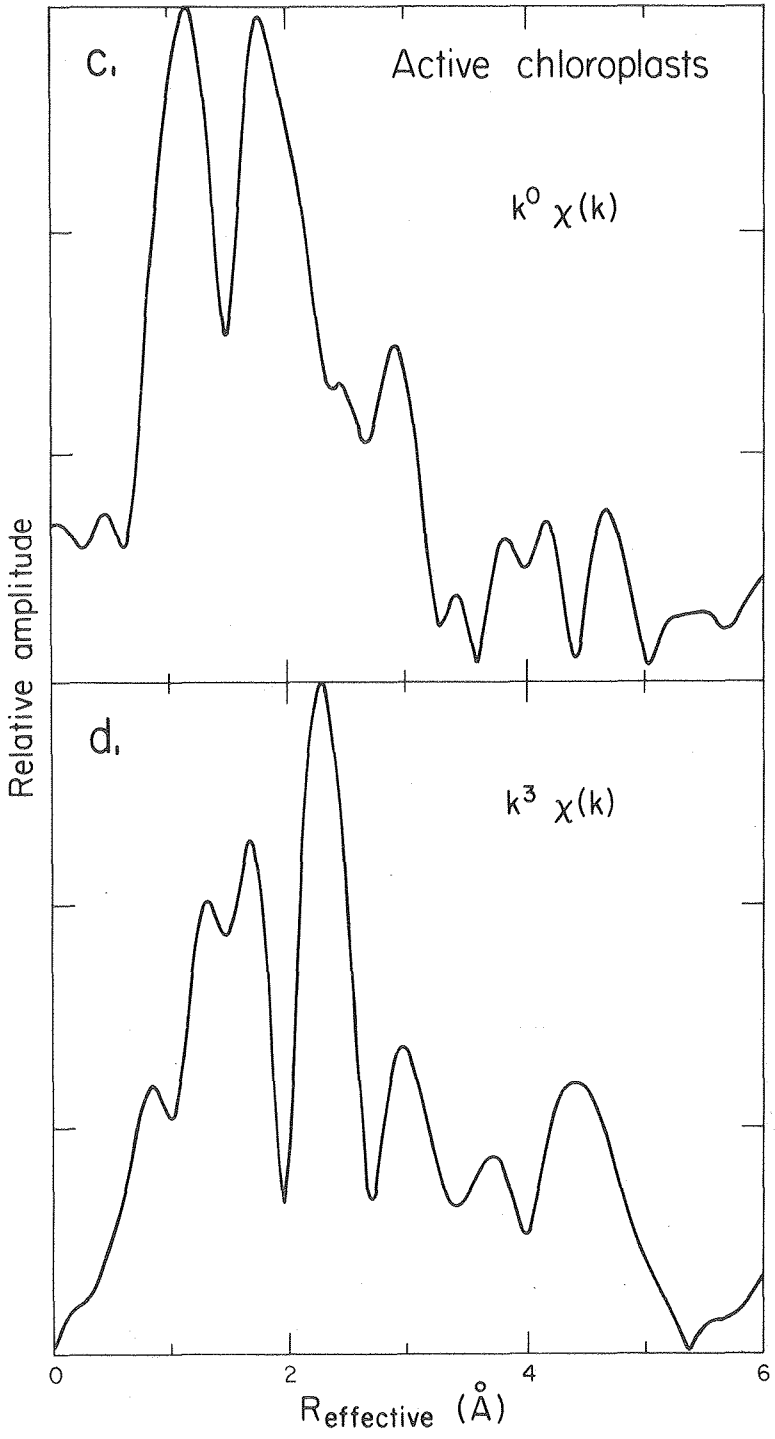

XBL 7910-5030

CHAPTER IV

Figure 1 c,d

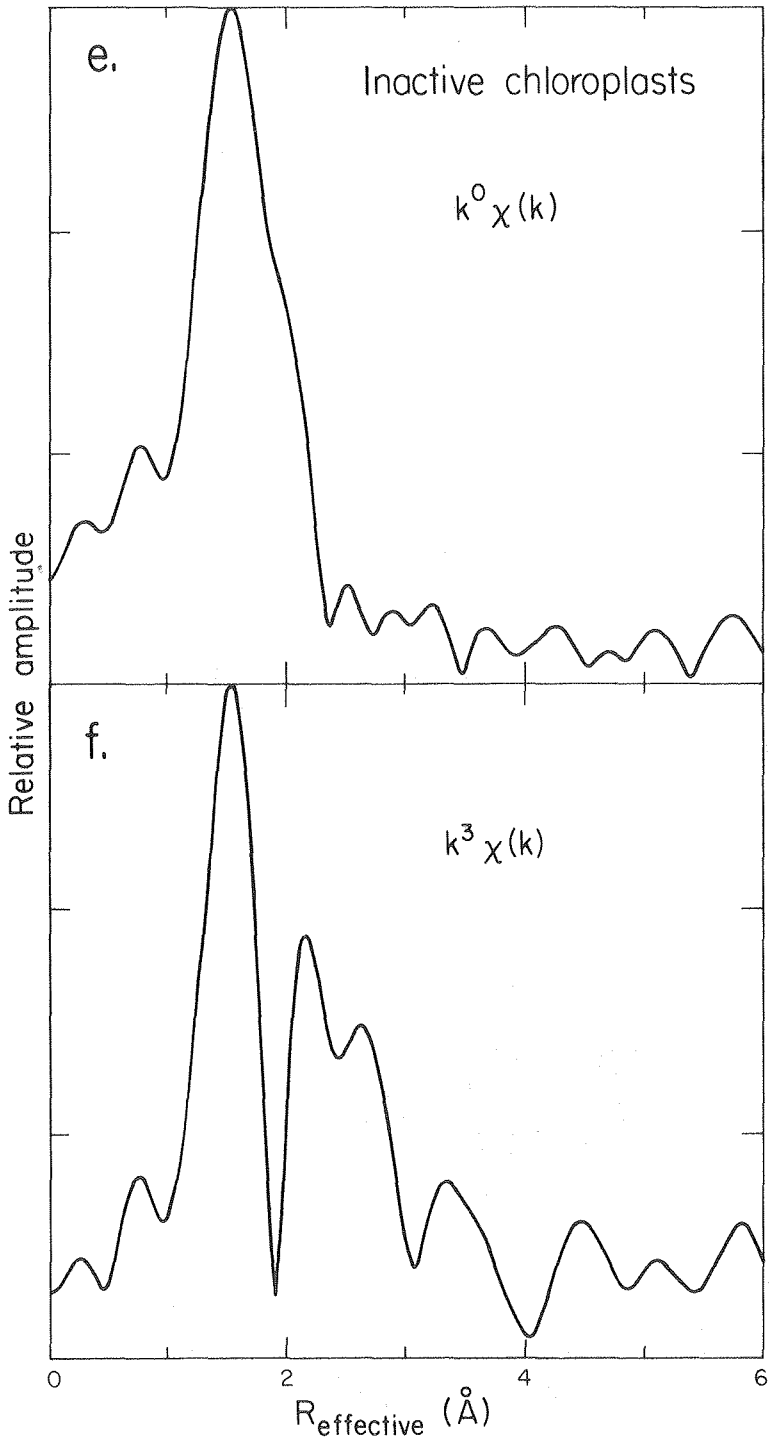

XBL 7910-5032

CHAPTER IV

Figure 1 e,f

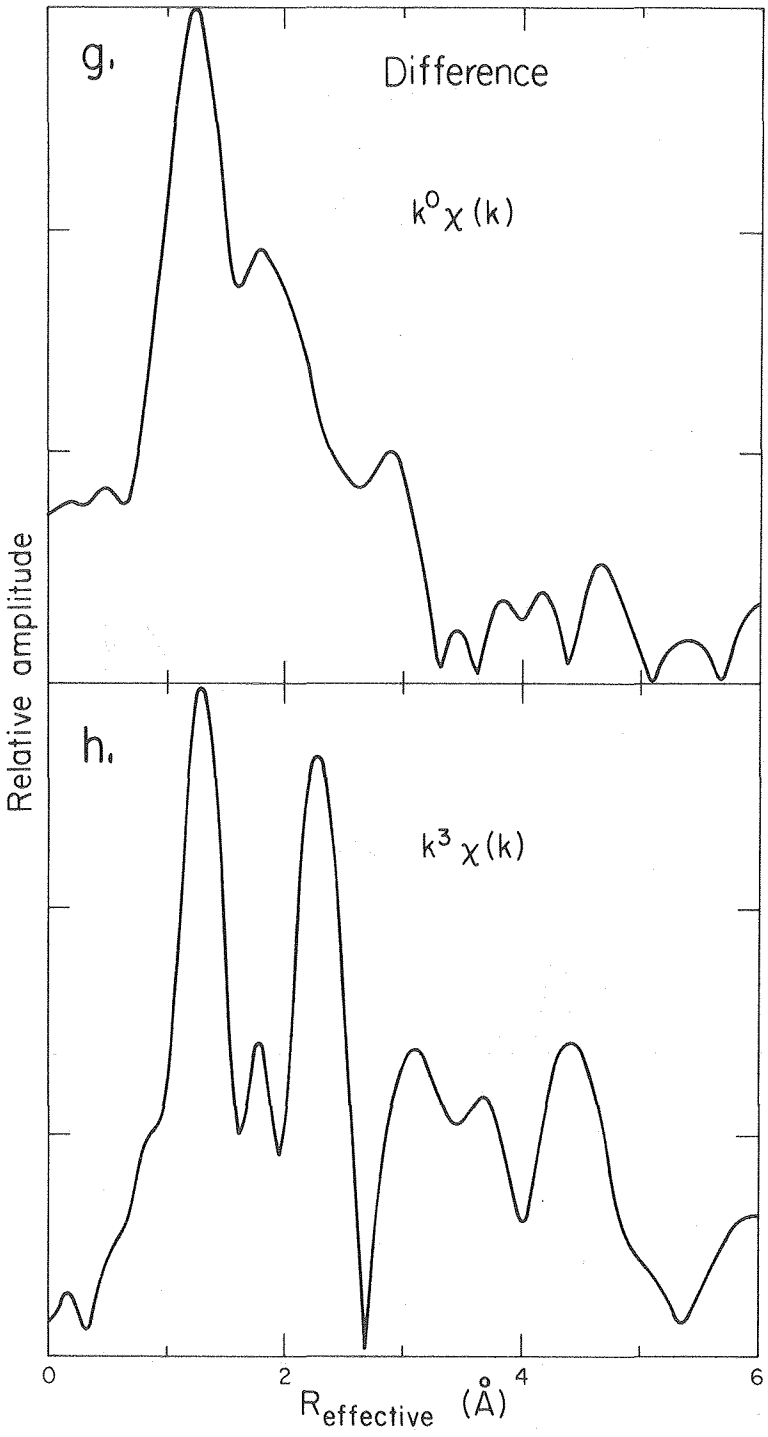

XBL 7910-5028

CHAPTER IV

Figure 1 g,h

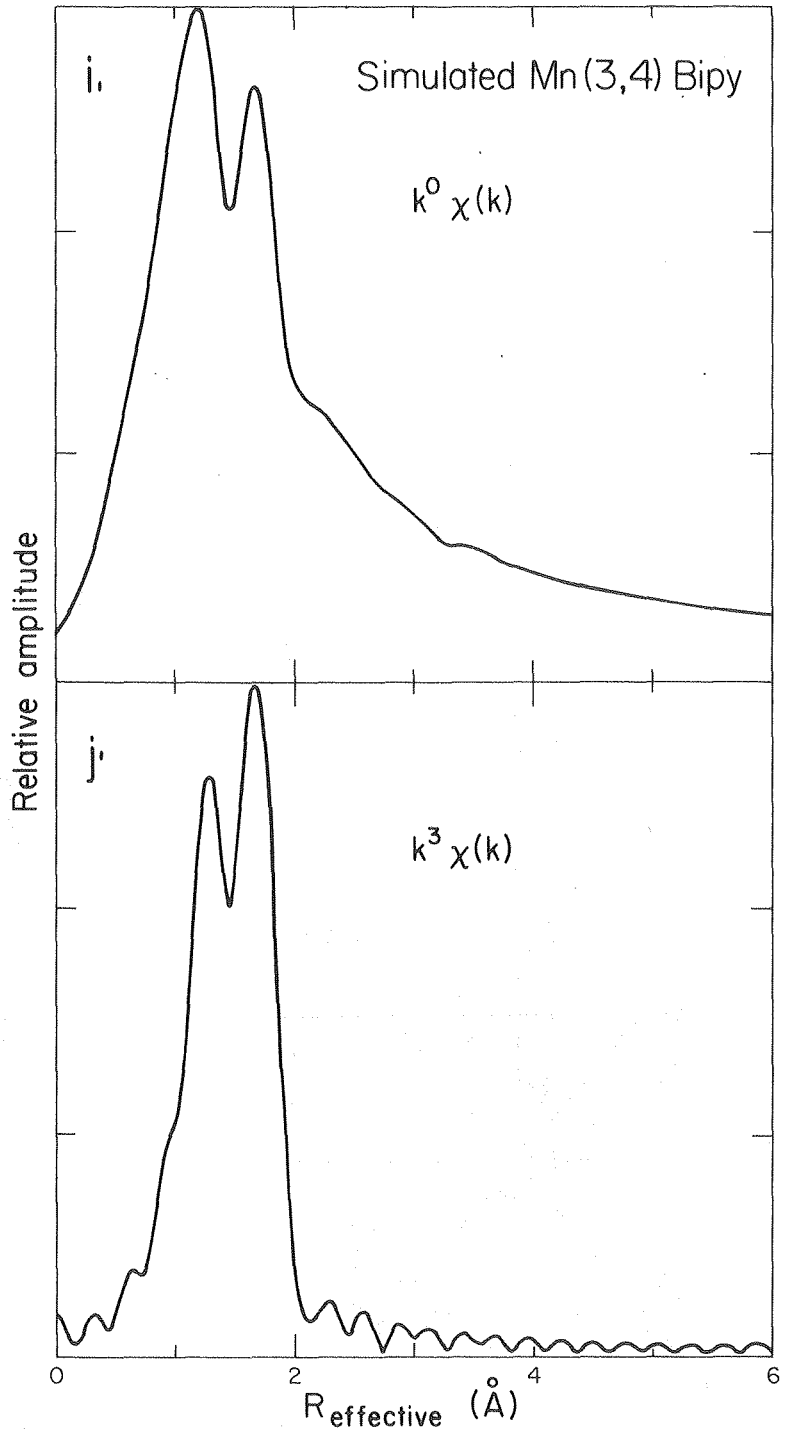

XBL 7910-5029

CHAPTER IV

Figure 1 i,j

Figure 2.

Structure of di-μ-oxo-tetrakis (2,2' bipyridine) dimanganese (III, IV) perchlorate

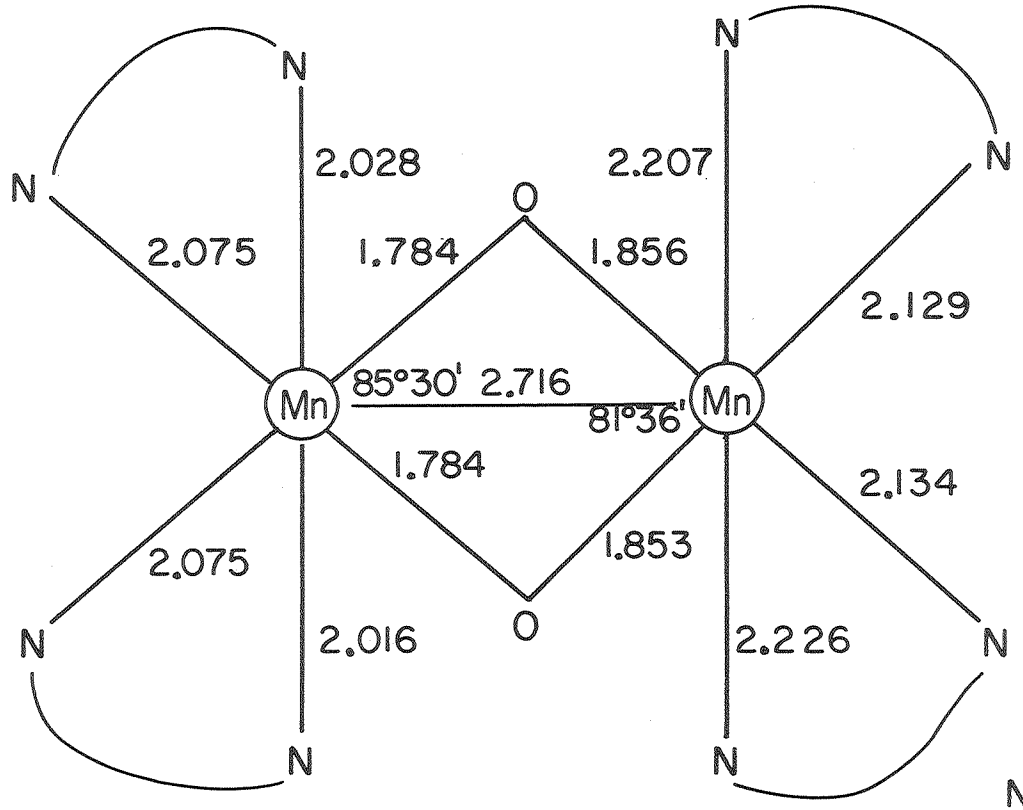

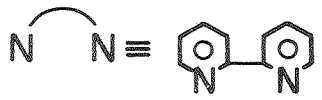

P.M. Plaksin, R.C. Stoufer, M. Mathew, G.J. Palenik, JACS 94 2121 (1972)

XBL7310-4202

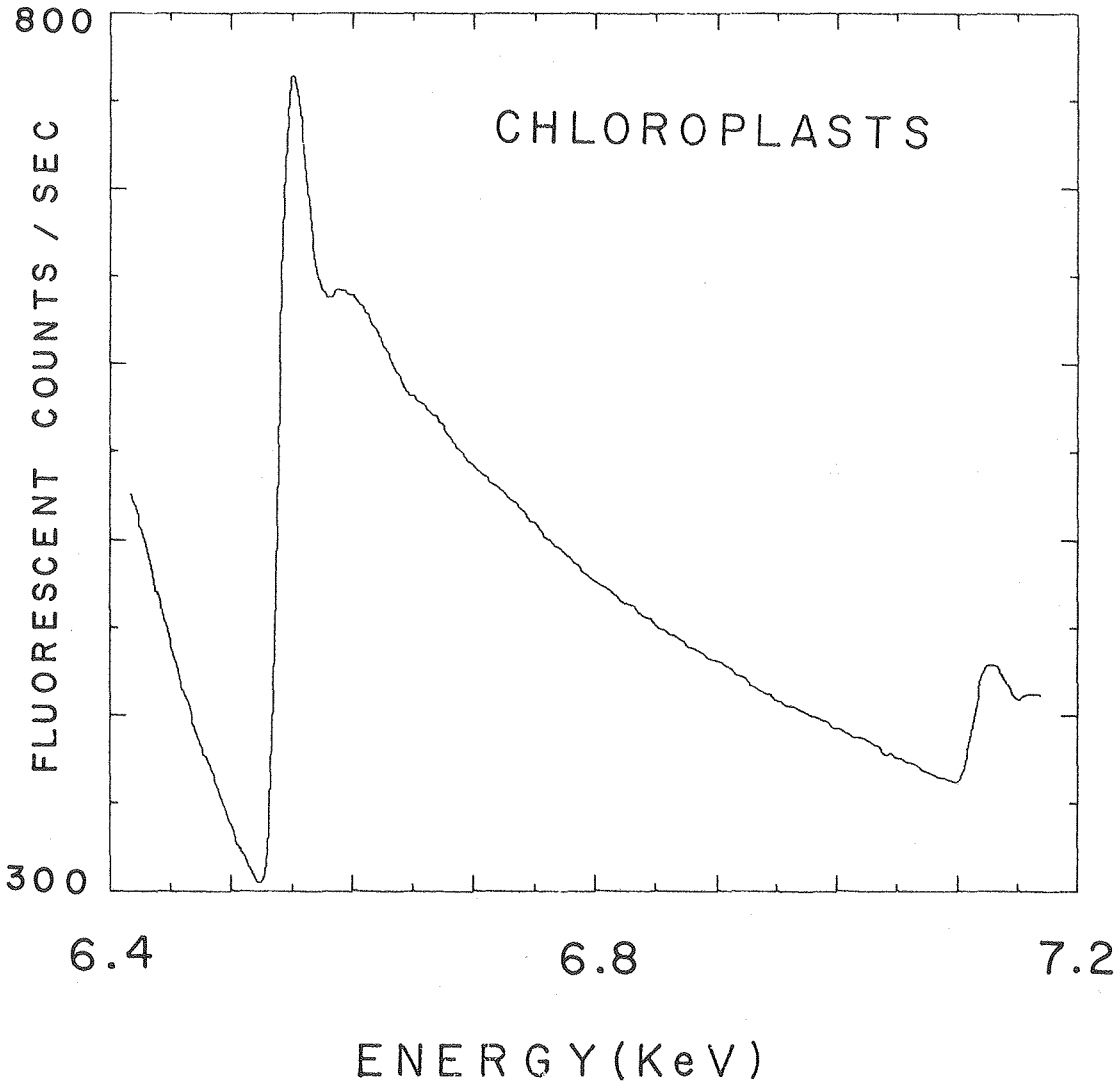

XBL 7810-4256

CHAPTER IV

Figure 3a.

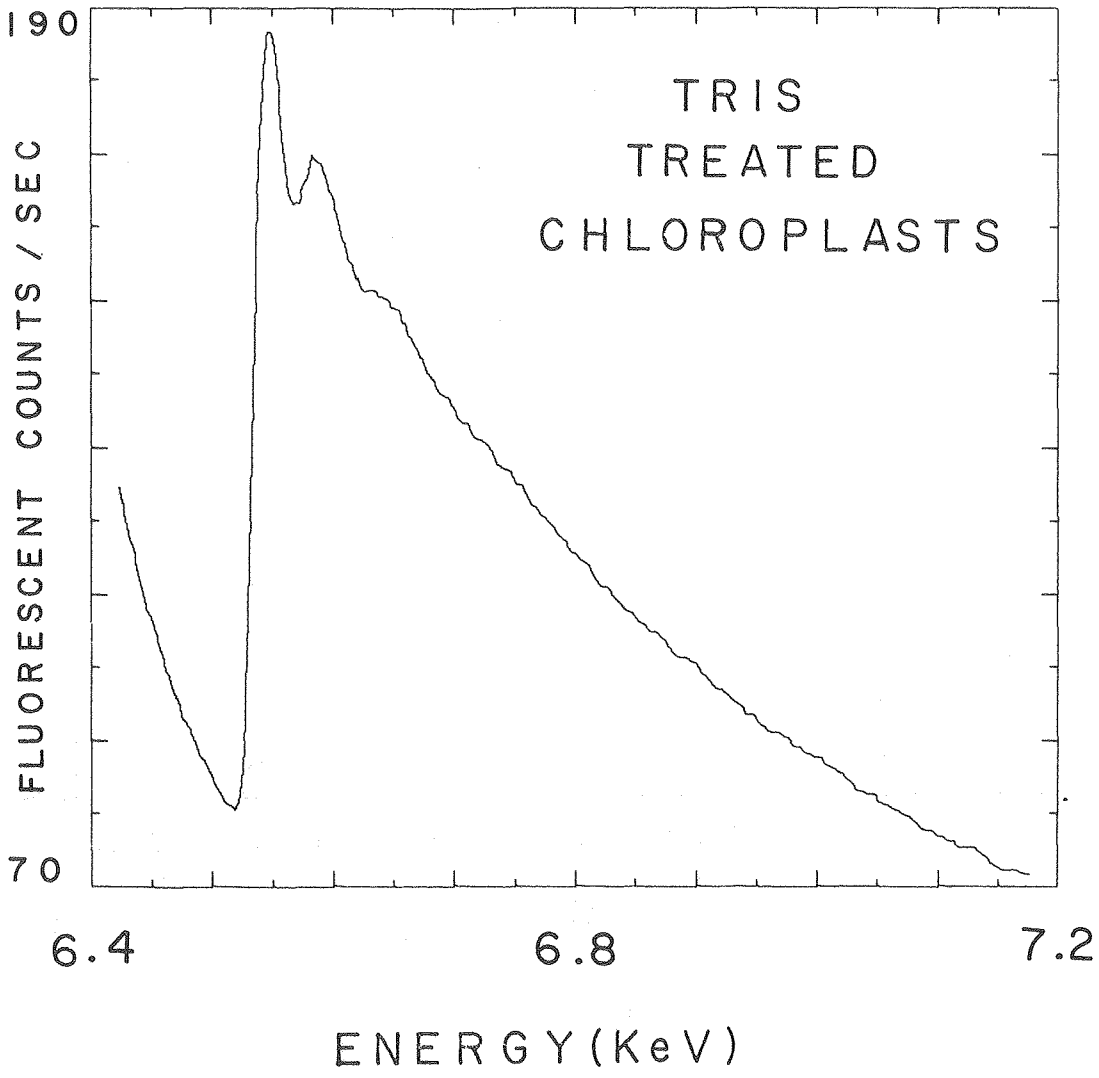

CHAPTER IV

Figure 3b.

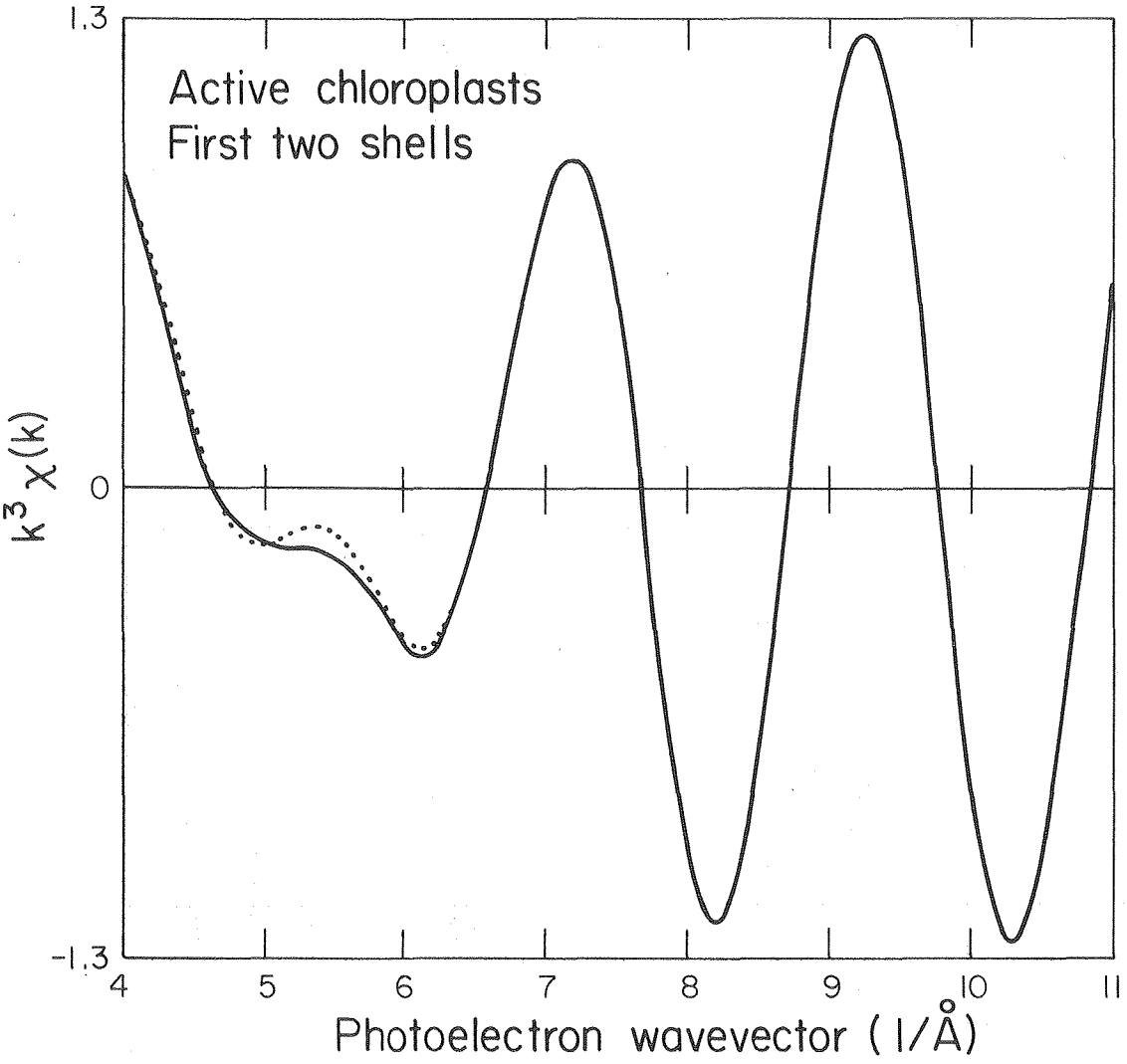

XBL 7910-5025

CHAPTER IV

Figure 4a.

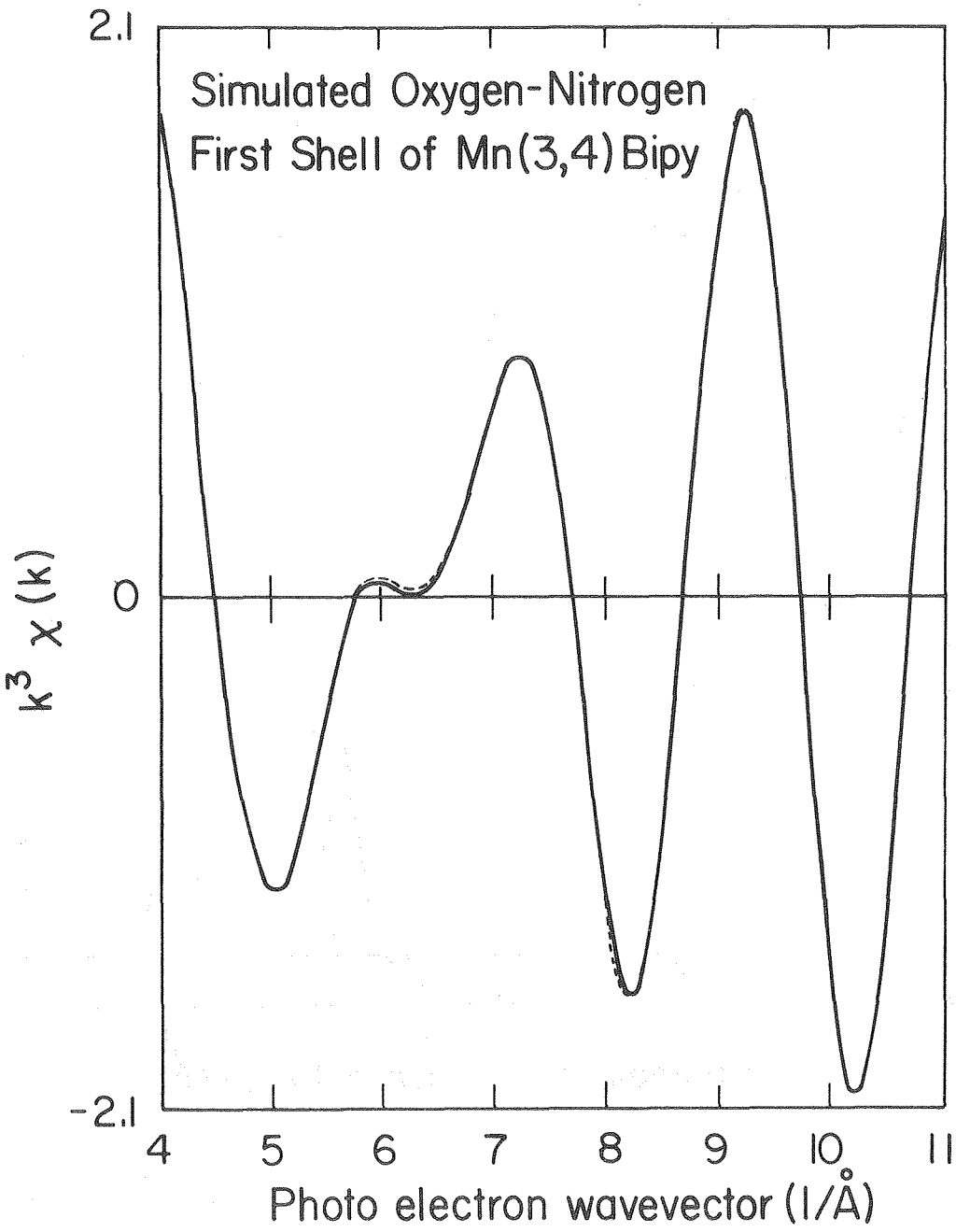

CHAPTER IV

Figure 4b.

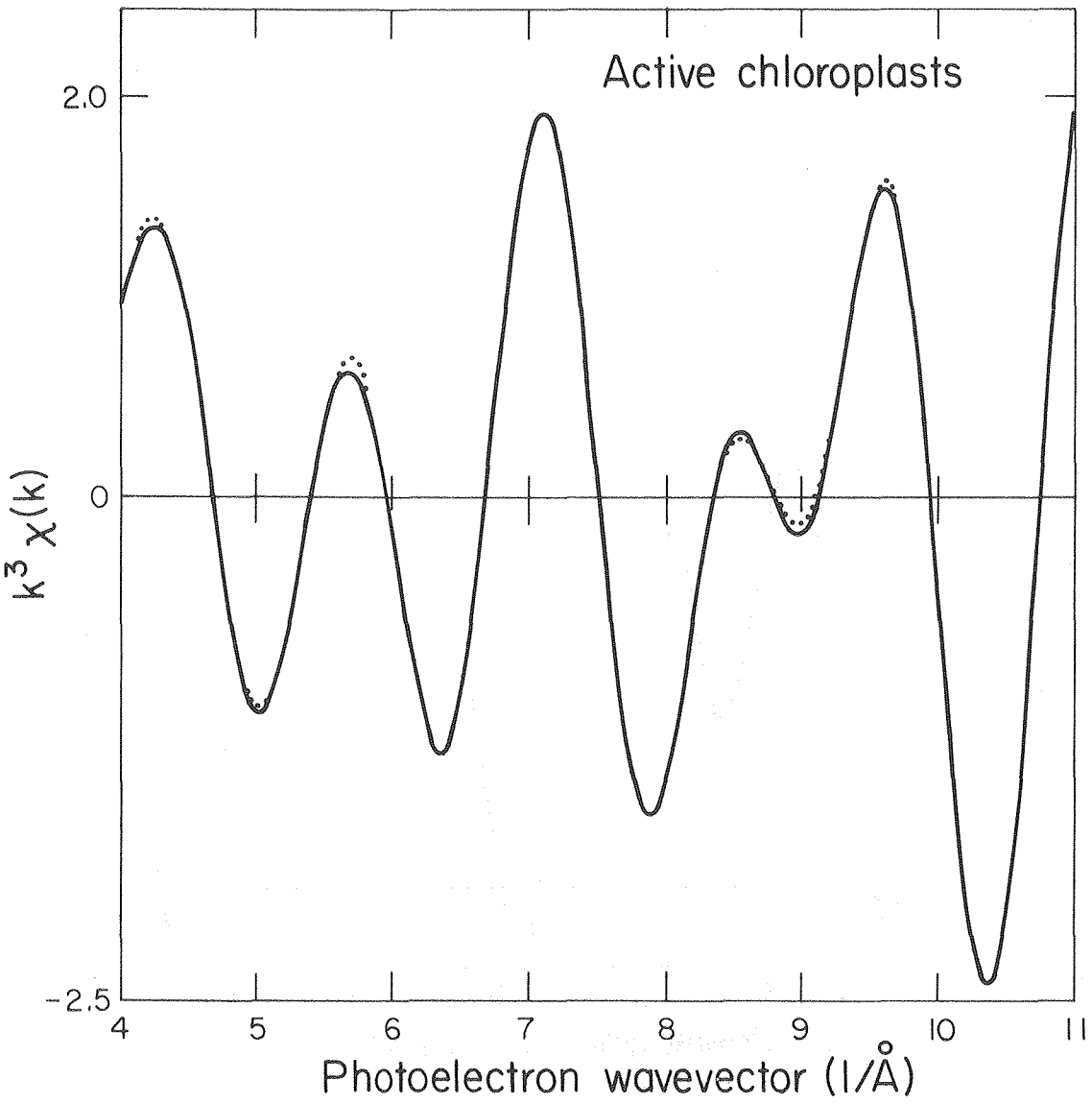

XBL 7910-5026

CHAPTER IV

Figure 5.

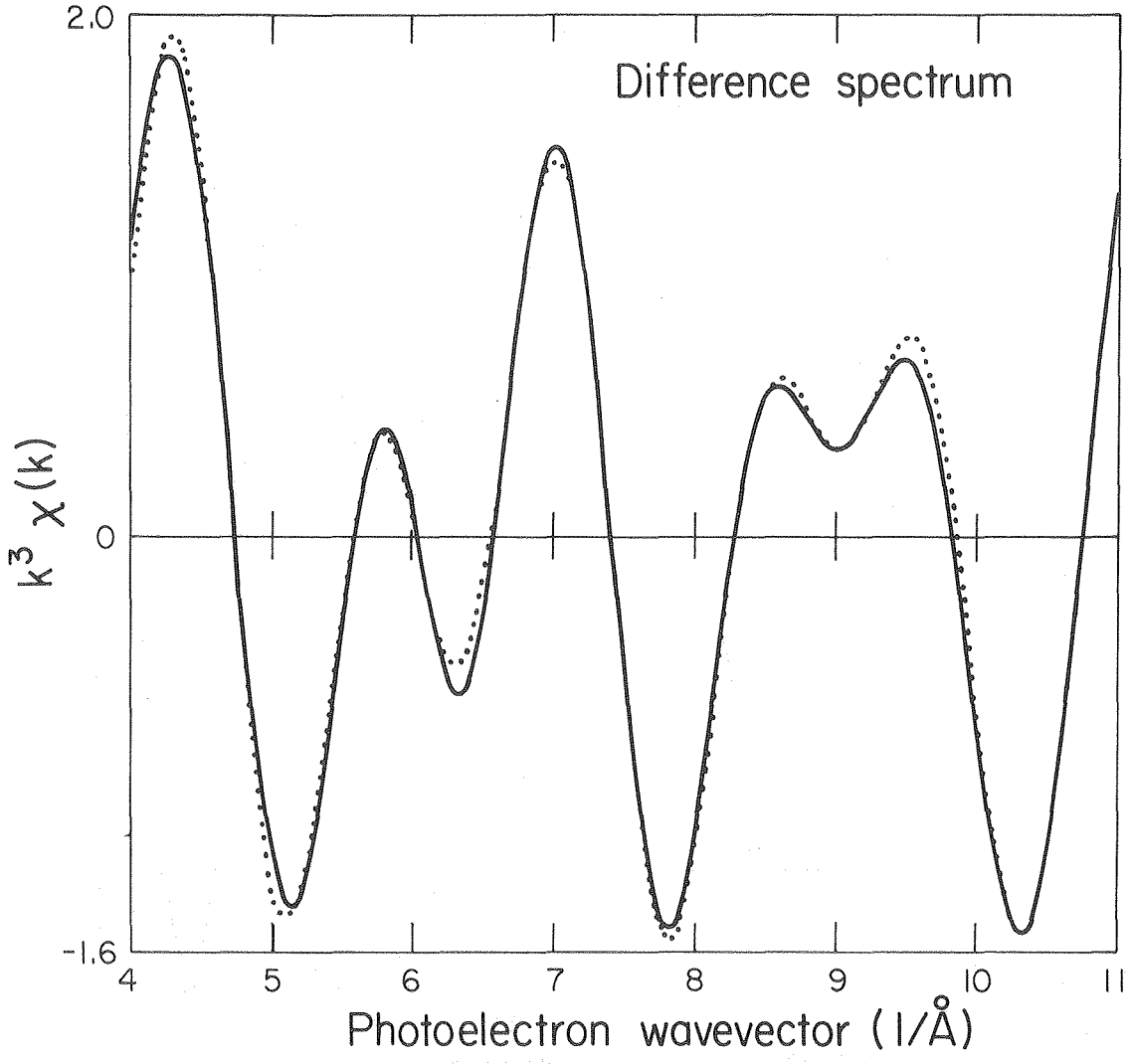

XBL 7910-5027

CHAPTER IV

Figure 6.

REFERENCES

CHAPTER IV

1. Pirson, A. Z. Botan. 31, 193-267 (1937).
2. Radmer, R.; Cheniae, G. in "Topics in Photosynthesis", Primary Processes of Photosynthesis", Vol. 2, J. Barber, Ed., Elsevier, Amsterdam, 1977, pp. 303-348.
3. Wydrzynski, T., Marks, T., Schmidt, P.G., Govindjee and Gutowsky, H.S. Biochem. 17, 2155 (1978).
4. Blankenship, R.E. and Sauer, K. Biochim. Biophys. Acta 357, 152 (1974).
5. Wydrzynski, T. and Sauer, K. Biochim. Biophys. Acta 589, 56 (1980).
6. (a) Kirby, J.A., Goodin, D., Wydrzynski, T., Robertson, A.S., and Klein, M.P. (submitted).
   (b) Chapter 5.
7. Stern, E.A. Phys. Rev. B., 10, 3027 (1974).
8. Ashley, C.A. and Doniach, S. Phys. Rev. B., 11, 1279 (1975).
9. Teo, B.-K. and Lee, P.A. J. Am. Chem. Soc. 101, 2815 (1979).
10. Cramer, S.P., Hodgson, K.O., Stiefel, E.I., and Newton, W.E. J. Am. Chem. Soc... 100, 2748 (1978).
11. Plaksin, P.M., Stoufer, R.C., Mathew, M., and Palenik, G.J. J. Am. Chem. Soc. 94, 2121 (1972).
12. Cooper, S.R. and Calvin, M. J. Am. Chem. Soc. 99, 6623 (1977).
13. Nyholm, R.S. and Turco, A. Chem. Ind. (London), p. 74 (1960).
14. Kincaid, B.M. PhD Thesis, Stanford University (1975).

REFERENCES, CHAPTER IV, continued

15. Hastings, J.B., Kincaid, B.M., and Eisenberger, P. Nuc. Inst. Methods 152, 167 16. Jaklevic, J., Kirby, J.A., Klein, M.P., Robertson, A.S., Brown, G.S., and Eisenberger, P. Sol. State Comm. 23 679-682 (1977).

17. Goulding, F.S. and Pehl, R.H. in "Nuclear Spectroscopy and Reactions, Part A" Academic Press, New York, 1974, P. 289.

18. (A) Kirby, J.A., Robertson, A.S. and Klein, M.P. (in preparation).

(B) Kirby, J.A., Ph.D. Thesis, University of California, Berkeley, (1980).

(c) Smith, J.P., Ph.D. Thesis, University of California, Berkeley (1978).

(d) Robertson, A.S., Ph.D. Thesis, University of California (1979).

19. Cramer, S.P., Eccles, T. K., Kutzler, F., Hodgson, K.O., and Doniach, S. J. Am. Chem. Soc. 98, 8059 (1976).

20. Eisenberger, P. and Brown, G.S. Solid State Comm., 29, 481 (1979).

21. (a) Cramer, S.P., Hodgson, K.O., Stiefel, E.I., and Newton, W.E. J.Am. Chem.Soc. 100, 2748 (1978).

(b) Cramer,S.P., Hodgson,K.O., Gillum, W.O., and Mortenson, L.E. J. Am. Chem. Soc. 100, 3398 (1978).

(c) Cramer, S.P., Gillum. W.O., Hodgson, K.O., Mortenson, L.E., Stiefel, E.I., Chisnell, J.R., Brill, W.J., and Shah, V.K. J. Am. Chem. Soc. 100, 3814 (1978).

REFERENCES, CHAPTER IV, continued

22. Anderson, R.A., Carmona-Guzman, E., Gibson, J.F., and Wilkinson, G. J.C.S. Dalton, 2204 (1976).

23. The "inactive" Chloroplast sample of this presentation corresponds to the Tris-treated osmoticly shocked" or "shocked" chloroplast sample of Reference 6.

24. Spector, M. and Winget, G.D. Proc. Nat. Acad. Sci. USA 77, 957 (1980)

CHAPTER V

X-RAY ABSORPTION EDGE SPECTROSCOPY (XAES) RESULTS ON MANGANESE CONTAINING COMPOUNDS AND THE MANGANESE IN PHOTOSYNTHETIC OXYGEN EVOLUTION

INTRODUCTION

The production of oxygen in photosynthesis by green plants and blue-green algae has been the subject of innumerable studies in the last 50 years. One of the results of these studies has been the demonstration of a manganese requirement for oxygen evolution (1,2,3). A membrane bound form of manganese as a necessary component of the electron transport chain has been the subject of many other studies (6,7,8,9). In addition, experiments by Kessler (4) and more recently by Cheniae and Martin (5) have placed the site of manganese sensitivity on the donor side of photosystem II near the site of water oxidation.

A currently popular scheme employing the cycling of five states, S_0 through S_4 was proposed by Kok (10) in 1970 to explain the observed oscillations in oxygen evolution (11) after each of a series of brief (10 μsec) flashes of light. The first evidence that manganese may be directly involved in the proposed "S" intermediates was provided by its effect on proton NMR relaxation rates (12) and an EPR study of Mn^{+2} released from thylakoid membranes by heat (13).

It thus appears likely that a protein bound manganese site is involved in accumulating oxidizing equivalents and/or acting as the catalytic site for photosynthetic water oxidation. Unfortunately, the crucial questions concerning the oxidation states of the membrane bound fraction of manganese and its ligand environment have been unavailableto scrutiny by conventional spectroscopic techniques.

We have undertaken a comprehensive study of manganese in spinach chloroplasts utilizing X-ray Absorption Spectroscopy, and wish to report the first direct observation of manganese bound to photosynthetic membranes. Reported here are the results of the X-ray Absorption Edge Spectroscopy (XAES) study of chloroplasts which revealed information about the oxidation state and ligand site symmetry of this previously shrouded component. Results and analysis of Extended X-ray Absorption Fine Structure were presented in Chapter IV (27).

MATERIALS AND METHODS

Model Compounds:

Samples of di-μ-oxo-tetrakis(1,10 phenanthroline)dimanganese (IV,IV)perchlorate [Mn(4,4)Phen], di-μ-oxo-tetrakis(2,2' bipyridyl)dimanganese(III,IV)perchlorate [Mn(3,4)Bipy], di-μ-oxo-tetrakis(1,10-phenanthroline)dimanganese(III,IV)perchlorate)[Mn(3,4)Phen] and μ-oxo-bis(phthalocyanatopyridine)manganese(III) dipyridinate [Mn(III)$(PcPy)_2O$] were provided by S.R. Cooper of the Dept. of Chemistry, Harvard, and were synthesized according to literature methods (28). Samples of $[(C_6H_5)_4P]_2$ Mn(II) $(SC_6H_5)_4$ were provided by D. Coucouvanis, Dept. of Chemistry, Univ. of Iowa. "Mn_2LCl_2" and "Mn_2LBr_2" were obtained from J.F. Dodge, Dept. of Chemistry, Calif. Inst. of Technology. All other manganese compounds were obtained from commercial sources.

Chloroplast preparation:

Broken spinach chloroplasts and broken chloroplasts treated with tris(hydroxymethyl)aminomethane (TRIS) were prepared as described by Blankenship and Sauer (14), except that the initial sucrose isolation medium contained 1mM EDTA to remove free and loosely bound manganese. The total chlorophyll content was determined by the method of MacKinney (15).

O_2 Evolution:

O_2 evolution was measured with a Beckman No. 39065 Clark-type electrode polarized at -0.8 V vs. Ag/Ag Cl. The media and measuring procedure were those of Blankenship and Sauer (14).

X-ray Absorption Samples:

Active chloroplast samples were made from preparations evolving no less than 150 moles O_2/mg Chl hr. Complete inhibition of oxygen evolution was verified for samples of Tris-treated chloroplasts, and release of Mn^{+2} from the vesicles was monitored with a Varian E-3 EPR spectrometer. Tris-treated, osmotically shocked samples were prepared by incubating Tris-treated chloroplasts in distilled water on ice at approximately 0.1 mg Chl/ml for 1/2 hour. All samples were centrifuged at 5000 X g for 5 minutes and the pellets were layered, to a thickness of about 2 mm, on sample holders consisting of millipore air pollution filter disks. A drop of sucrose isolation buffer (14) was applied to the samples periodically to retain moisture.

Samples of model compounds were prepared by pressing pellets of the appropriate material in a powdered cellulose matrix. The quantity used was that required to produce an absorbance change of 90% across

the K-absorption edge (21). Samples of $[(C_6H_5)_4\ P]_2$ Mn (II) $(SC_6H_5)_4$ were prepared under an argon atmosphere in a gas-tight sample cell with Kapton windows. The sample cell was stored under argon until use.

X-ray Absorption Measurements:

The XAES spectra were collected at the Stanford Synchrotron Radiation Laboratory, Stanford, CA (SSRL). The XAES spectra were collected using the standard absorption method described elsewhere (24). This consisted of a tunable monochromatic X-ray source, two ion chambers and the absorbing sample. The sample was placed between the two ion chambers which were used to obtain a measure of the incident and transmitted photon fluxes. The ratio of the incident to transmitted flux was collected as a function of incident photon energy, and the natural logarithm of this ratio was used as a measure of the total X-ray absorption cross section.

Data for the chloroplast samples were collected utilizing detection of the Mn Kα fluorescence exitation spectrum utilizing a three channel lithium drifted silicon detector (29).

Data on samples of a reference material ($KMnO_4$ or $MnCl_2 \cdot 4H_2O$) were collected for each fill of the storage ring to allow reliable energy
registration between samples and from day to day. Energy calibration of each sample studied was made by requiring a feature of the reference material to have a predetermined value ($KMnO_4$-pre-edge transition at 6543.3 eV, $MnCl_2 \cdot 4H_2O$ edge at 6546.7 eV).

The X-ray absorption edge energy was defined as the energy of the first major point of inflection on the edge. The derivative at a

point was obtained by fitting a polynomial to a fixed width energy region of the spectrum, evenly spaced on both sides of the point of interest. The polynomial was then differentiated to obtain a good approximation to the true derivative at that point. In the analysis presented here, the polynomial used was a quadratic and the energy widths were 2.5 eV and 5.0 eV for the model compounds and the chloroplast samples, respectively.

The chloroplast samples required a larger width due to a significantly higher noise level.

THEORY

It has been known for many years that the binding energies of the inner core electrons and the nuclei of atoms are affected by chemical bonding. Photoelectron (15) and Mossbauer Spectroscopy (16) are good examples of this effect. As with these methods, XAES can be used to gain information related to the oxidation state, ligand site symmetry and environment of a metal atom (17).

The features of an X-ray absorption edge are due to transitions from a core level to "bound" states in complexes or band structure statesin crystaline solids. For this study the 1s or K-shell absorption edge (K-edge) of Mn was measured.

In 1967, Batsonov and coworkers (18) reported a linear correlation between the X-ray edge position and a quantity called the "coordination charge," defined as

$$\eta = z - \sum_{i=1}^{N} C_j \qquad (1)$$

where η is the coordination charge, Z is the formal oxidation state of the absorbing atom, C_j is the degree of covalence for the jth first coordination sphere ligand and N is the total number of first sphere ligands. The degree of covalence is defined as $C_j=1 - i_j$, where i_j is the ionicity of the bond between the absorbing atom and the jth ligand. The ionicity is calculated from Pauling's formula (19), giving

$$i=1 - \exp [- (\chi_A - \chi_L)^2/4] \qquad (2)$$

where χ_A and χ_L are the electronegativities of the absorber and ligand respectively. Cramer, et al. (21) have recently used this technique with some success in a study of the coordination environment of molybdenum in nitrogenase.

RESULTS

The X-ray absorption edges, utilizing fluorescence detection, (29) were obtained for chloroplasts prepared in three conditions. The results are presented in Fig. 1. Normal, active chloroplasts (labeled X) are those possessing full oxygen evolving capabilities. These preparations are reported to have 4-6 manganese atoms per photochemical reaction center(5). This manganese does not give rise to an aqueous Mn^{+2} EPR signal (5) and is assumed to be membrane bound. Second are chloroplasts which have been treated with 0.8M Tris buffer at pH 8.0 (labeled Y) which lack O_2 evolution capacity (5). Samples prepared under these conditions have released roughly 2/3 of their manganese to the inside of the thylakoid vesicles where it appears as

hexaquated Mn^{+2} by EPR (30). The third sample consists of Tris-treated thylakoid vesicles which have been osmotically ruptured and concentrated by centrifugation (labeled Z).
This treatment allows removal of the aqueous manganese trapped on the inside of the vesicles (14). This was verified by observing the loss of hexaquated Mn^{+2} EPR signal for this sample.

For comparison the edge spectra of Mn(III) $(acetylacetonate)_3$ (labeled 11) and Mn $(H_2O)_6^{+2}$ (labeled 9) are also shown. A number of characteristics of these spectra are particularly striking. Active chloroplasts exhibit an edge which is quite similar in position and shape to Mn(III) $(acetylacetonate)_3$, yet the edge of Tris treated chloroplasts is markedly different. The edge position and shape for the latter is much more like that of $Mn(H_2O)_6^{+2}$, which exhibits a strong absorbance peak at the edge. It can also be seen that the osmotically shocked chloroplast sample exhibits an edge intermediate between these two extremes.

Absorption edges (not shown) for a variety of manganese compounds were collected for the purpose of the edge correlation analysis. Coordination charges were calculated for these compounds using the electronegativities created by Allred and Rochow (22) and extended by Little and Jones (23). These coordinatiom charge values are tabulated with the experimental edge inflection point energics in Table 1.

The values presented in Table 1, which includes both simple crystalline Mn compounds and complexes which are primarily σ-bonded, are plotted in Figure 2. It is seen that a reasonably good linear relationship is observed. Figure 2 demonstrates that, at least for

simply bonded complexes, there exists a linear relationship between coordination charge and X-ray K-edge energies. A least squares linear fit applied to the values in Table 1 gives:

$$\text{K-edge (eV)} = 2.27 \pm .15\eta + 6548.69 \pm .16$$

This fit was subsequently used to estimate the coordination charges corresponding to the K-edges of the three chloroplast samples. The results are tabulated in Table 3 and presented graphically in Figure 2 as the points X, Y and Z.

To test limits to which this approach can be applied, a number of mixed valence compounds and a number of compounds which are known to have metal-ligand π-bonding interactions were included as model samples. The coordination charge values for these compounds are presented in Table 2 and in Figure 3. It is evident from Figure 3 that many of these complexes exhibit behavior decidedly different in edge inflection point positions from those which involve sigma type bonding.

DISCUSSION

Estimation of the effective quantity of charge on a metal by using correlations of K-edge inflection points with coordination charge is possible within certain limitations. Examinations of Table 1 and Figure 2 for compounds in which manganese is simply ligated by

interactions shows a significant correlation of edge position with coordination charge.

Also evident is a general grouping of the Mn(II) compounds and a gap before encountering higher oxidation states. Closer examination shows five compounds with the same coordination charge, but different edge energies (labeled 6-10). This spread in points is not due to uncertainties in edge determination, but to the simplistic coordination charge calculation which treats all oxygen ligands the same, when in reality they have different properties. This inherent spread must be considered a very real limitation to the technique and in practice, tends to reduce the reliability of using the method to predict oxidation states.

This effect is even more evident when examining compounds which have unusual coordination environments (see Table 2 and Figure 3). Points A, B, and C represent complexes which have manganese in more than one oxidation state. It has been observed that edges of this type exist as composites (17). However, the coordination charges for these three complexes were calculated from the average coordination environment of the manganese sites. Thus, if the resolution of edge features is sufficient to give separate inflection points for both oxidation states, selection of the first inflection point can be expected to give erroneous results. For Mn_3O_4 (labeled A in Table 2 and Figure 3), which exhibits two edge inflections, this seems to be the case. Mn_3O_4 contains one Mn(II) and two Mn(III) sites. The second inflection point of the edge is included in brackets in Table 2 opposite the coordination charge calculated for the Mn(III) site. This

value is in much better agreement with the fit from Figure 1 (not shown). For Mn(3,4)Bipy and Mn(3,4)Phen (labeled B and C), the separate edges are apparently not resolved, and an average edge position is obtained in good agreement with the σ-bonded complexes.

A second condition under which this approach may break down is the occurence of manganese in high oxidation states. However, we observe that $KMnO_4$ (labeled D) is in fair agreement with the extrapolated line of Figure 3. The electronegativity value for Mn(II) was used in the calculation due to the unavailability of values for Mn(VII) and is the likely cause for an erroneously large coordination charge. In addition, coordination charge values for complexes which involve metal-ligand interactions can be expected to underestimate the amount of charge donated by the ligands. The four observed compounds of this type (labeled E, F, G and H) show a significant deviation from the predicted line and in the direction expected.

Thus, the following limitations for estimation of coordination charge values of manganese in chloroplasts must be kept in mind. The presence of multiple oxidation states will provide an average coordination charge value unless individual edge inflection points can be discerned. For the chloroplast edges reported here, in which no indication of multiple edges is evident, average coordination charge values will be expected. In addition, if the manganese complex in chloroplasts contains ligands which are π-donors, artificially large estimates of coordination charge will be made. The most likely biological complexes in which π-interaction may be expected are the manganese porphyrins. However, complexes of this type have not been

considered likely candidates as the moderately strong charge transfer bands have not been observed in chloroplasts and would not be expected to reversibly release manganese upon Tris treatment.

With these limitations in mind, a number of inferences concerning the oxidation state and ligand symmetry can be drawn for chloroplast manganese. It is evident that the difference in edge shape observed for active and Tris-treated chloroplasts shown in Figure 1, reflects a significant change in the electronic environment of the metal. The appearance of the relatively narrow transition at the edge for the Tris-treated sample, which is charactersitic of Mn^{+2} ion is in marked contrast to the broad, featureless edge of active chloroplasts. The latter is much more reminiscent of the edge of Mn(III) (acetylacetonate)$_3$.

We have observed that, with the exception of α-MnS, all complexes of Mn(II) measured in this study exhibit a large absorption maximum at the K-edge such as is observed for $Mn(H_2O)^{+2}_6$, and that none of the observed higher oxidation state complexes of Mn have such a feature. These trends have been seen for complexes of various metals (17) in which a pronounced broadening of the K-absorption edge appears to be correlated to a loss of symmetry at the metal site. In this instance, the onset of Jahn-Teller distortion with higher oxidation states may be sufficient to cause a significant broadening of "p" states responsible for the absorption maximum, and produce the difference observed between the Mn(III) $(acac)_3$, and the $Mn(H_2O)^{+2}_6$ edges. The anomaly seen with α-MnS has been reported with other metal-sulfur complexes (17) and although the effect is not fully understood, a

pronounced broadening of states may be caused by the high degree of covalency of the metal-sulfur bond.

Consideration of the above trends in K-edge shape affords the following statements concerning nature of manganese in the chloroplast samples. The characteristically broad edge of untreated chloroplasts is indicative of a manganese site of low symmetry. Likely causes of this condition include a significant portion of chloroplast manganese in oxidation states higher than +2, or a manganese site constrained to an unusual ligand configuration.

Secondly, the observably different edge of Tris-treated chloroplasts is interpreted to reflect a considerable content of manganese in the +2 oxidation state and a somewhat more symmetric environment. This is to be expected in view of the idea that inhibition of oxygen evolution is coincident with the release of manganese to an EPR detectable aqueous state. We have in fact observed that the Tris-treated chloroplast edge can be reconstructed by addition of approximately two-thirds of a normalized $Mn(II)(acetate)_2 \cdot 4H_2O$ edge to one-third of the Tris-treated, osmotically shocked chloroplast edge. Since Mn(III) is subject to disproportionation to Mn(II) and Mn(IV) in solution, release of either Mn(II) or Mn(III) from the membrane will result in the observed aqueous Mn(II).

Unfortunately, the intermediate appearance of the Tris-treated osmotically shocked sample (Z of Figure 1) is not so easy to interpret. As this sample should contain that fraction of manganese

not released by Tris extraction, this edge should provide information about the nature of the manganese pool not considered necessary for O_2 evolution. It appears that either this fraction contains some manganese in a site similar to $Mn(H_2O)^{+2}_6$ or that removal of the aqueous fraction by osmotic shock was not complete. Although no Mn^{+2} EPR signal could be detected in samples prepared under these conditions it is conceivable that a portion remains which is non-specifically bound to membrane components.

Placement of the chloroplast edge inflection point energies on the coordination charge plot (Figure 2) finds support for these ideas. The active chloroplast sample (Labeled X) is in the gap between observed Mn (II) and Mn (III) complexes. This indicates that the manganese is formally of oxidation state +2, or +3 or a mixture of the two. The first of these possibilities is considered unlikely. Indeed, if the observed edge position were for a +2 oxidation state, Figure 2 indicates that it would be the most ionically ligated divalent complex of this study. This is not a desirable property for a site which has been proposed to accumulate oxidizing equivalents. The concept of a mixed oxidation state is feasible for a couple of reasons. Of the five S states proposed to act as charge accumulators, S_0 and S_1, in the ratio of 1:3, are believed to be stable in dark adapted chloroplasts (10). Secondly, results of the Extended X-ray Absorption Fine Structure (EXAFS) (27) on these samples indicate a dimeric manganese site. Thus, the presence of a Mn(II)-Mn(III) and/or Mn(III)-Mn(III) site may be indicated (see Table 4).

Points Y (Tris-treated chloroplasts) and Z (Tris-treated, osmotically shocked chloroplasts) on the coordination charge plot (Figure 2) also support the ideas presented on the basis of edge shape. Tris- treated chloroplasts, suspected to contain hexaquated Mn^{+2}, give an average coordination charge value of -0.35, a value quite consistent with the divalent compounds having six oxygen ligands. The Tris-treated, osmotically shocked edge corresponds to a coordination charge which is intermediate between that of the other two chloroplast samples. This is indicative of either a mixture of coordination environments or a divalent manganese site with a highly ionic character.

It must be kept in mind that the above interpretations reflect the environment of all manganese retained by chloroplasts after initial isolation in 1mM EDTA. The release of only a fraction of the manganese from the membranes by alkaline Tris buffer and the resulting total loss of oxygen evolving capability raises valid concerns about the nature and involvement of the remaining fraction of manganese.

It was indeed our intent to construct the edge for the Tris releasable fraction of manganese by subtraction of one-third of the normalized Tris-treated, osmotically shocked spectrum from that of active chloroplasts. This difference edge is shown in figure 4. Shown also for comparison are the edges of active and "Tris-shocked" chloroplasts. Like the active chloroplast spectrum, the difference edge is broad and featureless , but is shifted to slightly higher energy, giving a predicted coordination charge of +0.36 (table 3). This value is even more in line with that of observed Mn(III)

compounds than is the total manganese environment considered earlier.

Also shown in Figure 4 is the edge of di-μ-oxo-tetrakis(2,2'-bipyridyl) dimanganese(III,IV) perchlorate Mn(3,4)Bipy). This compound has special importance in light of the results of EXAFS analysis presented in the Chapter 4 (27). These results show that the EXAFS of the active manganese site is consistent with a dimeric structure similar to that of the bipyridyl complex. It is seen that the difference chloroplast edge has a coordination charge quite close to that of the Mn(3,4)Bipy and Mn(3,4)Phen complexes but lacks the characteristic edge structure exhibited by these models. The absence of such edge structure in chloroplasts may reflect a significant difference in ligand environment but may also be due to disorder, as small differences in ligand symmetry will significantly reduce resolution of edge features. Possible sources of this disorder include residual heterogeneity of manganese sites and an expected equilibrium of two environments representing the S_0 and S_1 states which are stable in the absence of illumination.

To more accurately predict the oxidation state and ligands for the essential Mn, several coordination charge calculations were made using different combinations of oxygen and nitrogen ligands. These calculations are presented in Table 4. The estimated error in the chloroplast edge determinations results in a predicted range for the coordination charge of +0.1 to +0.5. Several of these hypothetical structures are in agreement with the range of coordination charges under consideration: Mn(II,II) with four oxygen or three oxygen and one nitrogen ligands, Mn(III,III) with six ligands, the majority

being oxygen, or Mn (III,IV) with six ligands, the majority being nitrogen.

The previous arguments against a Mn (II,II) complex hold, because an unlikely ligand environment must be invoked to explain the observed cooRdination charge.

Replacement of oxy-ligands with complexed water molecules will increase the observed coordination charge, because of differences in the ligand donating properties. Indeed, a penta-coordinate Mn (II,III) site both agrees with the observed edge properties and provides a possible site for water substrate binding. Such a configuration is in complete accord with a model of the water splitting site proposed by Wydrzynski and Sauer (13). This model contains a dimeric manganese complex, and exists in the dark as a three to one mixture of Mn(II,III) and Mn(II,II).

CONCLUSIONS

The experiments reported here and in Chapter IV (27) demonstrate the first direct observations of membrane bound manganese in chloroplasts. The shape observed and coordination charge deduced for the Mn absorption edge of active chloroplasts suggests an average environment for manganese sites. This proposed environment consists of a portion of the manganese in an oxidation state higher than +2. Both the proposed dimeric structure derived from the EXAFS analysis (27) andthe dark stability of more than one S intermediate of the charge storageobserved cycle make a mixture of oxidation states

probable. Such a mixture of oxidation states and the ensuing changes in coordination environment may well explain the absence of edge features and a coordination charge which is intermediate between that of observed Mn(II) and Mn(III) complexes. The model of Wydrzynski and Sauer (13) involving a manganese dimer in which a mixture of Mn(II,II) and Mn(II,III) in the ratio of 1 to 3 in the dark is consistent with the average environment observed in chloroplasts.

A drastic change in manganese environment upon inactivation of oxygen evolution by Tris-treatment. This change is indicative of the previously reported release of manganese from the putative water oxidation site into the inner thylakoid space where it appears as an aqueous Mn(II).

Finally, it is proposed that subtraction of one-third of the Tristreated, osmotically shocked chloroplast edge from that of active chloroplasts may provide a closer estimate of properties for the fraction of manganese sensitive to Tris release and hence to oxygen evolution capacity. Provided that the difference edge is a valid representation of the active pool of manganese, the observed coordination charge of +0.36 virtually assures that a significant fraction of the manganese present is in oxidation states greater than +2.

Table 1. Manganese Coordination Charges and X-ray K-Edge Energies for Model Complexes

Label	Compound	Coordination Charge (e's)[a]	K-Edge (eV)[e]
1	α-MnS	-3.04	6542.15
2	Mn(II) (S-phenyl)$_4$(P(Phenyl)$_4$)$_2$	-1.36	6545.11
3	$MnCl_2 \cdot 4H_2O$	-1.02	6546.97
4	$Mn_2LCl_2 \cdot 2H_2O$[b]	-0.67	6546.81
5	$Mn_2LBr_2 \cdot 2H_2O$[b]	-0.70	6546.63
6	$Mn(II)C_2O_4 \cdot 2H_2O$[b]	-0.46	6546.82
7	Mn(II) $(CCH_3CO_2)_2 \cdot 4H_2O$	-0.46	6547.91
8	Mn(II) $(AcAc)_2 \cdot 2H_2O$[c]	-0.46	6547.41
9	Mn^{+2} (aqueous)	-0.46	6548.54
10	$Mn(II)_2\ P_2O_7$	-0.46	6547.18
11	Mn(III) $(AcAc)_3$[c]	0.54	6550.70
12	Mn_2O_3	0.54	6549.55
13	Mn(IV,IV) Phen[d]	0.86	6551.04
14	α-MnO_2	1.54	6552.06

a. Units are electrons

b. L is the dianion of 11,23-dimethyl-3,7,15,19-tetraazatricyclo-(19.3.1.1^{9,13})hexacosa-1(25),2,7,9,11,13(26),14,19,21,21-decaene-25,26-diol.

c. AcAc = acetyl acetonate

d. Di-μ-oxo-tetrakis (1,10 phenanthroline) dimanganese (IV,IV) perchlorate

e. Error estimated to be $\pm$ 0.2eV

Table 2. Coordination Charges and X-ray K-Edge Energies for Model Compounds of Unusual Chemical Environments

Label	Compound	Coordination Charge (e's)[a]	K-Edge (eV)g
A	MN_3O_4	0.48	6547.13
		[0.54][b]	[6550.43][b]
B	Mn(III,IV) Bipy [c]	0.36	6549.67
C	Mn(III,IV) Phen [d]	0.36	6549.66
D	$KMnO_4$	5.36	6557.60
E	$[Mn(III)\ (PcPy)]_2O$ [e]	-0.31	6551.44
F	Mn(III) TPP Cl[f]	-0.43	6549.74
G	$K_3Mn(CN)_6$	-1.92	6555.12
H	$Mn_2(CO)_{10}$	-4.10	6553.52

a. Average of individual Mn coordianation charges; units are electrons

b. Second edge using only Mn (III) sites

c. di-μ-oxo-tetrakis (2,2'bipyridine) dimanganese (III,IV) perchlorate

d. di-μ-oxo-tetrakis (1,10 phenanthroline)dimanganese (III,IV) perchlorate

e. μ-oxobis (phthalocyanato pyridine) manganese (III) dipyridinate

f. Chloro-α,β,γ,δ-tetraphenylporphinato (H_2O) manganese (III)

g. Error estimated to be 0.2 eV.

Table 3. Experimentally Determined Coordination Charges and K-Edge Energies for Chloroplast Samples

Figure Label	Sample (see text)	Coordination Charge (e's)[a]	K-Edge (eV)[b]
X	"Active"	0.18(18)	6549.1
Y	"Tris-treated"	-0.35 (18)	6547.9
Z	"Tris-treated, osmoticaly shocked"	-0.04 (18)	6548.6
W	"Active" -1/3 "Tris-treated, osmotically shocked [c]	0.36 (18)	6549.6

a. Calculated from fit to values in Table 1 (see text); units are electrons

b. Error estimated to be 0. 3eV

c. Synthesized from curves X and Z

Table 4. Coordination Charge Calculations for Manganese Dimers with Different Combinations of Oxygen and Nitrogen Ligands

Manganese Oxidation State	Ligands	Coordination Charge
II,II	6 Oxy	-0.46
	5 Oxy	-0.05
	2 Oxy, 2 Nit	+0.02
	3 Oxy, 1 Nit	+0.19
	4 Oxy	+0.36
II,III	4 Oxy, 2 Nit	-0.30
	5 Oxy, 1 Nit	-0.13
	6 Oxy	+0.04
	3 Oxy, 2 Nit	+0.11
	4 Oxy, 1 Nit	+0.28
	5 Oxy	+0.45
	4 Oxy	+0.86
III,III	2 Oxy, 4 Nit	-0.14
	3 Oxy, 3 Nit	+0.03
	4 Oxy, 2 Nit	+0.20
	5 Oxy, 1 Nit	+0.37
	6 Oxy	+0.54
	5 Oxy	+0.95
III,IV	6 Nit	+0.02
	1 Oxy, 5 Nit	+0.19
	2 Oxy, 4 Nit	+0.36
	3 Oxy, 3 Nit	+0.53

FIGURE CAPTIONS

CHAPTER V

Fig. 1. X-ray absorption K-edges for manganese in three different chloroplast samples and two model complexes. Spectrum 9 is 1mM solution of $MnCl_2$, 11 is Mn(III) (acentonatoacetonate)$_3$, X is the active chloroplasts, Y is the Tris-treated chloroplasts, and Z is the Tris-treated, osmotically shocked chloroplasts (see text and Table 1).

Fig. 2. Manganese K-edge inflection point energy versus coordination charge for 14 compounds and complexes (labeled 1-14). The three chloroplast samples (X, Y, and Z) were placed on a linear fit to points 1-14 (see tables 1 and 3 for label description).

Fig. 3. Manganese K-edge inflection point energy versus coordination charge for complexes containing manganese with mixed valence, high oxidation state, or ligands providing pi overlap (points A-H) (see Table 2 for label description).

Figure Captions, Chapter V, continued

Fig. 4. X-ray absorption K-edges for manganese in chloroplasts. Z denotes the spectrum for Tris-washed, osmotically shocked chloroplasts, X denotes the edge for active chloroplast, and W denotes an edge constructed by subtraction of one-third of the normalized Tris-shocked chloroplast edge from that of active chloroplasts. Edge B denotes that of di-μ-oxo-tetrakis (2,2'bipyridine) dimanganese (III,IV) perchorate (Mn(3,4)Bipy) which is included for comparison.

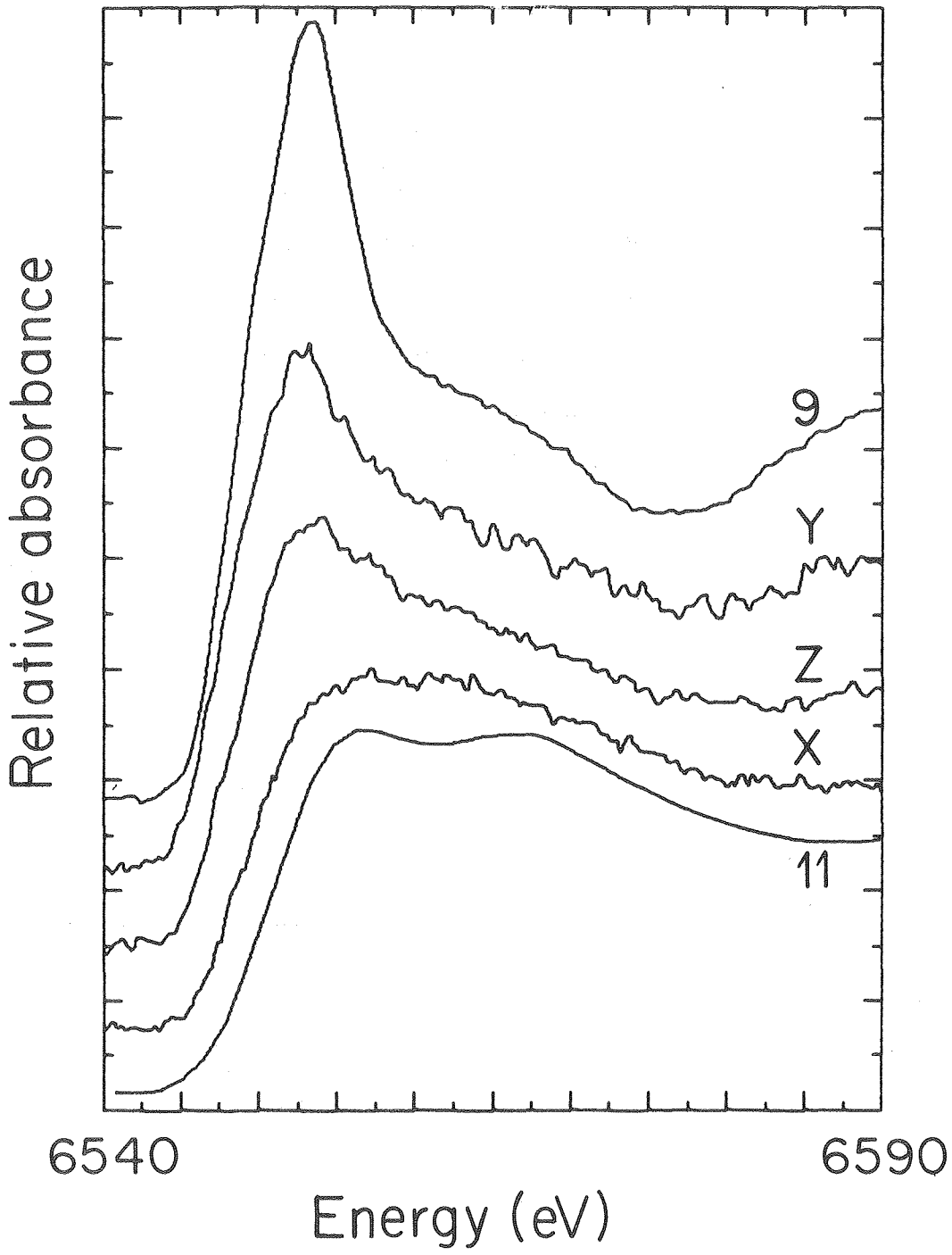

XBL796-4868

CHAPTER V

Figure 1.

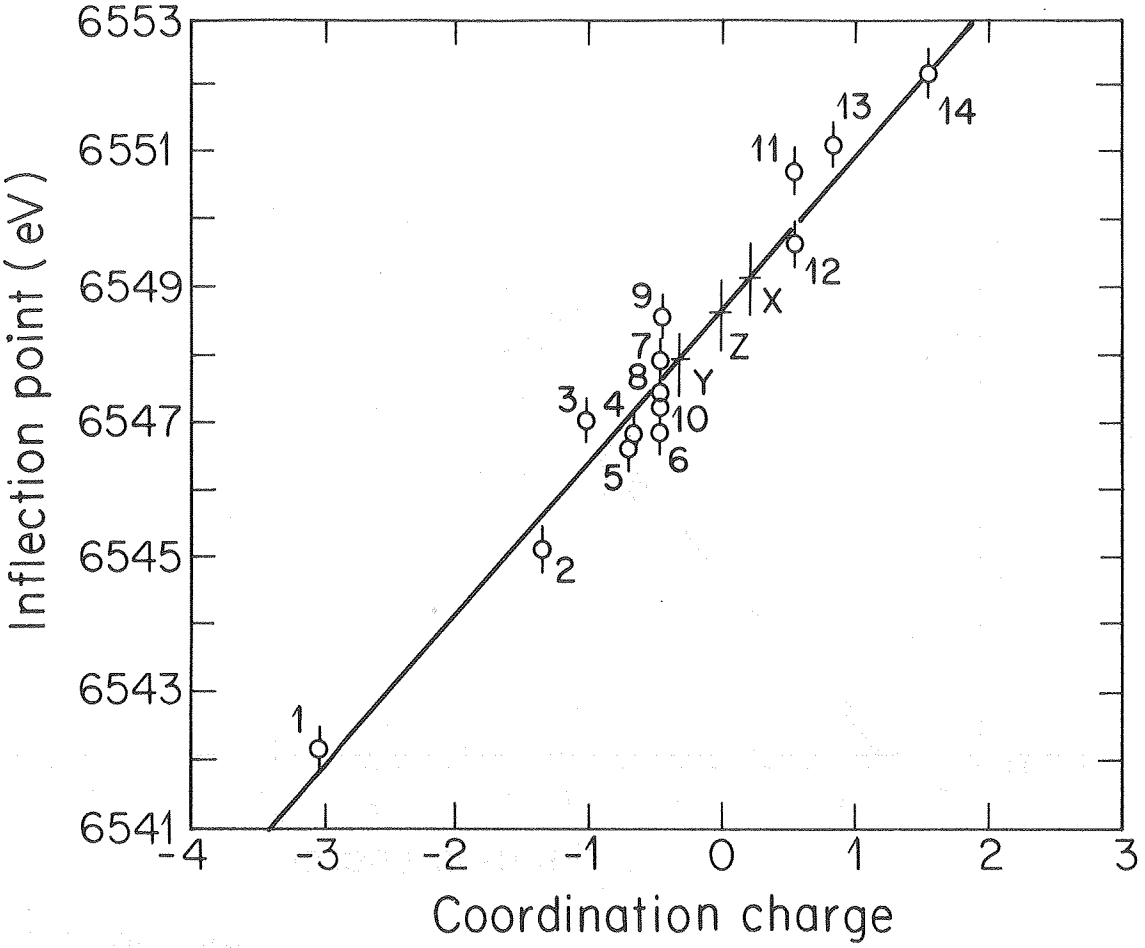

XBL796-4873

CHAPTER V

Figure 2.

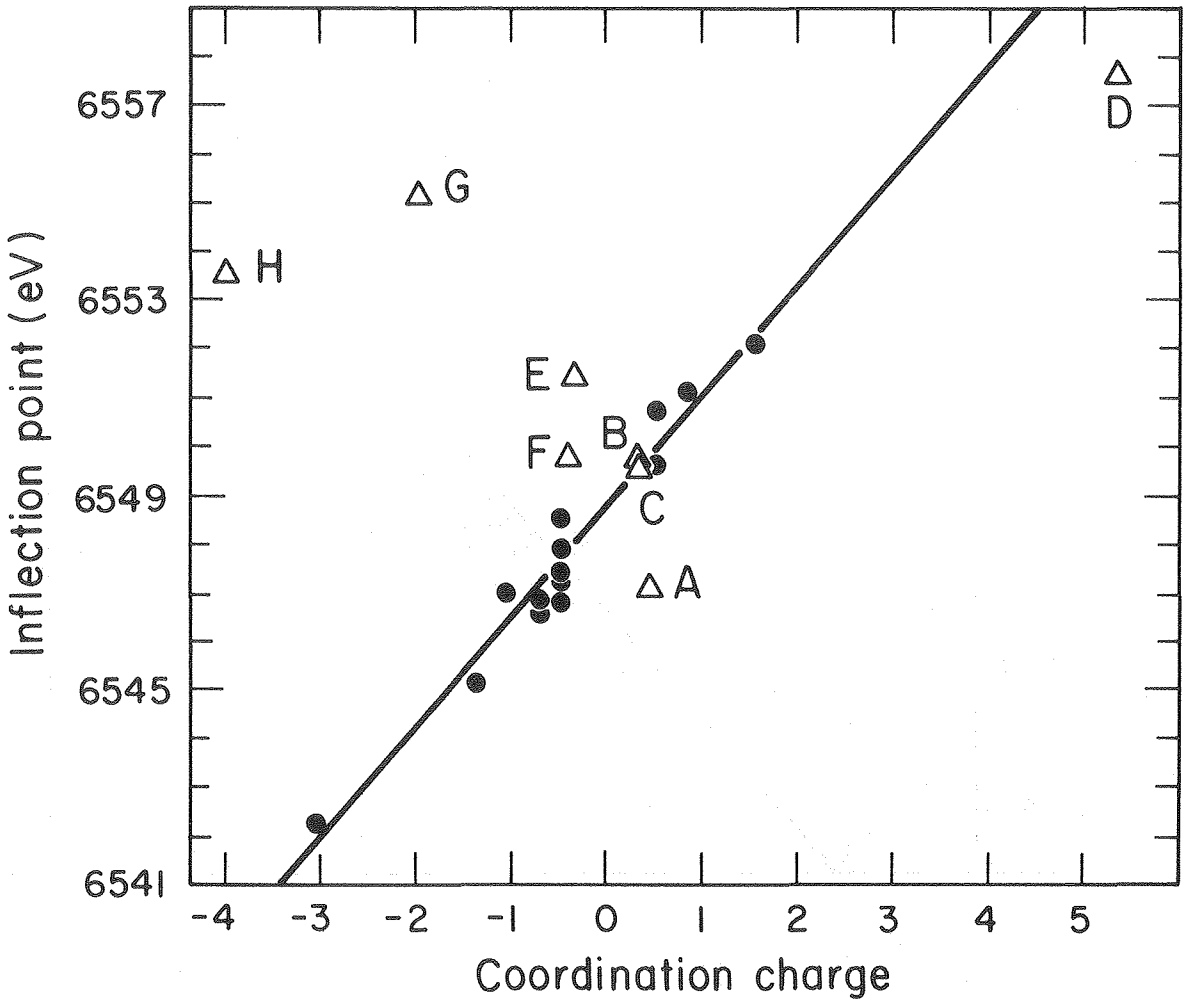

XBL 796-4870A

CHAPTER V

Figure 3.

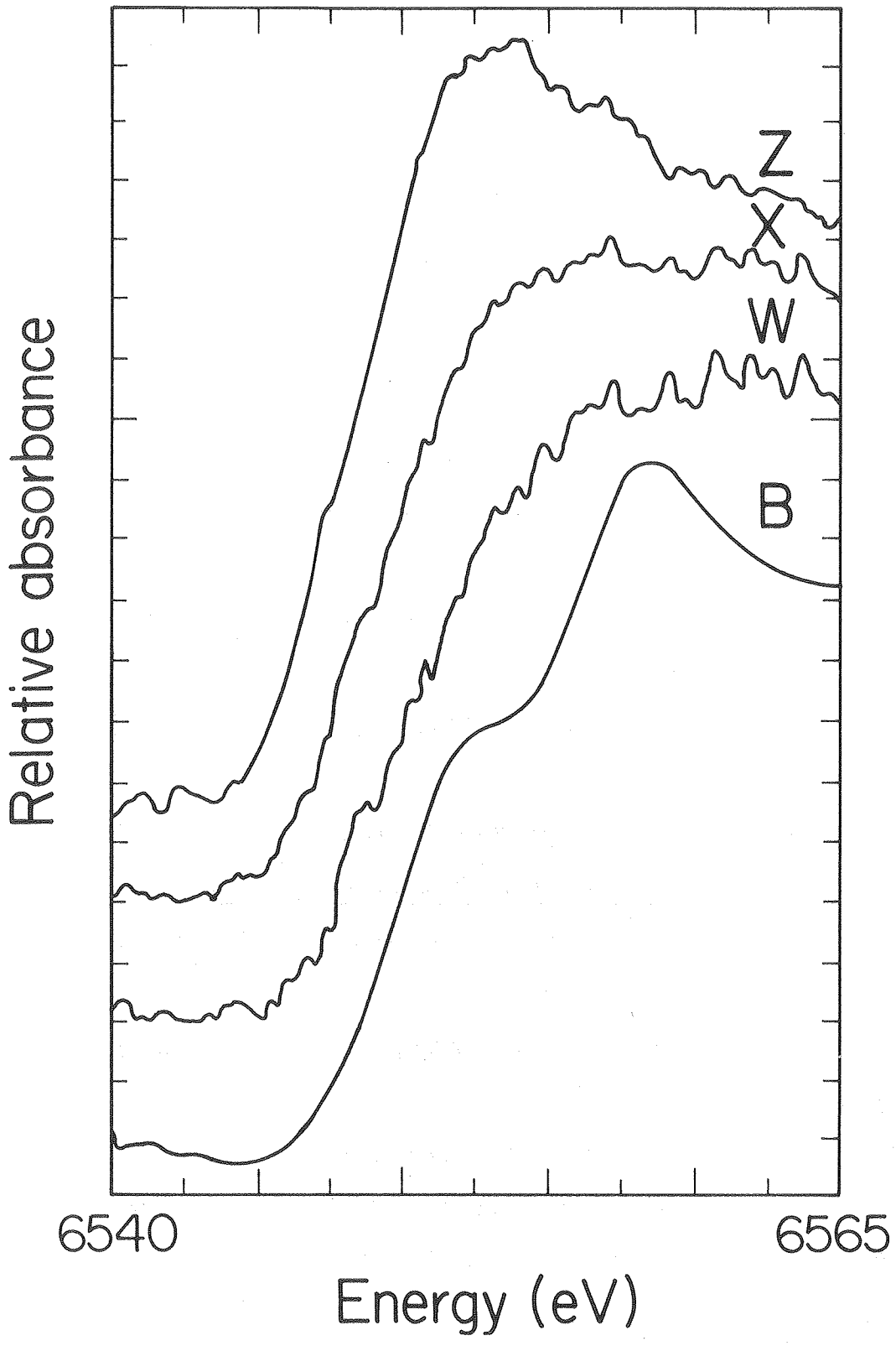

CHAPTER V

Figure 4.

XBL 805-4185

REFERENCES

CHAPTER V

1. Pirson, A. Z. Botan. 31, 193 (1937).
2. Eyster, C. Brown, T.E., Tanner, H.A., and Hood, S.L. Plant. Physiol. 33, 235 (1958).
3. Spencer, D. and Possinghan, J.V. Aust. J. Biol. Sci. 13, 441 (1961).
4. Kessler, E. Arch. Biochem. Biophys. 59, (1955).
5. Cheniae, G.M. and Martin, I.F. Biochim. Biophys. Acta 197, 219-239 (1970).
6. Cheniae, G.M. and Martin, I.F. Brookhaven Symp. Biol. 19, 406 (1966).
7. Yamashita, T. and Butler, W.L. Plant Physiol. 43, 1978 and 2037 (1968).
8. Heath, R.L. and Hind, G. Biochim. Biophys. Acta 189, 222 (1969).
9. Homann, P.H., Biochem. Biophys. Res. Commun. 33, 229 (1968).
10. Kok, B., Forbush, B. and McGloin, M. Photochem. Photobiol. 11, 457-475 (1970).
11. Joliot, P., Barbieri, G., and Chabaud, R. Photochem. Photobiol. 10, 309-329 (1969).
12. Wydrzynski, T., Zumbulyadis, N., Schmidt, P.G., Gutowsky, H.S., and Govindjee. Proc. Natl. Acad. Sci. USA 73, 1196-98 (1976).
13. Wydrzynski, T. and Sauer, K. Biochim. Biophys. Acta 589, 56-70 (1980).
14. Blankenship, R.E. and Sauer, K. Biochem. Biophys Acta 357, 252-266 (1974).

References, Chapter V, continued

15. (a) Kramer, L.N. and Klein, M.P. J. Chem. Phys. 51, 3618 (1969). (b) Kramer, L.N. and Klein, M.P. Chem. Phys. Lett. 8, 183 (1971).

16. Herber, R. "The Mossbauer Effect and Its Application in Chemistry", Advances in Chemistry Series, No. 68, Am Chem. Soc. Washington, D.C. (1967) pp. 8-20.

17. Sinastava, U.C. and Nigam, H.L. Coor. Chem. Rev. 9, 275 (1972-3).

18. Ovsyannikova, I.A., Batsanov, S.S., Nasonova, L.I., Batsanova, L.R., and Nekrasova, E.A. Bull. Acad. Sci. USSR Phys. Ser. (Eng. translation), 31, 936 (1967).

19. Pauling, L. "The Nature of the Chemical Bond", 3rd edition, Cornell Univ. Press, Cornell, NY. , p. 98 (1960).

20. Batsanov, S.S. "Elecktrootritsatel 'nost' Elementov i Khimicheskaya Svyaz' (Electronegativity of Elements and Chemical Bonds), Novosibirsk, 1962. pp 1-175.

21. Cramer, S.P., Eccles, T.K., Kutzler, F., Hodgson, K.O., and Mortenson, L.E. J. Am. Chem. Soc. 98, 1287 (1976).

22. Allred, A.L. and E.G. Rochow. J. Inorg. Nucl. Chem. 5, 264 (1958).

23. Little, E.J. and Jones, M.M. J. Chem. Educ. 37, 231 (1960).

24. Kincaid, B.M. Ph.D. Thesis, Stanford University (1974).

References, Chapter V, continued

25. Blankenship, R.E. and Sauer, K. Biochim. Biophys Acta 357, 252 (1974).

26. See for example, Yeh, H.C. and Azaroff, L.V. J. Appl. Phys. 38, 4034 (1967) and the Mn(III) (acetyl acetonate)$_3$ spectrum in Fig. 1(a) which is distorted by the Jahn-Teller effect.

27. (a) Kirby, J.A., Robertson, A.S., Klein, M.P., Smith, J.P., Thompson, A.C., and Cooper, S.R., (submitted).
(b) Chapter 4.

28. Cooper, S.R., private communication; Cooper, S.R. and M. Calvin, J. Am. Chem Soc. 99, 6623 (1977).

29. Jaklevic. J., Kirby, J.A., Klein, M.P., Robertson, A.S., Brown, G.S., and Eisenberger, P. Solid State Comm. 23, 679 (1977).

30. Blankenship, R.E., Bacock, G.T., and Sauer, K. Biochim. Biophys. Acta 387, 165-175 (1975).

31. Spector, M. and Winget, G.D. Proc. Natl. Acad. Sci. USA 77(2), 959 (1980).